UNIVERSITY OF CALIFORNIA
SANTA CRUZ

GEOLOCATION OF A RADIO FREQUENCY EMITTER USING A SINGLE LOW EARTH SATELLITE

A dissertation submitted in partial satisfaction of the
requirements for the degree of

DOCTOR OF PHILOSOPHY

in

ELECTRICAL & COMPUTER ENGINEERING

by

Patrick Ellis

December 2020

The Dissertation of Patrick Ellis
is approved:

Dr. Farid Dowla, Chair

Dr. Hamid Sadjadpour

Dr. Dejan Milutinovic

Dr. Don Van Rheeden

Quentin Williams
Vice Provost and Dean of Graduate Studies

Table of Contents

List of Figures

List of Tables

Acronyms

BPSK Binary Phase Shift Keying

cEKF constrained Extended Kalman Filter

CRB Cramér-Rao Bound

cUKF constrained Unscented Kalman Filter

cUPF constrained Unscented Particle Filter

DTED Digital Terrain Elevation Data

ECEF Earth Centered Earth Fixed

ECI Earth Centered Inertial

EKF Extended Kalman Filter

FIM Fisher Information Matrix

FLOPs Floating Point Operations

GNP Gaussian noise process

GRV Gaussian Random Variables

HMM Hidden Markov Model

IMM Interacting Multiple Models

KF Kalman Filter

LEO Low Earth Orbit

MEO Medium Earth Orbit

MM Multiple Model

NNSS Navy Navigation Satellite System

PCA Point of Closest Approach

PCRB Posterior Cramér-Rao Bound

pdf probability density function

PF Particle Filter

rcPCRB recursive constrained Posterior Cramér-Rao Bound

RF Radio Frequency

rPCRB recursive Posterior Cramér-Rao Bound

SIS Sequential Importance Sampling

SSG Single Satellite Geolocation

UKF Unscented Kalman Filter

Abstract

Geolocation of a Radio Frequency Emitter using a Single Low Earth Satellite

by

Patrick Ellis

A passive Radio Frequency (RF) geolocation solution is provided that uses a single Low Earth Orbit (LEO) satellite to find an uncooperative earth-bound emitter. For the first time, an unambiguous solution is available for real-time, single-pass, and time-constrained acquisition scenarios where single transmissions are expected and computational abilities are limited. The geolocation algorithm rapidly maps Doppler and Doppler Rate measurements to an RF emitter location, offering a unique and powerful take on Single Satellite Geolocation (SSG) - the provision of a geolocation estimate only using one satellite as a passive receiver. An initial search area of several hundred kilometers squared is expected.

Two solutions are provided that cater to approximately symmetric and asymmetric error distributions, respectively. The first is a variant of the constrained Unscented Kalman Filter (cUKF), which harnesses the estimation abilities of the Kalman Filter, the modeling capabilities of the Unscented Transform, and a novel projection technique to constrain estimates to be on the Earth's surface. When the error distributions are strongly non-Gaussian, as is common when ephemeris and oscillator errors are present, a constrained Unscented Particle Filter (cUPF) has been derived. In this solution, the cUKF is used as the proposal distribution to allow the Monte Carlo properties of the Particle Filter to efficiently characterize the Posterior Distribution, while still avoiding sample degeneracy. Both the cUKF and cUPF solutions are capable of obtaining single-kilometer geolocation accuracy despite small sample sizes, short signal durations, large search areas,

and non-trivial transceiver geometry. Usage of the cUKF versus the cUPF can be seen as a trade-off between computational speed and modeling capabilities. Corresponding theoretic performance bounds are provided for mission analysis and algorithmic optimality comparison. The bound takes the form of the recursive constrained Posterior Cramér-Rao Bound (rcPCRB). This theoretic information bound is uniquely suited to gauge the mean squared error optimality of iterative nonlinear estimation algorithms - and is recast and adapted to the SSG scenario.

Computational capabilities of spaceborne processing units are reviewed. A full computational cost profile of the two provided geolocation solutions are given in terms of three types of floating point computations during a single algorithmic iterative step. Computational requirements are well within reach of current space-proven processing units. The advent of hybrid processing units speak to the provided algorithms' potential even more.

In all simulated scenarios, the provided cUKF geolocation solution meets the optimal performance bounds provided by the rcPCRB, always reaching sub-kilometer geolocation accuracy. Numerical analysis over measurement noise, center frequency, slant angle, and initialization errors showcase the cUKF's robustness and aptitude over different mission profiles. When oscillator and ephemeris errors are present, the cUPF continues to obtain single kilometer geolocation accuracies, even with single second acquisition times, limited computational powers, and several hundred kilometer search spaces. Finally, the performance of the cUPF is demonstrated on raw IQ data acquired from the TDS-1 satellite operated by Surrey Satellite Technology, which listened to a transmitting beacon over White Sands, New Mexico. This real life experiment exactly represents the scenario designed for by this dissertation and provides a worst case test scenario with extremely low SNR, small sample size, ephemeris and timing errors, and high

quantization error. In order to deal with the highly non-Gaussian error distributions, the cUPF was utilized and performed extremely well - converging within three seconds to within approximately 10 kilometers of the true emitter position over a 500^2 km search space with only 24 samples.

Dedication

To my parents Michael and Neliza Ellis

To my sister Anna Ellis

To my partner Kellen Stanley

To my friends Jan-Luca Bell and Jamal Roache

To my dogs Ziggy and Rapinoe

Thank you.

Acknowledgments

Many people have helped achieve this life milestone. First and foremost, I thank my parents whom instilled within me an insatiable curiosity and gave me the means to pursue it. I thank my sister, whose soft humility while treading through her continual successes makes her a constant role model. My undergraduate advisor, Dr. In Soo Ahn, was the first person to introduced the idea of graduate school to me, and deserves high recognition. I thank my Master's advisor, Dr. Benjamin Friedlander, whose sharp acumen still shapes the way I think to this day. Additional gratitude is given to my time spent at BBN Technologies and MIT Lincoln Laboratory - they crafted the way I see engineering and helped me define my role in it. To my PhD advisor, Dr. Farid Dowla, I thank whole-heartedly for his measured guidance, intuition, and time that made this whole enterprise possible and enjoyable. I want to thank Dr. Don Van Rheeden for his technical expertise and advice, as well as the Southwest Research Institute as a whole for funding a portion of this degree. Finally, I want to make a special mention to the late Dr. Joel Kubby. Without his observational care and departmental guidance, I would not be in this program. May he rest in peace, and those whom he touched such as I continue to honor his quiet fortitude.

The text of this dissertation includes material in previously published work. They are listed below:

- P. Ellis and F. Dowla, "A Single Satellite Geolocation Solution of an RF Emitter using a Constrained Unscented Kalman Filter," IEEE Statistical Signal Processing Workshop 2018, pp. 643-647, 2018

- P. Ellis and F. Dowla, "Performance Bounds of a Single LEO Satellite Pro-

viding Geolocation of an RF Emitter," 9th Advanced Satellite Multimedia Systems Conference and 15th Signal Processing for Space Communications Workshop, pp. 1-5. 2018

- P. Ellis and F. Dowla, "RF Emitter Geolocation Using a Single Satellite," 2018 GEOINT Symposium (Talk) 2018

- P. Ellis and T. Sturdevant, "RF Emitter Geolocation Using a Single SmallSat," 33rd Annual AIAA/USU Conference on SmallSats, 2019.

- P. Ellis "TF Geolocation Using a Single LEO Satellite" Joint SMC/IEEE AESS Meeting. San Antonio, TX December 2019 (Talk)

- P. Ellis, D.Van Rheeden, and F. Dowla, "Use of Doppler and Doppler Rate for RF Geolocation Using a Single LEO Satellite," IEEE Access Journal, January 2020

- P. Ellis and F. Dowla, "Single Satellite Emitter Geolocation in the Presence of Oscillator and Ephemeris Errors," 2020 IEEE Aerospace Conference, pp. 1-7, March 2020

Chapter 1

Introduction

1.1 Motivation

The ability of satellites to detect and geolocate RF signals is highly coveted as it facilitates search-and-rescue, tracking, and spectrum monitoring. A single satellite geolocation (SSG) solution, if geolocation accuracy is maintained, offers many benefits. With respect to multi-satellite systems - maintenance, calibration, and central node establishment between satellites are largely eliminated. Satellite formations, requiring expensive and time-consuming launch methods and onboard propulsion systems, are avoided.

All altitudes offer geolocation capabilities for satellites. The higher the satellite, the larger the search space. However, as the most effective SSG solutions utilize the Doppler generated by the respective motion between the satellite and the emitter, LEO is the only orbit altitude conducive to geolocating the short duration (singular second), single burst emitters this dissertation is focused on. Additionally, since satellites in LEO are rarely spaced for simultaneous reception of an RF emitter, there is an existing, demonstrable need for a reliable SSG solution for RF geolocation.

A new space age has arrived where ultra-small satellites are being launched in unprecedented numbers. These satellites do not have the computational abilities nor the instrumental accuracies that existing SSG methods require. LEO satellites provide large look areas upon the earth, but their fast orbital speeds often prevent multiple bursts of the unknown emitter with a low repetition rate to be captured in a single pass - often giving scenarios where only a single transmission burst is available for geolocation. Consequently, there is a clear and dire need for an SSG solution to provide an unambiguous solution applicable for real-time, single-pass, and time-constrained acquisition scenarios where single transmissions are expected and computational abilities are limited.

1.2 Context

1.2.1 The SmallSat Revolution

Over the past couple decades the *SmallSat Revolution* has emerged, signaling a seismic change in the space exploration paradigm. Satellites are now being made in much smaller sizes and increasingly larger numbers. In the past, massive satellites the size of school buses were commonplace. Yet, in 2015 alone, 48% of the satellites launched were less than 10 kg [2] and the trend has continued. *SmallSats* have firmly established themselves as the satellite of choice across the market.

SmallSats are generally classified by their weight, although a completely standardized categorization has not yet been established. One formulation is: ESPA-Class (<180kg), CubeSats (<10kg), ChipSats (<1g). Another formulation is Minisatellite (>100 kg), Microsatellite (10-100kg), Nanosatellite (1-10kg), Picosatellite (0.1-1kg), and Femtosatellite (0.001-0.01kg). The vast majority of the small

spacecraft launched are in the CubeSat-class. The concept of a CubeSat was first established in the space community in 1999 by professors from Stanford and California Polytechnic University, whom devised and implemented a modular system of standardization - SmallSats were to be measured in units of 1U cubes, measuring 10x10x10 centimeters and 1.33kg weight. As such, CubeSats grow in size through the accumulation of these units. 1.5U, 2U, 3U, 6U, etc [1].

One major benefit of the smaller satellite sizes is that they can be much more affordably flown as secondary payloads on launch vehicles or from the International Space Station. It has been observed that as satellites get smaller and smaller, the launch vehicle industry has provided rockets that are growing bigger and bigger and carrying more and more satellites per launch. This trend caters to the lower-cost of space entry that is attracting so many space endeavors [67]. However, the price reduction that comes from being launched as secondary payloads means SmallSats are highly constrained in terms of available orbits and launch times. This can adversely affect the transceiver geometry in geolocation scenarios.

The reduction in size has also enabled the ability to launch many more satellites than before and at a much cheaper price. One of the most appealing aspects of the SmallSat Revolution is the ability to rapidly traverse through mission concept design, spacecraft production, launch, and operations. Generally speaking, SmallSats can be conceived as an idea to realization within two years, costing anywhere from $30,000 US dollars to roughly one million US dollars. This is a vast improvement from the hyper-expensive satellites of decades past [67]. The trade-off for the reduction in cost is the acceptance of higher mission risk. SmallSats are most often built with commercial off-the-shelf parts, although as interest by various industrial, government, and private entities increases, military-grade and space-ready components are actively being developed today. Despite these

Table 1.1: Consequences of the SmallSat Revolution

Advantages	**Disadvantages**
Cost Effective Production	Lower Quality Assembly
Fast Idea-to-Space Time	Limited Orbital Choices
Low Launch Costs	Constrained Launch Times
Greater Numbers of Satellites	Shorter Satellite Lifetimes

improvements, mission planners still need to contend with the lower reliability and quality of SmallSats compared with their larger predecessors.

SmallSat bus ('bus' is the infrastructure of the satellite that determines the orientation, size, and type of payloads available to the spacecraft) size inherently limits its capabilities. Naturally, a smaller spacecraft implies a smaller bus which means less spacecraft capabilities. However, the past two decades have seen a drastic improvement in processing power, data storage, propulsion, and solar array efficiency that allows small buses to provide large capabilities. As a result, SmallSats now provide many long-life, complex operational missions in commercial communications, earth observations, and military surveillance [38]. Despite these impressive SmallSat accomplishments, the limited power supply and computational capabilities are still major design constraints.

An exciting new era of space exploration has been entered. The advantages afforded by the SmallSat Revolution have been outlined as well as the trade-spaces it creates when designing a satellite mission. These are summarized in Table 1.1. The work provided in this dissertation utilizes the unique opportunities afforded by this new space age, but also specifically mitigates and caters to the detrimental aspects as well.

1.2.2 Space RF Geolocation

Space offers the ultimate high ground, and has long held vested interest from the private, government, and commercial communities. The SmallSat Revolution is rapidly replacing prohibitively expensive monolithic satellites with low-cost, smaller sized platforms that are performing increasingly complex missions. This change in space accessibility and utilization has opened up a wide variety of opportunities. While the SmallSat missions are high-risk, there is also high return with a relatively low cost. Technology miniaturization, solar array efficiency, and increased processing power have paved the way for mission concepts previously thought impossible on such a small bus size.

One of the burgeoning application areas for SmallSats is RF Geolocation. In fact, patents dealing with RF geolocation are currently the fourth most numerous patent type in the satellite industry [62]. However, nearly all of these patents are tailored for large and expensive satellite systems. A few - such as Hawkeye 360, Spire Global, and some academic entities are just now attempting to provide RF geolocation with multiple SmallSats [11]. Previous concerns of the quality of onboard electronics, computational powers, and general risk held back investment in prior years. However, there is now an acceleration, particularly in the intelligence community, on the willingness to adopt small satellites for missions. According to Bill Gattle, the former program director of terrestrial communications and director of engineering for defense programs at the Pentagon, "It's moved from... customers being intrigued to believing it's worthy of a demo." Indeed, geolocation and other related situation awareness scenarios are expected to grow at a compound annual growth rate of 21% for the next 10 years [3, 38].

An SSG solution fits very well into these trends. Situational awareness and geolocation utility is dependent on first hearing the signals of interest. Space

geolocation systems requiring multiple satellites comes with a variety of caveats. For instance, placing these systems in a fashion that covers large search areas simultaneously is prohibitive in terms of number of satellites needed, cost, and system maintenance. Having the ability to geolocate an RF signal with only a single satellite decreases the point of failure for a geolocation system and allows greater coverage. The proposed SSG solution fits perfectly within the trends of SmallSats and RF geolocation from space.

1.3 Contributions and Novelty

The SSG solutions developed in this Dissertation are governed by measurements of both Doppler and Doppler Rate. As all previous SSG solutions solely utilize Doppler, a thorough analysis showing how Doppler and Doppler Rate provide a vastly improved solution space is provided in Section 2.3. Of particular note is the provision of an unambiguous solution space, which is addressed in depth and best depicted in Fig. 2.3 and Fig. 2.4. The measurement equations are kinematically derived and can be seen in its final form in Eq. 2.24 along with the full derivation in Appendix 8.1.

A key separation of the provided solutions from other SSG approaches is the ability to geolocate signals with very short (singular-second) durations. The difficulty of this achievement stems from the short duration signals creating an extremely ill-conditioned solution space. The answer to this issue was a combination of using Doppler and Doppler Rate measurements, assuming the unknown emitter to be approximately stationary and sitting upon the Earth's ellipsoidal surface, framing the problem in the Earth Centered Earth Fixed (ECEF) coordinate system, and performing geolocation with iterative, nonlinear filtering techniques. A visual representation of these developments on the solution space can be seen in

Fig. 2.5. The assumption of an approximately stationary emitter is made widely applicable by the short signal duration and the fast speeds of the satellite. The ECEF coordinate system necessitates only three state variables to be estimated - the rectangular coordinates of the emitter position. This eliminates the need to estimate velocity or acceleration components - greatly enhancing the stability of the SSG solution and simplifying the state equation as seen in Eq. 2.14. To enforce the ellipsoidal constraint in real-time filtering applications, a completely novel method of projecting sigma points into the constrained solution space is developed in Section 3.1.2 and Appendix 8.2.

The choice of an iterative nonlinear filtering algorithm to provide geolocation estimates comes from expectations of short signal duration, highly nonlinear measurement equations, the presence of ephemeris and oscillator errors, and the need for an Earth-surface constraint. Two algorithms were developed based on the potential noise characteristics in the measurement equations shown in Eq. 2.24. The cUKF was developed for situations when the Posterior error distribution is mostly symmetric and the cUPF for when the Posterior error distribution is asymmetric. The construction of the cUKF algorithm is outlined in Section 3.1.2 and the cUPF is detailed in Section 3.2.2. The trade-off between the two algorithms are outlined in Table 3.1. Both of these algorithms take advantage of the aforementioned novel sigma-point projection method developed in Section 3.1.2.

For the SSG scenario, ephemeris and oscillator errors are a serious concern and have not yet been dealt with by any available SSG solution today. A thorough literature review was done to collect experimentally obtained values of these errors explicitly pertaining to SmallSats. The magnitudes of both ephemeris and oscillator errors present in these SmallSat missions are summarized into three categories of severity in Table 2.1 and Table 2.2, respectively. A methodology of

statistically quantifying ephemeris errors was then developed and can be found in Section 2.3.5. An analytic form of the received signal in the presence of oscillator errors was derived and can be found in Eq. 2.35.

A key component of the offered SSG solutions is their ability to be run in real-time aboard existing SmallSat processing units. For persective, an overview of onboard computational capabilities of SmallSats is provided in Section 3.3. The computational costs of the cUKF and cUPF are outlined in Table 3.2 and Table 3.3, respectively. The computational costs are described in terms of the number of Floating Point Operations (FLOPs), square root operations, and trigonometry operations per kth step of both the cUKF and cUPF.

Both the cUKF and cUPF aim to minimize the mean squared error. By obtaining the theoretical lower limit of minimizing the mean squared error, a measure of optimality can be obtained. The traditional Cramér-Rao Bound (CRB) provides this performance measure, and it is currently the form all existing performance bounds in literature take for the SSG scenario. However, the CRB is meant for block processing and derives its information theoretic measure from measurement equations. This is in stark contrast with SSG algorithms in use today (including the cUKF and cUPF developed here) that utilize both the measurement equations and state equations in an iterative fashion to obtain geolocation estimates. As a result, all currently available bounds that utilize the CRB are poor indicators of SSG algorithmic optimality. To remedy this, a recursive constrained Posterior Cramér-Rao Bound (rcPCRB) was derived for the SSG scenario. It's final form can be found in Eq. 4.17, elaborated on in Section 4.2, and whose explicit derivatives can be found in Appendix 8.3. This bound provides the best possible mean squared error achievable for any iterative, nonlinear algorithm utilizing both state and measurement equations when corrupted with approximately Gaussian noise.

With the rcPCRB in place as a theoretical performance bound, significant effort was made to find the most effective contemporary SSG solution as means of comparison. Both the cUKF and cUPF are an unambiguous, computationally friendly algorithm that is able to converge in single-pass, time-constrained acquisition scenarios where single transmissions are expected. As covered in Section 2.2, no other existing technique can do this. In order to properly gauge the caliber of these developed algorithms, the liberty was taken to adapt prior and current techniques to the fit these design constraints through use of a constrained Extended Kalman Filter (cEKF), constructed in Section 3.1.2, and explicitly stated in Eq. 3.12. In Section 5, numerical analysis is done over measurement noise, center frequency, slant angle, and initialization errors. The cUKF's superiority over the cEKF is showcased by outperforming the cEKF by over three orders of magnitude in every scenario. In these simulations, less than 5 seconds of signal acquisition were utilized, steady state was reached within 3 seconds, and geolocation errors of less than a single kilometer were obtained. The cUKF also matched the rcPCRB in each of these simulated scenarios - proving that the cUKF is reaching the optimal minimum mean squared error. In scenarios where the cUPF is to be used - such as large ephemeris and oscillator errors - the cEKF failed completely to converge. In contrast, the cUPF performed extremely well, obtaining single kilometer geolocation accuracy as shown in Figs. 5.7-5.11. Initial search spaces spanned hundreds of kilometers.

As a final validation, the cUKF and cUPF are demonstrated on raw IQ data acquired from the TDS-1 satellite operated by Surrey Satellite Technology. The TDS-1 satellite is a SmallSat that listened to a transmitting beacon over White Sands, New Mexico at the L1 frequency in November of 2016. The experiment exactly represents the desired scenario and provides a worst case test: the ex-

periment exhibited extremely low SNR, small sample size, ephemeris and timing errors, and high quantization error. In select cases, the cUKF could reach single kilometer geolocation accuracies (Fig. 6.12). But in general, the cUKF could not deal with the asymmetrical error distributions - generally yielding geolocation estimates converging to about 40 km of the true beacon location. The cUPF was then utilized and performed extremely well. In 50 trials, utilizing only 80 measurements of Doppler and Doppler Rate each, the cUPF converged within three seconds (24 samples) to just under 10 kilometers of the true emitter location. The initial search space covered an area of over 500^2 kilometers. The results of this promising validation are shown in Fig. 6.13. The cUPF algorithm performed exceptionally well given a worst-case scenario, and therefore provides a high level of assurance for its capabilities on many existing and future systems.

Chapter 2

Problem Formulation

2.1 Application Scenario

The physical scenario involves a single LEO satellite receiving a signal emitted by a transmitter on the surface of the earth. The satellite has no knowledge of the position of the transmitter, but does know its own position, velocity, and acceleration (all orbital information on the satellite is referred to as *ephemeris* information). There is a certain amount of error affiliated with the ephemeris information as well as oscillator errors occurring within the transmitted radio and the receiver clock on the satellite. The search area for the emitter is generally a circle projected to the Earth's surface with a diameter on the order of several hundred kilometers.

The only knowledge of the transmitted signal that the satellite holds is whatever knowledge is needed to produce the measurements that the chosen geolocation algorithm uses to generate a position estimate. Typical assumptions include knowledge of the center frequency and modulation scheme, although this varies widely based on the scenario. The main objective is to unambiguously estimate the emitter location as quickly and accurately as possible. The accuracy will be

such that the developed algorithm provides geolocation estimates that yield the lowest possible mean squared error estimate. A measure of mean squared error optimality will be given by a theoretic performance bound.

An example scenario is shown in Fig. 2.1. An emitter sits off the coast of Greenland at longitude 35 deg W and latitude 65 deg N transmitting a 1200 Baud Binary Phase Shift Keying (BPSK) signal at a center frequency of 120.6 MHz for 5 seconds continuously. The satellite flies in a circular orbit at an altitude of 1000 km, receiving the signal at a 15 deg slant angle and a slant range of about 1400 km. The average Carrier-to-Noise ratio is about 15 dB over the acquisition time. As mentioned above, using only the transmitted signal that impinges upon the satellite, the emitter location is to be estimated knowing only the center frequency and modulation type. Additionally, geolocation estimates must be obtained computationally efficient enough to be computed on the satellite's onboard processing unit.

2.2 Prior and Contemporary Solutions

Current SSG solutions generally involve either an angle-of-arrival (AoA) or a Doppler-based approach. AoA-based algorithms [55, 68, 27, 30] offer simple solutions but are limited to high signal strength scenarios, long acquisition times, relatively stationary targets, and high precision satellite pointing accuracy - providing limited geolocation accuracy in limited situations. Doppler-based algorithms are governed by highly nonlinear equations but offer better information on the emitter and higher accuracy capabilities and are therefore the focus of this Dissertation's proposed geolocation solutions. The processing methodology for single or multiple satellite RF geolocation systems using a Doppler-based approach is generally the same. A single satellite receives and stores data. When a ground station is

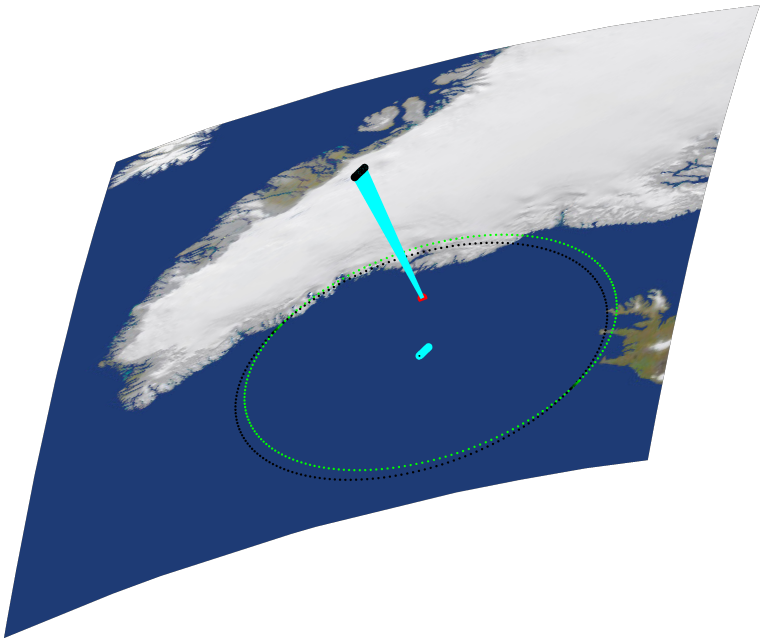

Figure 2.1: A standard scenario for RF Emitter Geolocation. The red dot is the emitter while the satellite moves overhead in black. The sub-satellite path and range vectors are in cyan while the antenna footprints are also shown at time zero (black dots) and five seconds later (light green dots).

available, the stored data is downlinked. Geolocation estimates are then obtained through post-processing with a chosen algorithm.

The use of received Doppler for geolocation was largely pioneered by research scientists at the Johns Hopkins Applied Physics Laboratory, who solved the orbit of Sputnik-1 by analyzing the Doppler shift of the satellite's transmitted signal in 1957 [14]. This technique quickly found its place in the Navy Navigation Satellite System (NNSS) (also known as Transit), the first satellite-based geopositioning system launched in 1960. Ground stations constantly looked for satellite-transmitted coherent carrier frequencies at 150 MHz and 400 MHz. At least one Doppler curve of about 2 minutes long was recorded from a satellite pass. Together, the Doppler curve(s), an initial estimated ground station position, the transmitted orbit parameters, and a Least Squares Estimator then produced a

refined location estimate of the ground station to within 100 meters of accuracy [64].

Search-and-rescue operations soon took advantage of the use of satellite Doppler for positioning in 1982 with the launch of the COSPAS-SARSAT (1979) satellite system, which is still in use today. Distress signals sent from approved emergency beacons are received by overhead satellites and sent to the ground station for post-processing to find the location of the beacon. Beacons output a pre-defined burst-mode lasting about a quarter of a second, repeated roughly every 50 seconds. Legacy beacons transmitted at 121.5 MHz and 243 MHz but have now migrated to 406 MHz beacons also transmitting GPS coordinates to the satellite. Historically, the COSPAS-SARSAT is a search-and-rescue system that usually requires at least two satellites, two transmissions, or two passes. However, with the advent of the 406 MHz GPS-bearing signal, a new constellation called MEOSAR was launched in 2016 that utilizes satellites in Medium Earth Orbit (MEO) to repeat the received beacon signals for ground processing - drastically increasing the geolocation accuracy [45].

Doppler geolocation was also implemented into ARGOS in 1978, a satellite-based system which collects environmental data from transmitting platforms worldwide. Two geolocation options are available, a Least Squares approach and a Kalman Filtering approach [5]. The Least Squares approach requires two transmissions per satellite pass to calculate a position and its mirror solution (the mirrored solution is often referred to as the 'antipode'). The Kalman approach uses an Interacting Multiple Models (IMM) approach where each model consists of an Unscented Kalman Filter (UKF) that models different movements of the RF emitters (beacons fastened on sea turtles, ships, buoys, etc.) and can be computed using a single transmission per satellite pass [46]. Both algorithms require

an initialization procedure of obtaining four transmissions in a single satellite pass.

Other past Doppler-based SSG algorithms utilize Nonlinear Least Squares and various forms of the Extended Kalman Filter (EKF) and can be found in [26, 44, 58]. There are two algebraic solutions - the first [51] is meant for rough initial geolocation estimates and is based on calculating Point of Closest Approach (PCA). The second [50] goes further by algebraically estimating the center frequency and then using an adaptive grid search to find the geolocation estimate. Additional solutions suggest using Doppler Rate combined with a grid search [28] and a Particle Filter (PF) approach meant for unmanned aerial vehicles that utilizes Doppler to estimate location and center frequency [69].

Theoretic performance bounds have long been used to measure the optimality of estimation techniques and for mission planning, however very few bounds exist for the SSG solution. Existing bounds generally assume a flat earth, fixed and known height above the emitter, and a straight line constant velocity flight path [51, 40, 42]. Some have incorporated a spherical earth and elliptical flight path but all have used the traditional CRB [69, 70].

2.3 The Proposed Solution Framework

Referring once more to the scenario described in Fig. 2.1, it is quickly apparent that none of the current and prior solutions are able to provide a geolocation solution. The acquisition time is too short, the assumptions are too strong, and the search area is too big. Additionally, no existing solutions are designed for the errors affiliated with SmallSats (oscillator and ephemeris) nor deal with transmitters whom may be made with cheap and uncalibrated clocks that exhibit oscillator errors much worse than those on SmallSats. Inaccuracies befitting useful geolocation ($\approx$ 1 km) are only currently obtained through the use of strong initialization

procedures, the use of multiple satellites or passes, or additional information that drastically decreases the search area. No available algorithm is meant for a single satellite, real-time processing, with only a single pass and limited signal duration, to find an uncooperative emitter.

A drastic change is needed to accommodate the requisites of crafting a geolocation system that handles short signal duration, single burst acquisitions scenarios, one satellite pass, no initialization procedures, oscillator and ephemeris errors, and no auxiliary signals in a computationally efficient manner befitting SmallSat onboard systems. From a design standpoint, four things need to be stipulated, and they are listed and described below:

1. **Measurements** that, from an information-criterion perspective, hold the most information concerning the origin of the emitted signal impinging upon the satellite.

2. A **State Vector** that provides the best estimation accuracy and stability. The SSG scenario can be posed in several different coordinate systems, each entailing a different set of state vectors.

3. A **Geolocation Algorithm** that maps the measurements to an emitter location unambiguously, quickly, and in a computationally efficient manner.

4. A **Theoretical Performance Bound** to gauge algorithmic optimality and for system design.

2.3.1 Measurements

An AoA-based approach utilizes raw IQ samples as the measurement quantity as they are received on the satellite. The corresponding geolocation algorithm is a power-based calculation that utilizes some form of peak finder over the pairs of

azimuthal and elevational values as measured from the satellite nadir. The highest peak corresponds to the highest power, and therefore yields the directional vector pointing towards the presumed emitter location. This vector then can be intersected with the Earth ellipsoid to obtain a location estimate. This approach is attractive as it allows for computationally cheap power calculations and is insensitive to oscillator drift. However, careful calibrations, long acquisition periods, and stationary emitters are strong requirements. It is also, due to the large range (slant) distances, extremely sensitive to ephemeris errors and pointing accuracy. An AoA-based approach is simply not applicable.

A Doppler-based approach, as the historical and current approaches suggest, is the most popular and effective. The emitted signal undergoes a Doppler shift brought about by the transceiver geometry and satellite motion, which is captured in the signal seen by the satellite. The shorter the range vector, the faster the range rate, and more location information is embedded within the received signal. The high speed of the satellite offers spatial diversity within a short period of time, allowing high geolocation accuracies. This approach requires an intermediate step of estimating the Doppler and a geolocation algorithm that can deal with a highly nonlinear measurement equation.

Yet, no matter how good the measurements of the Doppler are, no matter how efficient and accurate the geolocation estimation method used, there is a reason all contemporary approaches utilize additional satellites, satellite passes, or initialization procedures. A single satellite trying to geolocate a signal with only Doppler measurements possesses an extremely ill-conditioned solution space that is rife with ambiguities and heavily susceptible to noise and initialization error. Current techniques only use Doppler, but this dissertation utilizes both Doppler and Doppler Rate as measurement equations. The reasoning for using an

additional measurement (as well as further insight on why to use Doppler-based versus AoA-based approaches) follows from a derivation of the received signal.

The emitted signal is narrowband and sent at a center frequency f_c. It can be denoted as:

$$y_T(t) = \mathrm{Re}\{\tilde{s}(t)e^{j2\pi f_c t}\} \tag{2.1}$$

where $\tilde{s}(t)$ is the complex envelope of $s(t)$. If the emitter and the satellite have no respective motion, the impinging signal at the satellite can be expressed as:

$$\begin{aligned} y_R(t) &= y_T(t-\tau_k) \\ &= \mathrm{Re}\{\tilde{s}(t-\tau_k)e^{j2\pi f_c(t-\tau_k)}\} \text{ where } \tau_k = \frac{r_k}{c_0} \end{aligned}$$

The subscript k indicates a particular instant in time, r_k is the range from the emitter to the satellite, and c_0 is the speed of light. However, the satellites of interest travel as fast as 7.8 km/sec, making the range (r_k) time dependent, $r_k(t)$. The received signal at the satellite is now denoted as:

$$\begin{aligned} y_R(t) &= y_T(t-\tau(t_k)) \\ &= \mathrm{Re}\{\tilde{s}(t-\tau(t_k))e^{j2\pi f_c(t-\tau(t_k))}\} \\ &\approxeq \mathrm{Re}\{\tilde{s}(t)e^{j2\pi f_c(t-\tau(t_k))}\} \\ &= \mathrm{Re}\{\tilde{s}(t)e^{-j2\pi f_c\tau(t_k))}\} \end{aligned} \tag{2.2}$$

where

$$\tau(t_k) = \frac{r(t_k)}{c_0} \tag{2.3}$$

Note that it is assumed the phase of the impinging signal moves faster than $\tilde{s}(t)$ such that the change of $\tilde{s}(t-\tau(t_k)) \approxeq \tilde{s}(t)$ in the third line. This is known as the narrowband assumption. The last line has the carrier frequency term removed

and represents the basebanded signal. This derivation is loosely based off of the one found in [16].

The measurements desired are Doppler and Doppler Rate, denoted $z_1(t)$ and $z_2(t)$, respectively. As shown in Appendix 8.1, the Doppler and Doppler Rate can be shown in terms of the kinematic motion of the emitter and satellite. The satellite's position is $\mathbf{p}_s(t_k)$, its velocity $\mathbf{v}_s(t_k)$, and acceleration $\mathbf{a}_s(t_k)$. Likewise, the (assumed stationary for now) emitter's position is denoted as $\mathbf{p}_e(t_k)$. Therefore, Doppler and Doppler Rate can be written as:

$$\begin{aligned} z_1(t_k) &= \frac{1}{2\pi}\frac{\partial}{\partial t_k}\angle\tilde{y}_R(t_k) \\ &= \frac{1}{\lambda}\frac{\partial}{\partial t_k}|\mathbf{r}(t_k)| \\ &= \frac{1}{\lambda}\frac{\partial}{\partial t_k}|\mathbf{p}_s(t_k) - \mathbf{p}_e(t_k)| \\ &= -\left(\frac{1}{\lambda}\right)\underbrace{\left(\frac{\mathbf{v}_s^T(t_k)[\mathbf{p}_s(t_k) - \mathbf{p}_e(t_k)]}{|\mathbf{p}_s(t_k) - \mathbf{p}_e(t_k)|}\right)}_{v_r(t_k)} \end{aligned} \tag{2.4}$$

$$\begin{aligned} z_2(t_k) &= \frac{1}{2\pi}\frac{\partial^2}{\partial t_k^2}\angle\tilde{y}_R(t_k) \\ &= \frac{1}{\lambda}\frac{\partial^2}{\partial t_k^2}|\mathbf{r}(t_k)| \\ &= \frac{1}{\lambda}\frac{\partial^2}{\partial t_k^2}|\mathbf{p}_s(t_k) - \mathbf{p}_e(t_k)| \\ &= -\left(\frac{1}{\lambda}\right)\left(\frac{\mathbf{a}_s^T(t_k)[\mathbf{p}_s(t_k) - \mathbf{p}_e(t_k)]}{|\mathbf{p}_s(t_k) - \mathbf{p}_e(t_k)|} + \frac{|\mathbf{v}_s(t_k)|^2}{|\mathbf{p}_s(t_k) - \mathbf{p}_e(t_k)|} - \frac{v_r^2(t_k)}{|\mathbf{p}_s(t_k) - \mathbf{p}_e(t_k)|}\right) \end{aligned} \tag{2.5}$$

where $\lambda = \frac{c_0}{f_c}$ is the wavelength, $\tilde{y}_R(t_k)$ is the real and complex components of the received signal, and $|\cdot|$ denotes the Frobenius norm operation.

It is immediately apparent from Eq. 2.4 and Eq. 2.5 that the desired informa-

tion, $\mathbf{p}_e(t_k)$, is present in a highly nonlinear fashion. Further, $\mathbf{p}_e(t_k)$ occurs many times in the expressions and appears to largely govern the measurement values - this is good for estimation purposes. However, a deeper dive is required to fully realize this benefit.

For the scenario of a stationary emitter and a satellite as the receiver, Figure 2.2 describes the transceiver geometry and the governing kinematics. The satellite position vector, velocity vector, acceleration vector are in blue, green, and orange respectively as well as the emitter position vector in red. The range vector, $\mathbf{r}(t_k) = \mathbf{p}_s(t_k) - \mathbf{p}_e(t_k)$ can be seen as purple.

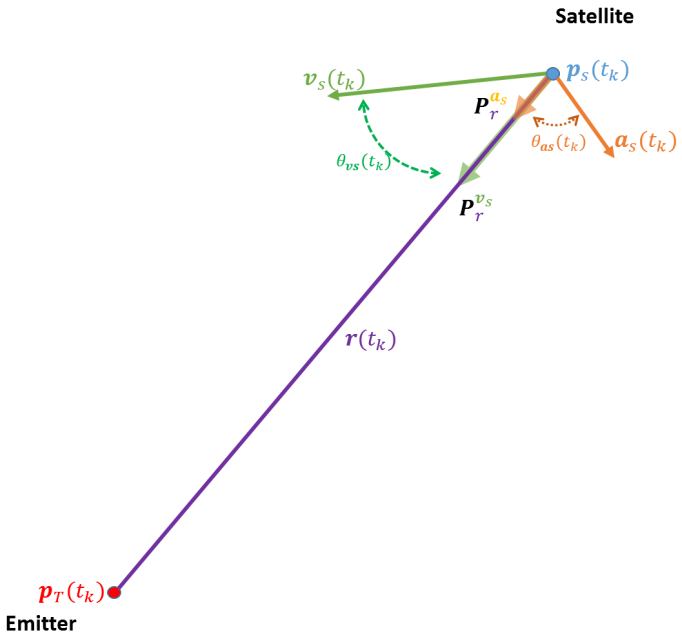

Figure 2.2: Kinematic representation of transceiver geometry as it pertains to inducing Doppler effects.

From a transceiver geometry-kinematic viewpoint, three properties govern the performance of a Doppler-based algorithm: $|\mathbf{r}(t_k)|$, $\mathbf{P}_r^{\mathbf{v}_s}(t_k)$, and $\mathbf{P}_r^{\mathbf{a}_k}(t_k)$. These terms represent the range vector length, the projection of the satellite velocity onto the range vector, and the satellite acceleration vector projection onto the range vector. The quantities can be defined as follows. $\mathbf{P}_r^{\mathbf{v}_s}(t_k)$ is the vector projection

of $\mathbf{v}_s(t_k)$ onto the range vector $\mathbf{r}(t_k)$. The angle between the range vector and the satellite velocity vector is $\theta_{vr}(t_k)$ and ranges from $0 \leq \theta_{vr}(t_k) \leq \pi$ and does not discriminate on whether the satellite velocity vector is pointing towards the emitter or away (and ambiguity). Similarly, $\mathbf{P}_r^{\mathbf{a}_k}(t_k)$ is the vector projection of $\mathbf{a}_s(t_k)$ onto the range vector $\mathbf{r}(t_k)$. The angle between the satellite acceleration vector and the range vector is $\theta_{ar}(t_k)$. This ranges from $0 \leq \theta_{ar}(t_k) \leq \pi$ and possesses the same ambiguity as $\theta_{vr}(t_k)$. These vector projections be generically defined (suppressing time) as:

$$\mathbf{P}_{\mathbf{y}}^{\mathbf{x}} = \frac{\mathbf{x}^T\mathbf{y}}{|\mathbf{y}|^2}\mathbf{y} \tag{2.6}$$

$$= \frac{|\mathbf{a}|}{|\mathbf{b}|}\cos(\theta_{xy})\mathbf{b} \tag{2.7}$$

Let the scalar projection be defined as:

$$P_{\mathbf{y}}^{\mathbf{x}} = \frac{\mathbf{x}^T\mathbf{y}}{|\mathbf{y}|} \tag{2.8}$$

$$= |\mathbf{x}|\cos(\theta_{xy}) \tag{2.9}$$

The question then arises of when is the usage of Doppler and Doppler Rate beneficial for geolocation. It is not the magnitude of the Doppler or the Doppler Rate that entails greater geolocation accuracy, but the rate at which they are changing. A faster changing Doppler and Doppler Rate entails that more information can be obtained from the measurements on the emitter position. This can be likened to having a greater aperture for an array of receivers, since a larger aperture means a greater diversity in measurements. The proposed algorithm is a real-time algorithm that parses short-duration signals so the ability to have as diverse (informative) measurements as possible is the key component. This

is synonymous with having a scenario whose transceiver geometry and motion characteristics provide the fastest changing Doppler and Doppler Rate.

An additional look at Eq. 2.4 is now warranted. Keeping in mind Fig. 2.2, Eq. 2.8 and Eq. 2.9:

$$
\begin{aligned}
z_1(t_k) &= -\left(\frac{1}{\lambda}\right)\left(\frac{\mathbf{v}_s^T(t_k)[\mathbf{p}_s(t_k)-\mathbf{p}_e(t_k)]}{|\mathbf{p}_s(t_k)-\mathbf{p}_e(t_k)|}\right) \\
&= -\left(\frac{1}{\lambda}\right)\left(\frac{\mathbf{v}_s^T(t_k)\mathbf{r}(t_k)}{|\mathbf{r}(t_k)|}\right) \qquad (2.10) \\
&= -\left(\frac{1}{\lambda}\right)\underbrace{|\mathbf{v}_s(t_k)|\cos\theta_{vr}(t_k)}_{\mathbf{P}_r^{\mathbf{v}_s}(t_k)} \qquad (2.11)
\end{aligned}
$$

Doppler is a scalar projection of the satellite velocity vector upon the range vector, scaled by the wavelength of the transmitted signal. The magnitude of the range vector is the most dominant factor in space geolocation since satellites travel up to 8000 meters per second but are located hundreds of kilometers from the emitter. Therefore, the denominator of Eq. 2.10 determines whether the Doppler effect will be negligible. The farther away the satellite and emitter are from each other, the less of a change in Doppler the satellite will see even at the satellite's closest point of approach (PoC).

The wavelength, a function of the center frequency divided by the speed of light, is a constant and has no ability to increase or decrease the information available to be learned about the emitter location. The angle between the range vector and the satellite velocity vector, $\cos\theta_{vr}(t_k)$ is seen in Eq. 2.11. It is congruent with the look angle of the emitter. From that standpoint, $\cos\theta_{vr}(t_k)$ will change faster when the satellite is closer to the emitter, thereby causing the angular velocity of the emitter look angle to increase. Directionality (whether the satellite is traveling towards or away from the emitter) is not discernable. This is what causes the "mirror" or "antipodal" solutions so often found in Doppler-based

approaches. Taking the derivative of Eq. 2.11 w.r.t. $\theta_{vr}(t_k)$ and setting it equal to zero yields $\theta_{vr}(t_k) = [0, \pi]$. Looking at Fig. 2.2, this result states that the fastest changing Doppler - in terms of the angle, $\theta_{vr}(t_k)$ - is obtained by moving directly at the emitter or directly away - or in other words, the velocity vector of the satellite is parallel with the range vector.

Fig. 2.3 demonstrates this analysis on Doppler for a satellite traveling a circular orbit at 500 km altitude receiving a signal sent by the emitter transmitting at 120 MHz. The left column shows a satellite traveling along a path (black line) with its current position marked in blue. The emitter's true position is in red. The Doppler error surface is produced by using Eq. 2.4 and varying $\mathbf{p}_e(t_k)$ over a grid of potential emitter locations at the given time point and satellite position (marked as a black dot). The Doppler error surface is a contour showing the amount of absolute error in the calculated Doppler when the chosen emitter location on the grid is plugged in from the true emitter position marked in red. The corresponding right column shows the Doppler curve over the passage of time and the current Doppler-Time point that corresponds to Doppler error surface directly to the left.

Note that the first two rows are the satellite approaching the emitter, the third row is the satellite at the closest location to the emitter, and the fourth row shows the satellite heading away from the emitter. Further, note that the third row, first column Doppler error contour plot shows the most density of lines - this aligns perfectly with the statement that the closer the satellite is to the emitter, the more informative the Doppler will be. The second point again shows more density of lines than the first and fourth point, but still less than the point of closest approach (3rd). An important facet to note about the Doppler error surface is that it showcases a surface that does not have a global minima - it is characterized

by lines. This corroborates with the statement that the Doppler solution space is rife with ambiguities. The flatness of the valley carved in the figures on the left column indicate why geolocation solutions solely based on Doppler need long acquisition times, very accurate initial guesses, or additional information to get the solution to converge.

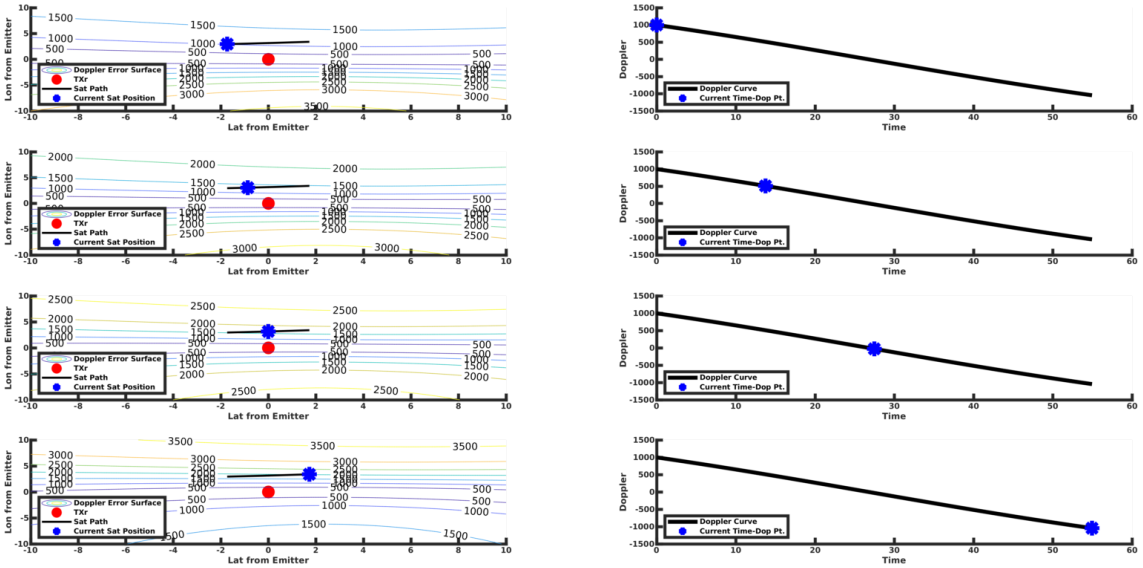

Figure 2.3: Effect of transceiver geometry and emitter estimates on Doppler as seen by the Satellite.

Looking now at the Doppler Rate:

$$z_2(t_k) = -\left(\frac{1}{\lambda}\right)\left(\frac{\mathbf{a}_s^T(t_k)[\mathbf{p}_s(t_k)-\mathbf{p}_e(t_k)]}{|\mathbf{p}_s(t_k)-\mathbf{p}_e(t_k)|} + \frac{|\mathbf{v}_s(t_k)|^2}{|\mathbf{p}_s(t_k)-\mathbf{p}_e(t_k)|} - \frac{v_r^2(t_k)}{|\mathbf{p}_s(t_k)-\mathbf{p}_e(t_k)|}\right)$$

$$= -\frac{1}{\lambda}\left(\underbrace{|\mathbf{a}_s(t_k)|\cos\theta_{ar}(t_k)}_{\mathbf{P}_r^{\mathbf{a}_s}(t_k)} + \frac{|\mathbf{v}_s(t_k)|^2}{|\mathbf{r}(t_k)|} - \frac{(|\mathbf{v}_s(t_k)|\cos\theta_{vr}(t_k))^2}{|\mathbf{r}(t_k)|}\right) \tag{2.12}$$

$$= -\left(\frac{1}{\lambda}\right)\left(\mathbf{P}_r^{\mathbf{a}_s}(t_k) + \frac{|\mathbf{v}_s(t_k)|^2}{|\mathbf{r}(t_k)|} - \frac{\left(\mathbf{P}_r^{\mathbf{v}_s}(t_k)\right)^2}{|\mathbf{r}(t_k)|}\right) \tag{2.13}$$

the geometric quantities in Fig. 2.2 are again present. The interpretation of Doppler Rate is not as straight forward as Doppler but it still provides tangible insights. The first time variant term in Eq. 2.13 is the projection of the satellite

acceleration vector upon the range vector and follows the same interpretation of the vector projection previously discussed in Eq. 2.11. Namely, the faster $\theta_{vr}(t_k)$ changes, the closer the satellite will be to the emitter. The second time variant term in Eq. 2.13 is an angle-independent term involving the squared magnitude of the satellite's velocity vector divided by the range length. A satellite's velocity magnitude will change in negligible amounts over the intended (short-duration) acquisition period, so only the range distance will chance causing this term to fade in and out of the equation as the satellite moves closer and away from the emitter. The last time varying term is simply the scalar projection from the Doppler expression Eq. 2.11 squared divided by the range. This term is again governed by the proximity of the satellite to the emitter as well as its directionality as stated before concerning $\theta_{vr}(t_k)$. Setting Eq. 2.12 equal to zero and taking the derivative w.r.t. $\theta_{ar}(t_k)$ yields $\theta_{ar}(t_k) = [0, \pi]$. This is the same result as with $\theta_{vr}(t_k)$, but because of the orbital mechanics of satellite motion, the acceleration vector will point towards the Earth. Unless hurtling directly towards the emitter, the satellite will not provide a maximal angle for acceleration. Note that this inherent dissimilarity in the projections of the satellite velocity and acceleration vector upon the range vector avoids mirror solutions. The periodicity of the cosine term that creates the ambiguity in Eq. 2.11 is broken by the appearance of two additional terms. This is very important for estimation purposes and solidifies the use of both Doppler and Doppler Rate measurements to glean information on the emitter location.

Fig. 2.4 demonstrates the same scenario as Fig. 2.3 but instead plots the Doppler Rate error surface in the left column and the Doppler Rate on the right column. Once more, the denser lines are at the point of closest approach (row 3), and the "looser" lines appearing when the satellite is farther away. What is

different is the manner that these lines appear on the error surface - they are concentric circles clearly showing a global minima. When the satellite is far away (rows 1 and 4), the minima is a flat basin but as more information is gleaned from the received signal, it begins to deepen to an unambiguous minima as seen in rows 2 and 3. This is pivotal, the inclusion of the Doppler Rate as a measurement equation successfully mitigates the ambiguities plaguing purely Doppler-based approaches.

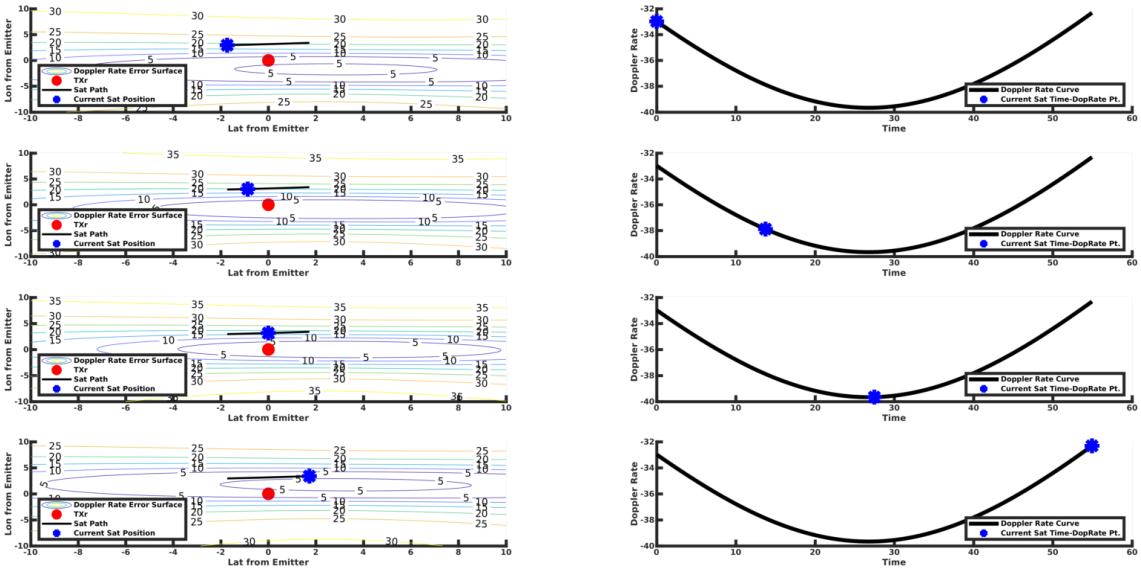

Figure 2.4: Effect of transceiver geometry and emitter estimates on Doppler Rate as seen by the Satellite.

2.3.2 State Vector and Constraints

While the choice of Doppler and Doppler Rate measurements provide a respectable amount information on the emitter, the solution space remains very ill-conditioned. A long acquisition time would help this drastically, but the aim of this solution is to be able to geolocate short duration (single second) signals. Further choices must be made to make the solution space as small and convergent as possible. The emitter location is the parameter of interest, but no assumptions

have been strictly stipulated on the emitter movement or which coordinate frame it should be placed in.

From this point on it is assumed that the emitter is both stationary and sitting upon the Earth's ellipsoidal surface. This constraint is validated in that the Earth's surface is 71 percent water, so all ships and buoys can be considered stationary or approximately stationary with respect to the satellite's velocity. As such, for most earth-bound emitters, if the Latitude and Longitude are known then the Altitude can be reliably approximated by cross-referencing with a Digital Terrain Elevation Data (DTED) map. While the constraint is an obvious one, the ability to implement it on an onboard algorithm upon the satellite in a manner that is not an exhaustive search is not trivial. One of the main contributes of this dissertation is a methodology for doing this in a computationally cheap, analytic fashion.

There exists a variety of coordinate frames including ECEF and Earth Centered Inertial (ECI) that each offer their own benefits and costs in different scenarios. Each represent the emitter location in terms of 3 state variables. This outnumbers the number of available measurements (2) and contributes to the ill-conditioned nature of the solution space. The addition of more parameters that must be estimated in order to obtain an estimate of the emitter location must be avoided to further deterioration of the solution space. The ECI coordinate frame is Cartesian and has the center of the Earth as its origin and does not rotate with respect to the stars. However, this means that even for a stationary emitter on the Earth, the emitter has a movement component that cannot be ignored and must be estimated. The emitter's position, velocity, and acceleration components in x,y, and z creates 9 parameters that must be estimated which is prohibitively large for a single receiver producing two measurements. For this reason, the ECEF

coordinate system will be used. In this framework, the Earth is held stationary so an object sitting on its surface without any motion of its own will not appear to be moving to the rotating satellite. In other words, a stationary emitter has no Earth-relative velocity component because it is moving with the Earth.

Therefore, the emitter position, denoted $\mathbf{p}_e(t_k)$, constitutes the state vector

$$\mathbf{x}_k = \mathbf{p}_{e(k)} = \begin{bmatrix} p_e^x(t_k) & p_e^y(t_k) & p_e^z(t_k) \end{bmatrix}^T \tag{2.14}$$

Note that there has been a slight notational change. From now on, to better accommodate the host of literature in nonlinear filtering and general readibility, the parenthetical time annotation for the state vector will be written as a subscript, $\mathbf{x}_k$. The notation of time varying components not being estimated, such as $\mathbf{p}_s(t_k)$, will be written as $\mathbf{p}_{s(k)}$, with the discrete time component placed in paranthesis in the subscript. As another example, the satellite velocity will now be denoted as $\mathbf{v}_{s(k)}$ and acceleration as $\mathbf{a}_{s(k)}$.

Since the emitter is stationary, a relationship of this quantity over time can be expressed as:

$$\mathbf{x}_{k+1} = \mathbf{x}_k \tag{2.15}$$

The knowledge that the emitter sits upon the surface of the earth is a state constraint. This constraint can be written as:

$$\begin{aligned} \mathbf{0} &= \mathbf{g}_k(\mathbf{x}_k) \\ 0 &= \frac{\left(x_k^{(1)}\right)^2}{R_{eq}^2} + \frac{\left(x_k^{(2)}\right)^2}{R_{eq}^2} + \frac{\left(x_k^{(3)}\right)^2}{R_p^2} - 1 \end{aligned} \tag{2.16}$$

where R_{eq} and R_p are earth's equatorial radius and polar radius, respectively and $x_k^{(n)}$ refers to the nth component of the state vector in Eq. 2.14.

A thorough portrayal of the solution space can now be formulated and is shown in Fig. 2.5. In the figure, the solution space using the proposed state and measurement equations is shown using the same exact parameters that governed Fig. 2.1. Greenland can be seen on the figure, surrounded by water. The satellite is the black dot, the emitter the red dot. The light green line is the range vector.

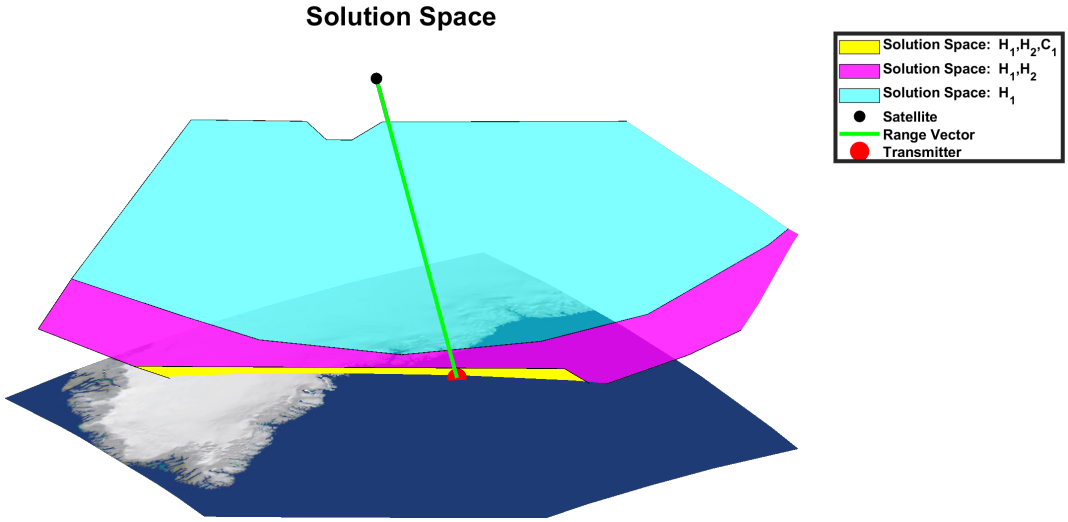

Figure 2.5: Depiction of solution space improvement offered through the use of two measurement equations and an earth surface constraint. H_1 is the Doppler measurement equation, H_2 is the Doppler Rate measurement equation, and C_1 is the earth surface constraint. This depiction follows the example scenario laid out in Fig. 2.1. The satellite is depicted as a black dot, the emitter as a red dot, and the range vector outlined in green.

Various shaded regions (light blue, magenta, yellow) intersect the figure. These shaded regions represent the solutions spaces offered from different choices of measurements and state spaces and their respective tolerances to measurement error. The shaded regions are generated using the following methodology. An Earth Centered Earth Fixed coordinate system is assumed, so the state space representing the unknown emitter location concerns an x-y-z coordinate. Current techniques utilize Doppler as measurements (H_1). This dissertation proposes the use of both the Doppler (H_1), Doppler Rate (H_2), and a state Earth-bound constraint C_1).

Only the first time sample is considered, where the received Doppler at $t_k = 0$ is $z_1(0) = 574.98$ Hz and the Doppler Rate $z_2(0) = -17.024$ Hz/sec. The values are obtained from the analytic form of the incident signal (Eq. 2.21 and Eq. 2.24) upon the satellite. The figure is generated by varying all possible values of the emitter position and plugging into the measurement equation(s). If the generated value(s) of the measurements come within 2.5% of their true values ($\begin{bmatrix} 574.98 \text{ Hz} & -17.024 \text{ Hz/sec} \end{bmatrix}^T$) then the point is shaded.

The large light blue hyperboloid surface (H_1) represents the solution space for techniques that only use Doppler (Eq. 2.4). To reiterate, all values within the light blue space represent an emitter position estimate that, when plugged into the measurement equation for Doppler, yields a measurement value within 2.5% of the true value. This suggests that only a little deviance in the state estimate (emitter location) yields a very believable measurement. This does not bode well for estimation purposes. An error tolerance of 2.5% is very easily attained when marginal ephemeris errors, oscillator errors, and even only additive noise is present. The inclusion of both Doppler and Doppler Rate (Eq. 2.4 and Eq. 2.5, denoted as H_1 and H_2 in Fig 2.5) is portrayed by the magenta arc overlapping a much smaller portion of the previous solution space. Note, the solution space generated by the Doppler Rate (H_2) intersects the solution space generated by the Doppler (H_1), producing a much smaller and well-defined space. The narrow strip of yellow incorporates the earth-bound constraint in addition to Doppler and Doppler Rate (Eq. 2.4, Eq. 2.5, and Eq. 2.16, denoted as H_1, H_2, and C_1 in Fig 2.5). It clearly provides a much smaller solution space and allows the geolocation algorithm to deal with spurious or systemic noise rather than ill-conditioned error surfaces. The result is a nonlinear estimation algorithm that is able to yield much more accurate, versatile, convergent, and efficiently computed answers.

2.3.3 The Geolocation Solution

The choice of measurements suggests a specific geolocation processing chain once energy has been detected by the satellite receiver.

1. Estimation of the Instantaneous Frequency (Doppler) and the Derivative of the Instantaneous Frequency (Doppler Rate)

2. The Mapping of the Doppler and Doppler Rate to an Emitter Location

This dissertation exclusively focuses on the second step. The first step can be done in a variety of ways (see [9, 10, 13]) and is left to the interested reader to choose based on their desired application. The estimation methods used in this dissertation will be outlined in the Section 5 when applicable.

But what can be taken from the first step is to note that it generates a sequence of noisy measurements made on a system governed by a state vector. There must be a model that relates the evolution of the state over time (Eq. 2.15, a linear equation), a constraint on the state equation (Eq. 2.16, a nonlinear equation), and a model relating the noisy measurements to the evolving states (Eq. 2.4 and Eq. 2.5, highly nonlinear equations). The noise portions are statistically defined and therefore stipulate a probabalistic state-space formulation. This problem is perfectly posed for nonlinear filtering.

The classic nonlinear filtering problem with an equality constraint can be written as:

$$\mathbf{x}_{k+1} = \mathbf{f}_k(\mathbf{x}_k, \mathbf{w}_k) \tag{2.17}$$

$$\mathbf{0} = \mathbf{g}_k(\mathbf{x}_k) \tag{2.18}$$

$$\mathbf{z}_k = \mathbf{h}_k(\mathbf{x}_k, \mathbf{v}_k) \tag{2.19}$$

where $\mathbf{x}_k$ is the $(L \times 1)$ state vector at time instant k and $\mathbf{z}_k$ is the $(N \times 1)$ measurement vector, $\mathbf{f}_k$ and $\mathbf{h}_k$ are nonlinear functions, and $\{\mathbf{w}_k\}$ and $\{\mathbf{v}_k\}$ are independent white noise processes of the state and measurement equations, with zero mean and covariances $\mathbf{Q}_k$ and $\mathbf{V}_k$, respectively.

The constrained nonlinear filtering equations Eqs. 2.17-2.19 utilized for both the proposed geolocation solution and the derived theoretic performance bound can now be explicitly written as:

$$\mathbf{x}_{k+1} = \mathbf{x}_k + \mathbf{w}_k \tag{2.20}$$

$$0 = \frac{\left(x_k^{(1)}\right)^2}{R_{eq}^2} + \frac{\left(x_k^{(2)}\right)^2}{R_{eq}^2} + \frac{\left(x_k^{(3)}\right)^2}{R_p^2} - 1 \tag{2.21}$$

$$\mathbf{z}_k = \mathbf{h}_k + \mathbf{v}_k \tag{2.22}$$

$$= \begin{bmatrix} h_k^{(1)}(\mathbf{x}_k) \\ h_k^{(2)}(\mathbf{x}_k) \end{bmatrix} + \begin{bmatrix} v_k^{(1)} \\ v_k^{(2)} \end{bmatrix} \tag{2.23}$$

$$= \begin{bmatrix} -\left(\frac{1}{\lambda}\right)\left(\frac{\mathbf{v}_{s(k)}^T(\mathbf{p}_{s(k)}-\mathbf{x}_k)}{|\mathbf{p}_{s(k)}-\mathbf{x}_k|}\right) \\ -\left(\frac{1}{\lambda}\right)\left(\frac{\mathbf{a}_{s(k)}^T(\mathbf{p}_{s(k)}-\mathbf{x}_k)}{|\mathbf{p}_{s(k)}-\mathbf{x}_k|} + \frac{|\mathbf{v}_{s(k)}|^2}{|\mathbf{p}_{s(k)}-\mathbf{x}_k|} \cdots \right. \\ \left. \cdots - \frac{\left(\frac{\mathbf{v}_{(k)}^T(\mathbf{p}_{s(k)}-\mathbf{x}_k)}{|\mathbf{p}_{s(k)}-\mathbf{x}_k|}\right)^2}{|\mathbf{p}_{s(k)}-\mathbf{x}_k|}\right) \end{bmatrix} \\ + \mathbf{v}_k \tag{2.24}$$

There are a trove of nonlinear filtering approaches that have been developed over the past half century. All roughly take the same general Bayesian approach to dynamic state estimation in that they all try to construct the *posterior* probability density function (pdf) of the state based on a series of noisy measurements [56]. For this scenario, an estimate is required at each new measurement, so a recursive filter is utilized which means the data is processed sequentially rather than in a

batch process. This is is pivotal as the entirety of the dataset does not need to be stored or reprocessed once a new measurement becomes available.

The entire premise of the Bayesian approach is to recursively quantify with a measurable confidence the state vector $\mathbf{x}_k$ at the sample k given the data $\mathbf{Z}_k$. Constructed in a statistical sense, this forms the Posterior pdf $p(\mathbf{x}_k|\mathbf{Z}_k)$. The optimal Bayesian solution is formed from two recurrence relationships that form the two stages that nonlinear recursive filters are comprised of: prediction and update.

The prediction stage assumes that the pdf $p(\mathbf{x}_{k-1}|\mathbf{Z}_{k-1})$ is available and that the transitional probability $p(\mathbf{x}_k|\mathbf{x}_{k-1})$ can be defined by Eq. 2.17. It is also worth noting that Eq. 2.17 is a Markov process of order one, and as such:

$$p(\mathbf{x}_k|\mathbf{Z}_{k-1}) = \int p(\mathbf{x}_k|\mathbf{x}_{k-1})p(\mathbf{x}_{k-1}|\mathbf{Z}_{k-1})\partial\mathbf{x}_{k-1} \tag{2.25}$$

When the measurement comes available at time k, $\mathbf{z}_k$, the update stage then involves an augmentation of the prediction (prior) pdf through the use of Bayes' Rule:

$$p(\mathbf{x}_k|\mathbf{Z}_k) = \frac{p(\mathbf{z}_k|\mathbf{x}_k)p(\mathbf{x}_k|\mathbf{Z}_{k-1})}{p(\mathbf{Z}_k|\mathbf{Z}_{k-1})} \tag{2.26}$$

where the denominator connects with Eq. 2.19 and its affiliated noise statistics. The ability to define $p(\mathbf{x}_k|\mathbf{Z}_k)$ allows an optimal state estimate to be computed versus many criterion. However, except for a few special cases, the analytic solutions of Eq. 2.25 and Eq. 2.26 cannot be found. As such, approximations must be made and a wide variety of suboptimal nonlinear filters are available to be chosen. Each come with their own strengths, caveats, and malleability to each application scenario.

There are many methods of describing the classes of these suboptimal Bayesian nonlinear filters. Here, four classes are adopted [56]: Analytic approximations, Numerical approximations, Multiple Model filters, and sampling approaches. Analytic approximations include the EKF and its many variants. The analytic approximation comes in the form of linearizing Eq. 2.17 and Eq. 2.17 if they are nonlinear. The EKF always approximates the posterior density as Gaussian, so if the nonlinearity is particularly pronounced, its performance will suffer greatly. Furthermore, the linearization comes in by the use of a Jacobian - a derivative-based approach - and is therefore highly susceptible to initialization errors. EKF variants (such as the iterated EKF) have been made to mitigate these errors but massive loads in complexity are required. Regardless, the EKF can be an excellent approach that is very fast to compute.

Numerical methods involve some form of numerical integration to solve the unsolvable integrals involved with the recurrence relationships in Eq. 2.25 and Eq. 2.26. This is done using a grid-based method to discretize the integration variables, which then leads to a summation over the integral(s). These can be highly effective but are limited to small search spaces and often cumbersome adaptable searches. These have been applied in Hidden Markov Model (HMM) filters very successfully in speech processing.

Multiple Model (MM) approaches approximate the posterior density by a weighted sum of Gaussian density functions. If the distribution is multi-model, this technique can be very effective. However, the computational burden is high as the number of densities grows. Furthermore, the estimation of the number of densities is a massively complex problem in of itself.

Of the sampling approaches, there are two in particular of special interest. The first is the Unscented Kalman Filter (UKF) which utilizes the Unscented

Transform in the EKF framework. Instead of approximating any nonlinear function in Eqs. 2.17-2.19, the posterior is approximated by the use of deterministic sample points. There is an assumption of a symmetric distribution, a slightly less stringent requirement that allows greater modeling abilities and modest computational requirements when compared to the EKF. There are many variants of the UKF that actually fall under a more general class of linear regression Kalman filters. All of these use the same filtering equations but vary in how they select their points. Particle filters (PFs) are a different class but also a sampling approach. They perform a sequential Monte Carlo estimation based on randomly formed probability densities. In general, it is not possible to effectively sample the posterior density, and so a vast array of PF-variants exist to most efficiently sample the approximate posterior density with the greatest stability. PFs are still known to be computationally expensive.

There are two geolocation solutions provided in this paper. One is a UKF variant and the other is a PF variant. There is an obvious need for the solution to be computationally efficient. Therefore, a recursive solution is a must - the storage of the entirety of the data chain or the use of it to make an estimate at each measurement is prohibitively large in terms of storage size and computational requirements. The Kalman framework perfectly fits these needs. However, the heavy nonlinearity in Eq. 2.19 points immediately at the usage of the UKF. Further, the constraint Eq. 2.18 must be used to obtain a less ill-conditioned solution space. Constraints, as mentioned, greatly help the geolocation solution but introduce odd nonlinearities in the error distributions and the probabilistic Bayesian modeling must handle that. Again, the UKF and PF frameworks speak to this. Because of these reasons, a UKF-based algorithm was chosen as the framework for the scenarios where the error distributions (posterior) are expected to be rel-

atively symmetric. UKFs require symmetric distributions but are well suited to be robust to occasional higher order moments in the error distribution. When the posterior density is expected to exhibit consistently non-symmetric scenarios, a geolocation algorithm based on the PF that utilizes the cUKF as a proposal distribution is designed. Each algorithm is designed to efficiently incorporate the Earth-bound constraint of the emitter.

2.3.4 The Theoretic Performance Bound

The geolocation algorithms are realized by the use of a nonlinear iterative estimation algorithm. It was also established that these types of filters are sub-optimal. In order to gauge how well-designed they are, there must be a way to measure how far from optimal they are. From the review of past and existing solutions, it is apparent that none of the prior bounds for the SSG scenario exist to properly gauge its algorithmic optimality. All took unrealistic geometric assumptions in either the Earth model or the flight path of the satellite and utilized the traditional Cramér-Rao Bound (CRB). Consequently, these prior performance bounds are often rendered non-canonical and are poor candidates for nonlinear, iterative algorithmic comparison.

Consequently, a recursive constrained Posterior Cramér-Rao Bound (rcPCRB) is derived and computed that provides a measure of mean squared error optimality for the cUKF and cUPF. It is uniquely suited in that it is a bound meant to gauge iterative nonlinear estimation algorithms. The bound is a culmination of developments on the CRB by [66, 65, 59, 19] and [20] that quantifies information measures from both the state and measurement equations. Its iterative nature is a drastic improvement on current performance bounds which only properly accommodate block processing algorithms.

Both the proposed geolocation solutions (cUKF and cUPF) and the derived theoretic performance bound (rcPCRB) utilize Eqs. 2.17-2.19.

2.3.5 Validation Approach

Beyond theoretical performance bounds, further validation is needed to prove algorithmic capability at the real-world level. In order to accomplish this, both simulated scenarios was generated and real world off-the-air IQ data was obtained from the TDS-1 satellite.

The artificial data comes from a complex simulation environment written entirely from scratch. Orbital mechanics are utilized to govern the satellite trajectory and the Earth follows the WGS 84 ellipsoid standards. An entire link budget has been implemented allowing the user to accurately model many real-world scenarios. The impinging signal is imbued with the phenomena incurred by the transciever motion using the derivations provided in previous sections. Actual waveforms with specific modulations are incorporated into a passband and eventually baseband signal. Estimates of Doppler and Doppler Rate are not analytically derived (model + noise) but are instead estimated using cyclo-stationary techniques as would be used in the field. This represents a more realistic scenario. Further, it was identified that ephemeris errors and oscillator errors would heavily affect geolocation accuracy and their respective formulation and derivation are shown below.

Ephemeris Errors

GPS is a mature and widely used positioning system for satellites in LEO, most of which only utilize a coarse acquisition (C/A) code and L1 phase measurements [22] or off-the-shelf, downsized adaptations of dual-frequency GPS receivers

[57, 29]. For this paper, it is assumed the LEO satellite has one of these two types of GPS receivers onboard. These receivers are susceptible to errors induced by satellite geometry, ionospheric effects, ephemeris errors, satellite clock errors, multipath distortion, tropospheric effects, and numerical errors [63].

Errors are often quantified - for position and velocity - in terms of radial, tangential, and normal errors. The radial, on-track, and cross-track component form an orthogonal coordinate system with the origin placed upon the current satellite position. The radial component shoots in a geodetic fashion towards the earth surface. The on-track axis lies upon the satellite position, pointing in the same direction as the satellite velocity vector. The cross-track forms a two dimensional plane with the on-track axis.

The positional error quantities are quantified as a zero-mean Gaussian Random Variables (GRV) along this coordinate system. The radial component will have the largest standard deviation (σ_{pr}). This is expected as the vertical component is the most sensitive in the dilution-of-precision for single-point solutions, with most errors falling between ± 5 meters. The on-track and cross-track components (σ_{po} and σ_{pc}, respectively) are typically less than ± 2.5 meters [29]. Pending on the quality of the GPS receiver, often the mean of the position errors are near zero, but can exhibit bias in the radial error estimates [22] up to 10 meters when only a single-frequency GPS receiver is used without additional onboard processing. The case of a radial bias is not considered here. Errors (in the vector norm sense, $|\mathbf{v}_e|$) in velocity average 0.34 meters per second with minimal values reaching 0.27 meters per second and maximal errors being 0.48 meters per second [6].

Based on the manner these error quantities are reported, numerical values based on experimental and simulated results published in [22, 57, 63, 6, 29] will be used in this paper. Each of these papers pertain to LEO satellites utilizing the

same quality of electronics as would be expected for the technology presented in this paper. Table 2.1 summarizes the ephemeris errors sets that will be evaluated in this paper: The parameters are radial error (σ_{pr}), on-track error (σ_{po}), cross-

Table 2.1: Table of Positional Error Distribution Values

Set	σ_{pr}	σ_{po}	σ_{pc}	$\lvert v_e \rvert$
1	1.5 m	1.0 m	1.0 m	0.27 m/s
2	8.0 m	4.0 m	4.0 m	0.48 m/s
3	12.0 m	5.5 m	5.5 m	1.0 m/s

track error (σ_{pc}), and the (3×1) velocity error ($\mathbf{v_e}$). The values are taken from the sources listed in references [22, 57, 63, 29] and [6]. and represent the best, average, and worst quoted performances of small LEO satellite GPS systems. The drawn positional error values are simply added onto the truth values and propagated through the geolocation algorithms as usual. The velocity error is incurred by an additive error vector (onto the true velocity vector) whose components are drawn from a zero mean distribution with a standard deviation equal to the magnitude given in Table 2.1. It is assumed these error distributions are zero mean.

Oscillator Errors

In single sensor Doppler-based geolocation oscillator drift is a serious concern. Assume the reading from the ith clock is $h_i(t)$. If the clock is perfect, then:

$$h_i(t) = t \tag{2.27}$$

However, all clocks possess inaccuracies and the off-the-shelf receivers and transmitters applicable for this technology will certainly possess a non-negligible amount of oscillator error and drift. The error quantification utilized here is based on the

clock error derived by [21]. The clock reading can be written as:

$$\phi_i(t) = \xi_i(t) + w_i(t) \tag{2.28}$$

where $\xi_i(t)$ is a GRV and $w_i(t)$ is a Weiner Process. The GRV has a mean of μ_i and variance σ_i^2 and the Weiner process comes from a zero mean process integrating (summing) over a random variable of variance ϵ_i^2, with $w(0) = 0$.

Using this clock model, denote the receiver clock as $h_R(t)$ and the transmitter clock as $h_T(t)$. They are defined as:

$$h_T(t) = t + \phi_T(t) \tag{2.29}$$

$$h_R(t) = t + \phi_R(t) + \phi_J(t) \tag{2.30}$$

where $\phi_T(t)$ is the transmitter oscillator error, $\phi_R(t)$ is the receiver oscillator error, and $\phi_J(t)$ is receiver jitter, specified from datasheets. Generally, datasheets give a phase noise specification that can be modeled as a GRV. Then, using Eq. 2.1, the transmitted signal can be expressed as:

$$y_T(t) = \mathrm{Re}\{\tilde{s}\Big(h_T(t)\Big)e^{j2\pi f_c h_T(t)}\} \tag{2.31}$$

$$= \mathrm{Re}\{\tilde{s}\Big(t + \phi_T(t)\Big)e^{j2\pi f_c\Big(t+\phi_T(t)\Big)}\} \tag{2.32}$$

When the transmitted signal undergoes a path delay $\tau(t_k) = \frac{r(t_k)}{c_0}$ (Eq. 2.3), the

received signal at the time instant t_k can be written as:

$$y_R(t) = \mathrm{Re}\{\tilde{s}\Big(t + \phi_T(t) - \tau(t_k)\Big)e^{j2\pi f_c\Big(t+\phi_T(t)-\tau(t_k)\Big)}\} \tag{2.33}$$

$$= \mathrm{Re}\{\tilde{s}\Big(t + \phi_T(t) - \tau(t_k)\Big)e^{j2\pi f_c\Big(t+\phi_T(t)-\tau(t_k)\Big)} \underbrace{e^{-j2\pi f_c\Big(t+\phi_R(t)-\phi_J(t)\Big)}}_{\text{Receiver Carrier Term}}\} \tag{2.34}$$

$$\approxeq \mathrm{Re}\{\tilde{s}(t) \underbrace{e^{-2\pi j f_c \phi_J(t)}}_{\text{Jitter Term}} \underbrace{e^{-j2\pi f_c \tau(t_k)}}_{\text{Doppler Term}} \underbrace{e^{j2\pi f_c\Big(\phi_T(t)-\phi_R(t)\Big)}}_{\text{Oscillator Term}}\} \tag{2.35}$$

Note that in Eq. 2.35 the narrowband assumption has been applied. The addition (or subtraction) of a Gaussian noise process (GNP) from a GNP is another GNP. The addition (or subtraction) of a Weiner process from a Weiner process is another Weiner process. Therefore:

$$\phi_T(t) - \phi_R(t) = \xi(t) + w(t) \tag{2.36}$$

where the mean of $\xi(t)$ is $\mu = \mu_T - \mu_R$ and variance $\sigma^2 = \sigma_T^2 + \sigma_R^2$. The Weiner process $w(t)$ is again zero mean but $\epsilon^2 = \epsilon_T^2 + \epsilon_R^2$. It is this form that the simulated data the proposed algorithm takes in, the exact values of which are drawn from Tables 2.1-2.2 and described in further detail in the Numerical Results section.

Table 2.2 shows the relevant values, representing standard values for a LEO GPS unit and a typical cheap RF transmitter taken from references [22, 57, 63, 29] and [6]. These values are used to obtain the statistical values of the oscillator noise for simulated algorithmic validation. The phase noise comes from the random variable $\xi(t)$, which gets its values drawn from Table 2.2. Additionally, the oscillator frequency accuracy for the transmitter and receiver is 5×10^{-11} which is used to produce the oscillator drift. The receiver jitter (τ_J) is 50×10^{-9}. This is implemented as a GNP added onto the incorporated time delays at each time sample.

Table 2.2: Table of Oscillator Error Values

Set	10 Hz	100 Hz	1 kHz	100 kHz	Units
1	-70	-113	-128	-140	dBc/Hz
2	-110	-120	-140	-150	dBc/Hz

The effects these oscillator errors will vary greatly depending on the quality of the oscillator and the frequencies involved. The three labeled terms - Jitter, Doppler, and Oscillator - in Eq. 2.35 will differ from scenario to scenario. Clearly, the higher the transmitted frequency, the greater the effects of the Jitter and Oscillator Term. However, higher transmitted frequencies generally exhibit much smaller errors. Optimizing oscillator error is a tradespace between oscillator quality, pricing, and the frequency of transmission.

Chapter 3

Geolocation Solutions

This chapter outlines the rationale, background theory, and the theoretical construction of the two geolocation solutions provided by this dissertation. The two solutions represent two different assumptions on the posterior density: one of approximate symmetry and one of non-symmetry. Each of these assumptions can reasonably be expected to be present in SSG scenarios and are described below.

The first solution is meant for scenarios where the expected error distribution is mostly symmetric. This geolocation solution takes the form of the constrained Unscented Kalman Filter (cUKF) and can be applied in situations where errors such as ephemeris and oscillator errors are mild or mitigated in some fashion such that the biases incorporated into the measurements do not differ drastically from the expected measurement model for a majority of the acquisition time.

When measurements are expected to exhibit large occasional deviance (bias) from the analytic model, a constrained Unscented Particle Filter (cUPF) has been derived that offers the same capabilities as the cUKF solution but with more tolerance to the aforementioned errors in measurements. It utilizes the cUKF as its proposal distribution and constantly resamples to avoid sample impoverishment. A methodology is laid out to keep the computational requirements roughly

Table 3.1: cUKF vs. cUPF

cUKF	**cUPF**
Computationally Efficient	Computationally Heavy
Approximately Gaussian Posterior	No Noise Density Constraints
Fast, Stable Convergence	Fast, Slightly Oscillating Convergence
Robust within Assumptions	Extremely Robust

comparable with the cUKF approach.

These two geolocation solutions far outstrip current methods in terms of geolocation accuracy within the scope of the intended geolocation scenario. When comparing the two approaches there are a set of very distinct tradeoffs, which are shown in Table 3.1.

Both of these solutions utilize the well known advantages of the Kalman Filter (KF). The KF is a technique well-suited for real-time processing and has modeling and uncertainty quantification abilities that far outstrip techniques such as Nonlinear Least Squares. Both the cUKF and cUPF also utilize a novel projection methodology meant to constrain the sigma points generated by the Unscented Transform into the usable solution space. This constraint allows the filter to generate geolocation solutions faster, with faster convergence, yielding higher geolocation accuracy.

The background theory governing the choice of a Kalman-based approach is described below. Additionally, the background theory and contributions within the choice of the cUKF and the cUPF is shown as well. The derivation of the constraint projection is outlined and demonstrated. A full computational cost profile is provided for each algorithm in terms of three types of floating point operations (FLOPs).

3.1 Low Measurement Bias Solution

3.1.1 Background Theory

The traditional UKF [35] is well known and is briefly outlined here. Recalling the classic nonlinear filtering problem expressed in Eqs. 2.17-2.19, the traditional KF assumes functions $\mathbf{f}$ and $\mathbf{h}$ are linear, and the state variables are Gaussian random variables (GRVs). Naturally, a GRV put through a linear system is again a GRV. When the system is nonlinear, characterizing the resulting distribution of the propagated GRVs is non-trivial. The UKF assumes the state distributions are Gaussian and represent the distributions as a set χ of $2L+1$ deterministic sample points called *sigma points*, where L is the number of states. The sigma points are calculated as shown below:

$$\begin{aligned}
\chi_0 &= \overline{\mathbf{x}}_{k-1} \\
\chi_i &= \overline{\mathbf{x}}_{k-1} + \zeta(\sqrt{\mathbf{P}_{x_{k-1}}})_i \text{ for } i = 1, \ldots, L \\
\chi_i &= \overline{\mathbf{x}}_{k-1} - \zeta(\sqrt{\mathbf{P}_{x_{k-1}}})_i \text{ for } i = L+1, \ldots, 2L
\end{aligned} \tag{3.1}$$

where $\overline{\mathbf{x}}_{k-1}$ is the sample mean and $(\sqrt{\mathbf{P}_{x_{k-1}}})_i$ denotes the ith column of the matrix square root of the covariance of the prior state estimates at time $t = (k-1)T_s$ with the desire to predict and estimate the state variables at time k where T_s is hte sampling interval. ζ is a scaling factor that determines the spread of the sigma points about the mean. These sigma points are then fed through the state and measurement equations, and the resulting distributions are approximated with weighted sample mean and weighted sample covariances. The time update

equations are:

$$\begin{aligned}
\chi^x_{k/t} &= f(\chi^x_t, \chi^w_t) \\
\hat{\mathbf{x}}^-_k &= \sum_{i=0}^{2L} w^m_i \chi^x_{k/t,i} \\
\hat{\mathbf{P}}^-_{x_k} &= \sum_{i=0}^{2L} w^c_i (\chi^x_{k/t,i} - \hat{\mathbf{x}}^-_k)(\chi^x_{k/t,i} - \hat{\mathbf{x}}^-_k)^T
\end{aligned} \tag{3.2}$$

Likewise, the measurement update equations are:

$$\begin{aligned}
\chi^z_{k/t} &= h(\chi^x_t, \chi^v_t) \\
\hat{\mathbf{z}}^-_k &= \sum_{i=0}^{2L} w^m_i \chi^z_{k/t,i} \\
\hat{\mathbf{P}}^-_{z_k} &= \sum_{i=0}^{2L} w^c_i (\chi^z_{k/t,i} - \hat{\mathbf{z}}^-_k)(\chi^z_{k/t,i} - \hat{\mathbf{z}}^-_k)^T \\
\hat{\mathbf{P}}^-_{x_k z_k} &= \sum_{i=0}^{2L} w^c_i (\chi^x_{k/t,i} - \hat{\mathbf{x}}^-_k)(\chi^z_{k/t,i} - \hat{\mathbf{z}}^-_k)^T
\end{aligned} \tag{3.3}$$

where the weights are calculated using the following equations:

$$w^m_0 = \frac{\lambda}{L+\lambda} \tag{3.4}$$

$$w^c_0 = \frac{\lambda}{L+\lambda} + (1 - \alpha^2 + \beta) \tag{3.5}$$

$$w^m_i = w^c_i = \frac{1}{2(L+\lambda)} \text{ for } i = 1, \ldots, 2L \tag{3.6}$$

The scalars α, β, and λ are used to taper the spread of the sigma points to the prior mean. Together, all of this allows the calculation of the final estimates where

the measurement and state estimates are fused together:

$$\begin{aligned} \mathbf{K}_k &= \hat{\mathbf{P}}^-_{xz_k}(\hat{\mathbf{P}}^-_{z_k})^{-1} \\ \hat{\mathbf{x}}_k &= \hat{\mathbf{x}}^-_k + \mathbf{K}_k(\mathbf{z}_k - \hat{\mathbf{z}}^-_k) \\ \hat{\mathbf{P}}_{x_k} &= \hat{\mathbf{P}}^-_{x_k} - \mathbf{K}_k\hat{\mathbf{P}}^-_{z_k}\mathbf{K}_k^T \end{aligned} \tag{3.7}$$

3.1.2 The constrained Unscented Kalman Filter (cUKF)

There are many methodologies for implementing constraints within the non-linear filtering framework, yet there is no general way of doing so. Excellent overviews can be found in [61] and [34], where it is suggested that constraint implementations fall under *pseudo-observation, projection* or *reparameterization* methods. Reparameterization is not applicable here due to complexities caused by the square roots in Eq. 2.21 and the usage of the ECEF coordinate system. Psuedo-observation puts the constraint as a noiseless measurement equation, but this causes a highly singular noise covariance which creates many practical difficulties concerning ill-conditioned covariances [61]. Therefore, the projection methodology has been chosen due to its applicability to this problem.

Projection can be used in EKFs, UKFs, and PFs. The use of projections in the particle framework is the basis of the second algorithm (described in the proceeding section). In general, the use of a PF with very small process noise runs the continual risk of sample impoverishment [7]. The EKF, due to its respectable modeling capabilities and superior computational efficiency is a rational choice and serves as the comparative basis in Section 5. Its formulation is provided below.

The cEKF projects the unconstrained estimate of the Kalman filter onto the constraint surface within the usual Kalman Filtering equations. This projection

can be expressed [61] as:

$$\tilde{\mathbf{x}}_k = \text{argmin}_{\mathbf{x}}(\mathbf{x} - \hat{\mathbf{x}}_k)^T \hat{\mathbf{P}}_{x_k}(\mathbf{x} - \hat{\mathbf{x}}_k) \tag{3.8}$$

$$\text{subject to: } \mathbf{D}\mathbf{x} = \mathbf{d} \tag{3.9}$$

where the positive-definite weighting matrix has been chosen to be the updated covariance matrix $\hat{\mathbf{P}}_{x_k}$ that obtains the maximum probability estimate of $\mathbf{x}$. The constraint can be implemented by taking a first order Taylor Expansion of the constraint, evaluated at the current state estimate as shown in [61]. For the Earth-bound constraint:

$$\mathbf{D} = \frac{\partial}{\partial \mathbf{x}}\mathbf{g}(\mathbf{x}) = \begin{bmatrix} \frac{2\mathbf{x}_k^{(1)}}{R_{eq}^2} & \frac{2\mathbf{x}_k^{(2)}}{R_{eq}^2} & \frac{2\mathbf{x}_k^{(3)}}{R_p^2} \end{bmatrix} \tag{3.10}$$

Therefore, Eq. 3.9 can be expressed as:

$$d = 1 - \mathbf{g}(\hat{\mathbf{x}}_k) + \mathbf{D}(\hat{\mathbf{x}}_k)\hat{\mathbf{x}}_k \tag{3.11}$$

The updated state estimate can then be written as:

$$\tilde{\mathbf{x}}_k = \hat{\mathbf{x}}_k - \hat{\mathbf{P}}_{x_k}\mathbf{D}^T(\mathbf{D}\hat{\mathbf{P}}_{x_k}\mathbf{D}^T)^{-1}(\mathbf{D}\hat{\mathbf{x}}_k - d) \tag{3.12}$$

As will be shown in Section 5, this cEKF formulation lacks the modeling capabilities for both the measurement equations and constraint equation. To remedy this, it is proposed to use a version of the cUKF, to better model the nonlinearity of the measurement equation. Further, a novel projection method was derived that takes each sigma point and quickly transforms them to the constraint surface. This avoids large grid searches or computationally expensive nonlinear programming problems [61, 36]. The process is succinctly outlined below:

Constrained Unscented Kalman Filter Algorithm

1. Calculate sigma points as in Eq. 3.1
2. Project sigma points that are not in the constrained solution space into the feasible region
3. Run projected sigma points through the time update equations as in Eq. 3.2
4. Project state estimates outside the constrained solution space into the feasible region using the Sigma Point Projection Algorithm
5. Run projected sigma points through Measurement-Update Equations as in Eq. 3.3
6. Run the Fusion Equations, Eq. 3.7
7. Repeat

This algorithm efficiently projects wayward sigma points to the closest feasible solution space, then recomputes the time and measurement update equations. Each point projection requires only 48 multiplications, 28 additions, 1 square root, and 10 trigonometry operations. Note the longitudal computation can be done in a variety of ways, but the arc tangent method was used in the computational cost analysis. Each sigma point $\mathbf{p}_\sigma = \begin{bmatrix} p_\sigma^x & p_\sigma^y & p_\sigma^z \end{bmatrix}^T$, is projected to the nearest point on the Earth's ellipsoid, $\mathbf{p}_{\hat{\sigma}} = \begin{bmatrix} p_{\hat{\sigma}}^x & p_{\hat{\sigma}}^y & p_{\hat{\sigma}}^z \end{bmatrix}^T$.

Sigma Point Projection Algorithm

1. Compute the Longitude of $\mathbf{p}_\sigma$, λ_σ

2. Rotate $\mathbf{p}_\sigma$ about the z-axis using the rotation matrix $\mathbf{R}_z(-\lambda_\sigma)$, so that the resulting point $\mathbf{p}_\sigma$ lies only on the x-z plane.

$$\mathbf{R}_z(\theta) = \begin{bmatrix} \cos\theta & -\sin\theta & 0 \\ \sin\theta & \cos\theta & 0 \\ 0 & 0 & 1 \end{bmatrix} \tag{3.13}$$

$$\hat{\mathbf{p}}_\sigma = \mathbf{R}_z(-\lambda_\sigma)\mathbf{p}_\sigma \tag{3.14}$$

3. Acquire the point of intersection of the geodetic line formed from $\hat{\mathbf{p}}_\sigma$ with the x-axis

$$\hat{\mathbf{p}}_i = \begin{bmatrix} \hat{p}_\sigma^x - \hat{p}_\sigma^z \tan(\pi - \lambda_\sigma) \\ 0 \\ 0 \end{bmatrix} \tag{3.15}$$

4. Rotate back the point $\hat{\mathbf{p}}_i$ using $\mathbf{R}_z(\lambda_\sigma)$ to obtain the original point of intersection $\mathbf{p}_i$ formed with the geodetic line created with $\mathbf{p}_\sigma$ and the xy-plane.

$$\mathbf{p}_i = \mathbf{R}_z(\lambda_\sigma)\hat{\mathbf{p}}_i \tag{3.16}$$

5. Using the line formed from points $\mathbf{p}_\sigma$ and $\mathbf{p}_i$, find the closest point of intersection (w.r.t. $\mathbf{p}_\sigma$) of the line and the ellipsoid formed from Eq. 2.21, $\mathbf{p}_{\hat{\sigma}}$.

$$\mathbf{p}_{\hat{\sigma}} = \begin{bmatrix} (1-s)p_i^x + sp_\sigma^x \\ (1-s)p_i^y + sp_\sigma^y \\ (1-s)p_i^z + sp_\sigma^z \end{bmatrix} \tag{3.17}$$

Where s is the line formed from points $\mathbf{p}_\sigma$ and $\mathbf{p}_i$ parameterized in arc length.

As is shown in Appendix 8.2, the constraint Eq. 2.21 is first reparameterized in terms of s then solved for with a simple quadratic detailed below:

$$s = \frac{-b + \sqrt{b^2 - 4ac}}{2a} \tag{3.18}$$

where

$$a = \frac{(p_i^x - p_\sigma^x)^2 + (p_i^y - p_\sigma^y)^2}{R_{eq}^2} + \frac{(p_i^z - p_\sigma^z)^2}{R_p^2} \tag{3.19}$$

$$\begin{aligned} b = &\frac{2p_i^x p_\sigma^x - 2(p_i^x)^2 + 2p_i^y p_\sigma^y - 2(p_i^y)^2}{R_{eq}^2} \\ &+ \frac{2p_i^z p_\sigma^z - 2(p_i^z)^2}{R_p^2} \end{aligned} \tag{3.20}$$

$$c = \frac{(p_i^x)^2 + (p_i^y)^2}{R_{eq}^2} + \frac{(p_i^z)^2}{R_p^2} - 1 \tag{3.21}$$

Results depicting this process are shown in Figure 3.1. The blue plane is the surface of the Earth. Unconstrained sigma points denoted in black are put through the steps outlined above and projected onto the earth's surface. The constrained sigma points are shown in green, with its new sample mean much closer to the true emitter position in red.

3.2 High Measurement Bias Solution

3.2.1 Background Theory

One of the four sub-optimal nonlinear filters was the category of grid-based approaches. These grid the solution space to compute the Posterior density recursively. A commonly used filter of this variant is the Point Mass Filter, but is heavily cursed by dimensionality with respect to the state vector size, grid size,

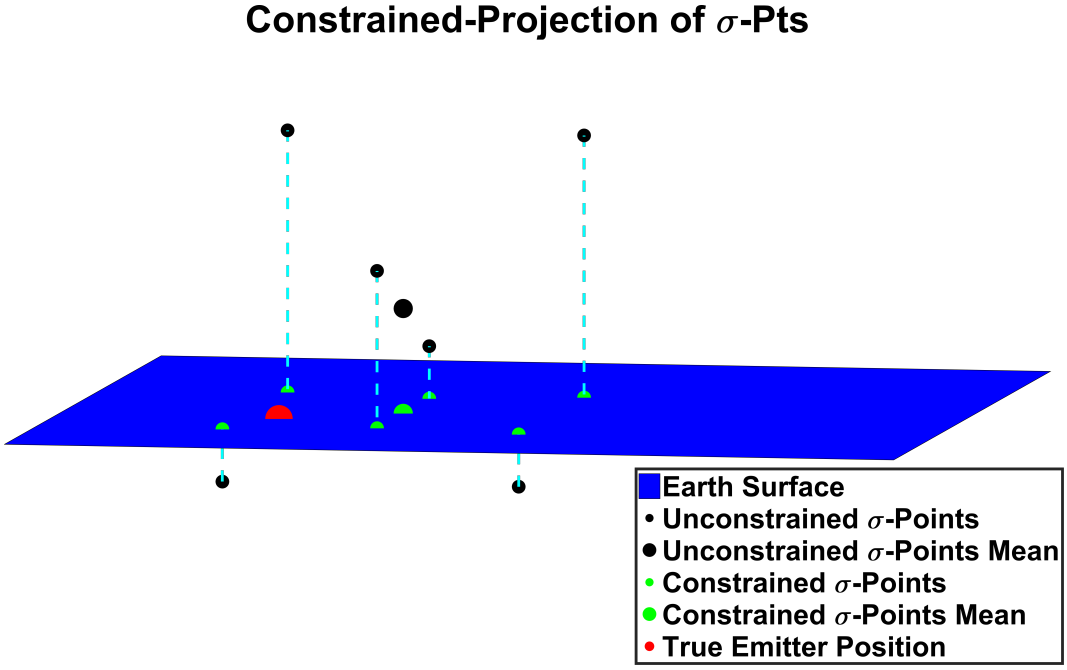

Figure 3.1: Depiction of the Sigma Point Projection Operation. The red dot denotes true position of the emitter. The black dots are the unconstrained sigma points which are put through the projection method to generate the constrained sigma points in green. The blue plane is the surface of the earth.

and is also quadratic in algorithmic complexity.

The Unscented Kalman Filter is a deterministic sampling of a finite set of grid points (the sigma points). The UKF uses a multivariate Gaussian assumption to have these deterministic sampling points generate an estimate of the Posterior density. The Particle Filter, on the other hand, provides a (numerical) approximation to the nonlinear filtering problem also with a grid, but the grid is adaptively selected in a stochastic fashion. Weights are used to adapt the grid for each particle (of which the set of N_p particles, make up the stochastic grid) to then approximate the Posterior density. The deterministic sampling offered by the UKF with $2L + 1$ sample points is now attempted with N_p particles.

A generic PF requires a proposal distribution, a resampling strategy, and a stipulated number of particles. A proper choice of a proposal distribution allows

the algorithm designer to sample from a simpler distribution than the desired and generally unattainable posterior distribution. This ability is obtained through *importance sampling*, which comes in many forms.

The theory governing this is as follows. Let $\mathbf{X}_k = \left[\mathbf{x}_j, j = 0, \ldots, k\right]$ represent the sequence of desired states. Let $\mathbf{Z}_k = \left[\mathbf{z}_j, j = 0, \ldots, k\right]$ be the sequence of measurements. Additionally let the joint posterior density and marginal density at time k be $p(\mathbf{X}_k|\mathbf{Z}_k)$ and $p(\mathbf{x}_k|\mathbf{Z}_k)$, respectively. Lastly, let $\left[\mathbf{x}_k^i, \mathbf{w}_k^i\right]$ denote a random measure that characterizes the joint posterior - this represents a set of support points with associated (normalized) weights.

Monte Carlo integration serves as a way to numerically evaluate a multidimensional integral and serves as the engine of all Particle Filters. Assume the following integral is to be evaluated:

$$I = \int \mathbf{g}(\mathbf{x}) \partial \mathbf{x} \tag{3.22}$$

Generally, Monte Carlo integration is set up where the factorization $\mathbf{g}(\mathbf{x}) = \mathbf{f}(\mathbf{x}) \cdot \pi(\mathbf{x})$ occurs. $\pi(\mathbf{x})$ is interpreted as a probability density function that, when N samples are drawn from it, the Monte Carlo estimate of the integral:

$$I = \int \mathbf{f}(\mathbf{x}) \pi(\mathbf{x}) \partial \mathbf{x} \tag{3.23}$$

is the sample mean:

$$I_N = \frac{1}{N} \Sigma_{i=1}^{N} \mathbf{f}(\mathbf{x}^i) \tag{3.24}$$

where $\left[\mathbf{x}^i, i = 1, \ldots, k\right]$ are the drawn samples. Additionally if these samples are independent then I_N is an unbiased estimate and will, according to the Law of Large Numbers, converge almost surely to I. The rate of convergence of the estimate is independent of the dimension of the integrand. It is worth noting that

deterministic sampling such as the UKF has a rate of convergence that decreases as the dimension of the integrand increases [56]. This highly useful property of MC integration comes from the assumption that the samples $\mathbf{x}^i$ come from parts of the state space that are informative to the integral. This directly translates in the Bayesian estimation context to $\pi(\mathbf{x})$ representing the posterior distribution. The posterior density, as is well known, is very difficult to sample from. One of the work-around methodologies is importance sampling.

The premise of importance sampling is the existence of a density, $q(\mathbf{x})$ that is similar to $\pi(\mathbf{x})$ in that it shares the same support:

$$\pi(\mathbf{x}) > 0 \rightarrow q(\mathbf{x}) > 0 \; \forall \; \mathbf{x} \; \in \; R^N \tag{3.25}$$

This allows the reformation of the integral to be written as:

$$I = \int \mathbf{f}(\mathbf{x}) \frac{\pi(\mathbf{x})}{q(\mathbf{x})} q(\mathbf{x}) \partial \mathbf{x} \tag{3.26}$$

Therefore the MC estimate can be found by generating N samples drawn from $q(\mathbf{x})$ and then the weighted sum can be formed:

$$I_N = \frac{1}{N} \Sigma_{i=1}^{N} \mathbf{f}(\mathbf{x}^i) \hat{w}(\mathbf{x}^i) \tag{3.27}$$

where $\hat{w}(\mathbf{x}^i) = \frac{\pi(\mathbf{x}^i)}{q(\mathbf{x}^i)}$ from the weights. Generally the normalizing factor of the desired density is not known so the normalization of the weights needs be done.

Importance Sampling put in the context of Bayesian nonlinear filtering is known as Sequential Importance Sampling (SIS). This sequential Monte Carlo approach is known by many names including bootstrap filtering, condensation algorithm, particle filtering, interacting particle approximations, and more [56].

Importance sampling established that the Posterior density could be obtained via a discrete approximation:

$$p(\mathbf{X}_k|\mathbf{Z}_k) \approx \sum_{i=1}^{N_p} w_k^i \delta(\mathbf{X}_k - \mathbf{X}_k^i) \tag{3.28}$$

with weights chosen as described via:

$$w_k^i \propto \frac{p(\mathbf{X}_k|\mathbf{Z}_k)}{q(\mathbf{X}_k|\mathbf{Z}_k)} \tag{3.29}$$

Recursion is obtained via the following assumptions [7]. First, that the importance density can be decomposed as:

$$q(\mathbf{X}_k|\mathbf{Z}_k) = q(\mathbf{x}_k|\mathbf{X}_{k-1}\mathbf{Z}_k)q(\mathbf{X}_{k-1}|\mathbf{Z}_{k-1}) \tag{3.30}$$

This establishes that a new drawn sample from the importance density is pairing the prior samples with a new state. This, along with the last assumption that the stochastic process is a Markov Chain (which allows a sample $\mathbf{x}_k$ to only depend on the previous step $\mathbf{x}_{k-1}$), allows the weight update equation to be established as:

$$w_k^i = w_{k-1}^i \frac{p(\mathbf{z}_k|\mathbf{x}_k^i)p(\mathbf{x}_k^i|\mathbf{x}_{k-1}^i)}{q(\mathbf{x}_k^i|\mathbf{x}_{k-1}^i, \mathbf{z}_k)} \tag{3.31}$$

which in turn allows the Posterior density to be more simply approximated as:

$$p(\mathbf{x}_k|\mathbf{Z}_k) \approx \sum_{i=1}^{N_p} w_k^i \delta(\mathbf{x}_k - \mathbf{x}_k^i) \tag{3.32}$$

The numeric values of the weights and amount of samples determine the efficiency of the SIS algorithm. As shown, this algorithm utilizes recursion of the weights and draws samples each time step for each particle from the importance density.

It is an elegant and simple algorithm that is very powerful. However, every SIS filter suffers from degeneracy where all but one particle will have nonzero weights after a finite number of iterations. This is equivalent to saying the variance of the particles is guaranteed to increase over time, which is well documented and is in general unavoidable. Various means to measure degeneracy exist. One is shown below.

$$N_{eff} = \frac{1}{\sum_{i=1}^{N}(w_k^i)^2} \tag{3.33}$$

When the measure crosses below a user-stipulated threshold (N_{thr}), the next step of Particle Filtering commences - resampling.

Resampling mitigates the degeneracy issue by generating a new same-sized set (sampling with replacement) of particles with non-negligible weights. The new state space variables (support) are chosen in a manner that particles with low weight have a low chance of being chosen, and particles with a high weight are given a high chance. The weights are reset to be uniform ($\frac{1}{N}$). Many methodologies are available to do this, each with their own computational, accuracy, and speed considerations. They are described below in the next section as they apply to the PF variant designed.

The main components of the PF have been stipulated. SIS filtering, the calculation of the Effective Sample Size (if desired), and Resampling. The structure is simple and effective, but the main design component comes in the choice of the importance function, the number of Particles, and the Resampling method choice.

3.2.2 The constrained Unscented Particle Filter (cUPF)

The variant of the Particle Filter devised for this dissertation does not deviate from the main components of the SIS Filter with Resampling. However, many design considerations need to be established as the PF framework is extremely

general.

Choice of Importance Function

One of the main tenets of the PF is the use of the importance density as described in Eq. 3.30. It is pivotal for the PF convergence and efficiency that this importance density be as similar to the true Posterior density as possible. There are a host of well established candidates [56]:

1. The optimal importance density w.r.t. minimizing the variance of the importance weights has been derived in [17]. It involves the ability to sample from $p(\mathbf{x}_k|\mathbf{x}_{k-1}^i, \mathbf{z}_k)$ and to evaluate the integral yielding $p(\mathbf{z}_k|\mathbf{x}_{k-1})$. Neither of these quantities are readily available in a computationally feasible manner.

2. The transitional prior $p(\mathbf{x}_k|\mathbf{x}_{k-1})$. However, this was found to be a poor choice. Note that the state space spanned by $\mathbf{x}$ at time point $k = 0$ is the entirety of the search space for the satellite to look for the RF emitter. This is a much broader and expansive (uninformed) likelihood than the likelihood $p(\mathbf{z}_k|\mathbf{x}_{k-1})$. This causes a severe degeneration in the particles, yielding only a few particles with non-negligible weights within a few iterations.

3. There are a host of variants that "inform" the transitional prior to providing samples with a higher likelihood (larger weight). A common method is the Auxiliary Particle Filter which utilizes the current measurement to augment the transitional state prior density. It was found in this application that the state likelihood was simply too broad, and the usage of measurements to augment it introduced instability and slow convergence. The SSG scenario inherently depends on the measurement equation to constraint the state

space much more than the state equations do. In the case of heavily biased measurements as in this application scenario, the use of a measurement that will be prone to frequent, non-Gaussian errors often incorrectly informs likelihoods.

The constrained Unscented Kalman Filter developed in the previous section is far and beyond the best choice for the importance distribution. It doubles as both the best possible guess of the support of the importance density and as a convergent, well-behaved estimation process. This is essentially the same as placing N_p particles, or N_p cUKF filters to estimate the emitter location. Each cUKF filter is initialized different, and the iteration process of the PF can be visualized as particles randomly placed upon the Earth and incrementally moving across the surface of the earth in search of the potential emitter location that provides the best state estimate. As a result, this creates a filter that is much more resilient filter to initialization error and greatly expands the search area space. As will be shown, because resampling is done at each step, the importance weights are not recursively passed on to be used in the computation for the next time iteration.

Choice of Resampling Method

The resampling method used is referred to as *Systematic Sampling* and is chosen for accuracy and computational efficiency. The computational requirements are discussed more in the next section. The resampling method is simple to implement and has a computational complexity of $O(N)$. In general, systematic sampling draws samples from a larger set, selected according to a random starting point within a fixed, periodic interval. This method has wide applications across many fields. But as it is applied to nonlinear filtering, the implementation

was taken from [37] and is restated here:

Systematic Resampling

1. Initialize the cumulative sum of weights to be $c_1 = w_k^1$
2. FOR $i = 2 : N$ set $c_i = c_{i-1} + w_k^i$
3. Set $u_1 \sim U[0, N^{-1}]$
4. FOR $j = 1 : N$
   - $u_j = u_1 + N^{-1}(j-1)$
   - WHILE $u_j < c_i$: $\quad i = i + 1$
   - Assign sample: $\mathbf{x}_k^{j*} = \mathbf{x}_k^i$
   - Assign weight: $w_k^j = N^{-1}$

Additional Components

A very accurate and efficient SSG solution has been formulated through the use of a SIS Filter, utilizing a constrained UKF as the importance density and resampling to mitigate sample degeneracy. However, resampling when the state equation has relatively little noise in comparison to the measurement noise creates an unwanted phenomena called *sample impoverishment* [7]. This describes a situation when there is a loss of diversity within the particles since the resampling algorithm is preset to pick samples with high weights repetitively (therefore when only a few samples have nonzero weights, sample diversity is quickly lost). This generally leads to extremely quick convergence to a single particle and is essentially equivalent to running a single cUKF.

Given the emitter is assumed stationary, there is little chance that the noise within the process equations will be relatively significant. In scenarios where the emitter is approximately stationary (with respect to the satellite) the process noise can reach the same magnitude as the measurement noise - but this cannot be expected in a generic SSG system design.

To combat this, jitter can be added within the algorithm that prevents a terminal loss of particle diversity. One of the more elegant matters of the SSG problem formulation is the highly intuitive geometry. The constrained state space is the surface of the earth. The cUKF generates sigma points that assume a mean that is the emitter location estimate and gives a state covariance which is the area of uncertainty about the estimate. The proposed PF runs N_p cUKFs, each returning a state estimate and covariance. At each time step, once all N_p emitter estimates ($\mathbf{x}_k^n$) are returned, the centroid is computed, $\mathbf{x}_k^\gamma$. If the distance of all the estimates (corresponding to distance upon the Earth) is less than 500 meters, then all Particles are drawn once more from a Gaussian distribution centered at $\mathbf{x}_k^\gamma$) and a covariance of the 500 meters squared in X,Y, and Z. This technique can be seen as an ad-hoc methodology of a *regularized particle filter* (RBF) and attempts to accomplish the same purpose as the Markov Chain Monte Carlo (MCMC) move step. Each are legitimate contemporaries but were deemed too computationally intense for the amount of times particle diversity is very low (this is rare).

Scenarios needing this jitter technique are rarely encountered in practice. However the jitter technique does add stability if the PF reaches a convergent point with low particle diversity. This situation can occur when the estimate is very accurate or entirely off, and is a symptom of purely perceived algorithmic convergence. Adversely, it also prevents asymptotic approximation of the Posterior density, although geolocation estimates of less than 500 meters for the purposes

of this SSG scenario is hardly expected.

At this point the entirety of the crafted geolocation algorithm, the constrained Unscented Particle Filter can be fully outlined:

Constrained Unscented Particle Filter

Assume there are $i = \begin{bmatrix} 1 & \dots & N_p \end{bmatrix}$ particles and N_t sampled time points. The algorithm is initialized using the state covariance effectively covering the search area. For each sampled time point:

1. Run the cUKF as discussed in the previous section
2. Draw $\mathbf{x}_k^i \sim N(\hat{\mathbf{x}}_k | \hat{\mathbf{P}}^i_{x_k}) = q(\mathbf{x}_k^i | \mathbf{x}_{k-1}^i, \mathbf{z}_k)$
3. Assign each $\mathbf{x}_k^i$ a corresponding weight, $w_k^{n_p}$

$$w_k^i = \frac{p(\mathbf{z}_k|\mathbf{x}_k^i)p(\mathbf{x}_k^i|\mathbf{x}_{k-1}^i)}{q(\mathbf{x}_k^i|\mathbf{x}_{k-1}^i, \mathbf{z}_k)} \tag{3.34}$$

4. Normalize Weights by dividing each w_k^i by $W_n = \sum_{i=1}^{N_p} w_k^i$
5. Resample at each processed time step using Algorithm 2 in [7]
6. Compute the centroid $\mathbf{x}_k^\gamma = \sum_{i=1}^{N_p} \frac{1}{N_p} \hat{\mathbf{x}}_k^i$. If $|\mathbf{x}_k^\gamma - \hat{\mathbf{x}}_k^i| < 500$ for each i then redraw $\hat{\mathbf{x}}_k^i \sim N(\mathbf{x}_k^\gamma, 500^2\mathbf{I})$.
7. Assign Covariance for each Particle $= \mathbf{P}^i_{x_k} = \hat{\mathbf{P}}^i_{x_k}$ and compute a weighted estimate of the mean for the current best estimate at time k as $\hat{\mathbf{x}}_k = \sum_{i=1}^{N_p} w_k^i \mathbf{x}_k^i$.

3.3 Computational Complexity

3.3.1 Overview of On-Board Processing Capabilities

The ability to process these geolocation algorithms in real-time is a major aspect of its novelty. This is a distinct challenge as computation abilities of spacecraft have generally lagged behind terrestrial computers by several generations. In general the cost to manufacture silicon computer parts tolerant to space radiation forces a tradeoff between computationally high performance and radiation tolerance [4]. Before the SmallSat Revolution, most satellite missions chose high radiation tolerance to be risk-adverse. An excellent list of SmallSat Processors and Single-Board Computers that have flown to space or are on existing missions is in [24].

However, with the onset of the SmallSat Revolution, the risk equation has changed. Satellite designers are more open towards utilizing higher computational powers with lower radiation tolerance. Despite this trend, the onboard computational powers are still dominated by microcontrollers and general purpose central processing units (CPUs).

Recently, research and applications involving reconfigurable computing and hybrid computing have allowed much more power to be harnessed [24]. Reconfigurable computing focuses on devices with adaptive designs that can be programmed to create different architectures and circuits. The most well-known of these are Field Programmable Gate Arrays (FPGAs) which also bring to the table energy efficiency. They are used now to interface multiple high-bandwidth sensors to a system ("interface glue logic"), synthetic aperture radar (SAR), hyperspectral imaging (HSI), image processing, image compression, and more. Hybrid computing combines dissimilar devices to gain their respective strengths when used as a

whole. An example of this is the use of a general-purpose CPU combined with an FPGA on the same board or a combination of rad-hard devices with higher grade commercial devices. The most popular of these are the System-on-Chip (SoC) devices which combine several designed blocks into a single chip. These are then embedded into processors, memory blocks, interface blocks, and more [24].

A specific example of a data processing system that could comfortably host the provided geolocation algorithms is the SpaceCub v2.0 [53]. This was designed by the NASA Goddard Space Flight Center and has flown on several missions. It is a hybrid processor that houses two Virtex-5 FPGAs linked by a high speed interconnect. The hybrid processor is a Xilinx Virtex-5 which has two PowerPC 440 RISC hardcore CPU blocks. Several other similar processing systems exist and are escribed in [24].

3.3.2 Computational Cost of the Proposed Algorithms

Measures of computational costs are difficult as there is no standard metric that yields equivalent comparisons across different systems. *Computational Complexity* is traditionally described in the asymptotic sense using the big O notation. It is a generic, usually worst case scenario that describes how an input number of items, n, affects and is expressed in terms of the system output $O(n)$. For instance, integer multiplication is at worst $O(n^2)$, suggesting that there is a constant c_m such that the multiplication of at most n integers will be computed equal to or less than $c_m n^2$ time.

This, however, does not give a tangible feel for an algorithmic implementation. A more palpable measure is often a numerical quantity of *flops*. Flops is actually an acronym, FLOPS, standing for "Floating Point Operations." It is a standard for gauging algorithms and computations that require the high precision offered

by floating point numbers. The number of flops needed to execute an algorithm is highly informative. In a commercial processor setting, "FLOPs" is generally understood to mean "Floating Point Operations per Second" to give a tangible feel for how a particular processing unit can handle floating point tasks. Each of these interpretations are more informative than another common measure - instructions per second. The algorithms given in this paper are dominated by floating point operations so the use of flops is reasonable and therefore utilized.

What constitutes a floating point operation differs from processor to processor, so care must be taken to not false advertise. For instance, in the modern CPU Intel x86 trigonometric computations are included as single line instructions. This would quantify it as a flop, the same as a floating point multiplication. However, if one were to perform a benchmark to measure the time required to compute a trigonometric calculation versus a floating point multiplication - it would not be uncommon to see the trigonometric computation time be upwards of 20 times lengthier (taking many cycles to compute). Yet, they are both considered a flop. The same story goes for square root operations. Because of this, the two algorithms provided in this dissertation - the cUKF and the cUPF - are stipulated below in number of flops (addition, subtraction, multiplication, division, exponentiation), trigonometric computations, and square root computations.

cUKF

Let M be the number of measurements, L the number of states, and N the number of sigma points. N is kept generic as the number of sigma points can vary (although here $N = 2L + 1$, $L = 3$, and $M = 2$). Table 3.2 outlines the computational burden at each step in the cUKF algorithm. The Cholesky Decomposition (serially implemented) was used for the sigma point computation

Table 3.2: cUKF Computational Cost Each kth Algorithmic Iteration

Algorithmic Step	**Flops**	$\sqrt{\cdot}$	**Trig**
σ-Pt Computation	$\frac{N(N+1)}{2} + \frac{N^3-N}{3}$	N	0
Constraint Projection	$78N$	N	$10N$
Time Update	$2N(L^2+L)+NL+L$	0	0
Constraint Projection	$78N$	N	$10N$
Measurement Update	$2M^2N+4MN+27LN+MLN$	$4N$	0
Fusion Equations	$M^3+3M^2-L+2M+4LM^2-LM$	M	0
Total	$\frac{1}{6}(2N^3+3N^2+946N+3)+5M^2+2M+M^3+$ $2NL^2+30NL+4MN+MLN+4M^2-LM$	$16N+M$	$20N$

in the State prediction and the LU decomposition [33] was used to invert the state-measurement covariance in the Measurement Update section.

cUPF

Notation is the same as the cUKF in the prior section: Let M be the number of measurements, L the number of states, and N the number of sigma points. For this application $M = 2$ and $K = 3$ but is kept generalized. Let $N^{\text{f}}_{\text{cUKF}}$ denote the total number of flops required by a single cUKF kth iteration. Likewise, let $N^{\text{s}}_{\text{cUKF}}$ and $N^{\text{t}}_{\text{cUKF}}$ denote the total number of square root operations and trig operations. The number of Particles is denoted as N_p and D represents the number of draws needed to characterize the uniform distribution (this will differ each time). Table 3.3 outlines the computational burden at each step in the cUPF algorithm.

The Cholesky Decomposition was used for the sigma point computation (serially implemented) in the State prediction and the LU decomposition was used to invert the state-measurement covariance in the Measurement Update section. For the generation of a Gaussian sample, the method of CDF ($\Phi(x)$, Cumulative Distribution Function) inversion is utilized. This takes a random number from a unitary uniform distribution $U[0,1]$ and generates a Gaussian random variable, x, via $\Phi^{-1}(x)$. The closed form for the inversion of $\Phi(x)$ does not exist so a host

Table 3.3: cUPF Computational Cost Each kth Algorithmic Iteration

Algorithmic Step	**Flops**	$\sqrt{\cdot}$	**Trig**
N cUKFs	$N_p N^{\mathrm{f}}_{\mathrm{cUKF}}$	$N_p N^{\mathrm{s}}_{\mathrm{cUKF}}$	$N_p N^{\mathrm{t}}_{\mathrm{cUKF}}$
Redraw Particles	$4N_p$	N_p	N_p
Particle Weights	$2M^2N_p + 7N_pM + 2N_pL^2 + 29N_pL + 3N_p$	$2N_p$	0
Resample	$6N_p + DN_p - 2$	DN_p	DN_p
Estimate	KN_p	0	0
Total	$N_p(N^{\mathrm{f}}_{\mathrm{cUKF}} + 2M^2 + 2L^2 + 8M + 29L + 13 + D) - 2$	$N_p(N^{\mathrm{s}}_{\mathrm{cUKF}} + D + 3)$	$N_p(N^{\mathrm{t}}_{\mathrm{cUKF}} + D + 1)$

of approximations exist. The one used in this computational cost profile is the Box-Muller transform [47]. The acquisition of a psuedo-random seed is assumed to be taken from a physical process such as thermal or clock noise. These processes are known to be roughly uniform and can be used to generate a uniform distribution once scaled. The process needed to accomplish this varies broadly from processor to processor and is largely left out of the analysis. The drawing of a uniform number is considered a singular flop.

As will be shown in the Numerical Results Sections, in order to combat the cUPFs high computational requirements, time samples can be skipped. This luxury is afforded by the modeling capabilities of the cUPF framework.

Chapter 4

Theoretic Performance Bounds

4.1 Background Theory

Let $\mathbf{x}$ be an $(L \times 1)$ deterministic parameter vector and let $\mathbf{z}$ be an $(M \times 1)$ vector of measured data. As such, let $p(\mathbf{z}|\mathbf{x})$ be the conditional pdf of data $\mathbf{z}$ given the parameter set $\mathbf{x}$. Lastly, let $\hat{\mathbf{x}}(\mathbf{z})$ be an estimate of $\mathbf{x}$. The estimation mean square error matrix can now be formed:

$$\Sigma = \mathop{\mathbb{E}}_{p(\mathbf{z}|\mathbf{x})} \left\{ [\hat{\mathbf{x}}(\mathbf{z}) - \mathbf{x}][\hat{\mathbf{x}}(\mathbf{z}) - \mathbf{x}]^T \right\} \tag{4.1}$$

and related to the Fisher Information matrix (FIM) and Cramér-Rao Bound (CRB):

$$\Big[\Sigma\Big]_{ii} \geq \Big[\mathbf{J}^{-1}\Big]_{ii} = \mathbf{C} \tag{4.2}$$

where $\Big[\mathbf{A}\Big]_{ij}$ denotes the element in the ith row and the jth column of matrix $\mathbf{A}$. $\mathbf{C}$ is the Cramér-Rao Bound (CRB), which is defined as the inverse of the Fisher Information Matrix (FIM), denoted as $\mathbf{J}$. It gives a theoretical lower bound on

the covariance of any unbiased estimator. The FIM is defined as:

$$\mathbf{J} = - \underset{p(\mathbf{z}|\mathbf{x})}{\mathbb{E}} \left\{ \nabla_{\mathbf{x}}^{\mathbf{x}} \log p(\mathbf{z}|\mathbf{x}) \right\} \tag{4.3}$$

and ∇_{α}^{β} is the $(m \times n)$ Hessian matrix w.r.t. parameter vectors α of size $(m \times 1)$ and β of size $(n \times 1)$. This bound stands as long as the expectations and derivatives exist, and the limits of integration do not depend on the parameters to be estimated.

When the parameter vector is random with known statistics, Van Trees proposed a Bayesian CRB (BCRB), also known as the Posterior Cramér-Rao Bound (PCRB) [8]. Provided the derivatives and expectations exist, and the prior densities go to zero at the limits of the parameters being estimated, the Posterior FIM can be written as:

$$\mathbf{J}^{B} = - \underset{p(\mathbf{z},\mathbf{x})}{\mathbb{E}} \left\{ \nabla_{\mathbf{x}}^{\mathbf{x}} \log p(\mathbf{z}, \mathbf{x}) \right\} \tag{4.4}$$

where $p(\mathbf{z}, \mathbf{x})$ is the joint pdf of $\mathbf{z}$ and $\mathbf{x}$.

The recursive Posterior Cramér-Rao Bound (rPCRB) obtains its recursive properties through use of the PCRB framework and Markovian Chain attributes, as will be shown. The result is a bound well-suited to gauge the optimality of iterative nonlinear estimation algorithms. The following expressions in this are taken from the derivation in [66], and are restated here for convenience. Consider the classic (non-constrained) nonlinear filtering problem:

$$\mathbf{x}_{k+1} = \mathbf{f}_k(\mathbf{x}_k, \mathbf{w}_k)$$
$$\mathbf{z}_k = \mathbf{h}_k(\mathbf{x}_k, \mathbf{v}_k)$$

where $\mathbf{x}_k$ is the system state $(L \times 1)$ vector at time k, $\{\mathbf{z}_k\}$ is the measurement

process $(M \times 1)$ vector, $\mathbf{f}_k$ and $\mathbf{h}_k$ are nonlinear functions, and $\{\mathbf{w}_k\}$ and $\{\mathbf{k}_n\}$ are independent white noise processes of the state and measurement equations, with zero mean and covariances $\mathbf{Q}_k$ and $\mathbf{V}_k$, respectively.

Together with a known pdf function of the initial state $\mathbf{x}_0$, $p(\mathbf{x}_0)$, the joint probability distribution of $\mathbf{X}_k = [\mathbf{x}_0^T, \ldots, \mathbf{x}_k^T]^T$ and $\mathbf{Z}_k = [\mathbf{z}_0^T, \ldots, \mathbf{z}_k^T]^T$ can be formed:

$$p(\mathbf{X}_k, \mathbf{Z}_k) = p(\mathbf{x}_0) \prod_{i=1}^{k} p(\mathbf{z}_i|\mathbf{x}_i) \prod_{j=1}^{k} p(\mathbf{x}_j|\mathbf{x}_{j-1}) \tag{4.5}$$

Using this joint distribution and the Posterior Cramér-Rao Bound equation (Eq. 4.4), an $(LN \times LN)$ information matrix can be formed, $\mathbf{J}$. The inversion of this large matrix gives the PCRB. However, the only portion of this matrix that is desired is the lower $(k \times k)$ submatrix representing the PCRB of only the latest state estimates, denoted as $\left(\mathbf{J}_k^B\right)^{-1}$, as can be seen by decomposing $\mathbf{X}_k = \left[\mathbf{X}_{k-1}^T \mathbf{x}_k^T\right]^T$.

By assuming the iterative process is a Markovian Chain and the use of the Woodbury matrix identity, Tichavsky et al showed that this submatrix can be efficiently computed in a recursive manner [66]. The sequence $\mathbf{J}_k^B$ of posterior information submatrices for the estimation of state vectors $\mathbf{x}_k$ can be computed as:

$$\mathbf{J}_{k+1}^B = \mathbf{D}_k^{22} - \mathbf{D}_k^{21}(\mathbf{J}_k^B + \mathbf{D}_k^{11})^{-1}\mathbf{D}_k^{12} \tag{4.6}$$

where

$$\mathbf{D}_k^{11} = \mathop{\mathbb{E}}_{p(\mathbf{x}_k)} \left\{ -\nabla_{\mathbf{x}_k}^{\mathbf{x}_k} \log p(\mathbf{x}_{k+1}|\mathbf{x}_k) \right\} \tag{4.7}$$

$$\mathbf{D}_k^{12} = \mathop{\mathbb{E}}_{p(\mathbf{x}_k)} \left\{ -\nabla_{\mathbf{x}_k}^{\mathbf{x}_{k+1}} \log p(\mathbf{x}_{k+1}|\mathbf{x}_k) \right\} \tag{4.8}$$

$$\mathbf{D}_k^{21} = \left(\mathbf{D}_k^{12}\right)^T \tag{4.9}$$

$$\mathbf{D}_k^{22} = \mathop{\mathbb{E}}_{p(\mathbf{z}_k|\mathbf{x}_k)} \left\{ \mathbf{J}_{k+1} \right\} + \mathop{\mathbb{E}}_{p(\mathbf{x}_k)} \left\{ -\nabla_{\mathbf{x}_{k+1}}^{\mathbf{x}_{k+1}} \log p(\mathbf{x}_{k+1}|\mathbf{x}_k) \right\} \tag{4.10}$$

and $\mathbf{J}_k$ is the standard FIM matrix:

$$\mathbf{J}_{k+1} = \mathop{\mathbb{E}}_{p(\mathbf{z}_{k+1}|\mathbf{x}_{k+1})} \left\{ -\nabla_{\mathbf{x}_{k+1}}^{\mathbf{x}_{k+1}} \log p(\mathbf{z}_{k+1}|\mathbf{x}_{k+1}) \right\} \tag{4.11}$$

Note that this recursion is initialized with:

$$\mathbf{J}_0 = \mathop{\mathbb{E}}_{p(\mathbf{x}_0)} \left\{ -\nabla_{\mathbf{x}_0}^{\mathbf{x}_0} \log p(\mathbf{x}_0) \right\} \tag{4.12}$$

The following outlines the effect of adding a constraint to the estimation problem. The traditional CRB under parametric constraints has been derived by several methods. It was first proposed by [25] and later in a simplified manner by [49]. It was then expanded for the singular case by [65]. The theoretical foundation is outlined here.

Now assume the $(L \times 1)$ parameter vector $\mathbf{x}$ is subjected to a set of continuously differentiable constraints as in Eq. 2.18:

$$C = \{\mathbf{x}|\mathbf{g}(\mathbf{x}) = \mathbf{0}\} \tag{4.13}$$

where it is assumed the set is nonempty. The $(G \times L)$ gradient matrix of the

constraints is:

$$\mathbf{G}(\mathbf{x}) = \frac{\partial}{\partial \mathbf{x}} \mathbf{g}(\mathbf{x}) \tag{4.14}$$

Here, it is assumed that $\mathbf{G}(\mathbf{x})$ is of full row rank for any $\mathbf{x}$ that satisfies the constraint Eq. 4.13 (although the case where it is singular is again covered in [65]). This means there exists a matrix $\mathbf{U} \in \mathbb{R}^{L \times (L-G)}$ whose columns forms an orthonormal basis for the nullspace of $\mathbf{G}(\mathbf{x})$.

Recalling the mean squared error matrix defined in Eq. 4.1, Σ, the constrained CRB can be defined as:

$$\Sigma \geq \mathbf{U}(\mathbf{U}^T \mathbf{J} \mathbf{U})^{-1} \mathbf{U}^T \tag{4.15}$$

The application of the constraint to the rPCRB was formalized by [59]. Recall the nonlinear filtering equations with an equality constraint in Eqs. 2.17-2.19. Then, as shown in [59] the error covariance of any unbiased state estimate $\mathbf{x}_k$ at time k is:

$$\mathbf{\Sigma}_k \geq \mathbf{U}_k \mathbf{J}_k^{-1} \mathbf{U}_k \tag{4.16}$$

where $\mathbf{U}_k$ denotes the matrix whose columns forms an orthnormal basis for the nullspace of $\mathbf{G}_k(\mathbf{x}_k)$. This is stating that the matrix $\mathbf{\Sigma}_k$ is positive semi-definite. It then follows through recursion that $\mathbf{J}_k$ (derived in the same fashion as [66]) can be expressed as:

$$\begin{aligned} \mathbf{J}_{k+1} = \mathbf{U}_{k+1} \Big(\mathbf{D}_k^{22} - \mathbf{D}_k^{21} \mathbf{U}_k (\mathbf{U}_k^T \mathbf{D}_k^{11} \mathbf{U}_k + \mathbf{J}_k)^{-1} \dots \\ \dots \times \mathbf{U}_k^T \mathbf{D}_k^{12} \Big) \mathbf{U}_{k+1} \end{aligned} \tag{4.17}$$

4.2 The recursive constrained Posterior Cramér-Rao Bound (rcPCRB)

This section provides a recursive constrained Posterior Cramér-Rao Bound (rcPCRB) that provides a measure of mean squared error optimality for the cUKF and cUPF. The rcPCRB is uniquely suited in that it is a bound meant to gauge iterative nonlinear algorithms that incorporates information measures from both the state and measurement equations and easily adapts to on-off signal characteristics. There are currently no existing bounds for the SSG scenario meant for nonlinear iterative estimation algorithms, and this section applies the theory laid out in Section 4.1 to the nonlinear filtering setup in Eq. 2.24.

Note, this bound does not apply to the situation where there are ephemeris or oscillator errors present. These errors propagate a different characterization of noise than is assumed in this bound (Gaussian).

Recall the desired rcPCRB bound defined in Eq. 4.17 as:

$$\begin{aligned}\mathbf{J}_{k+1} = \mathbf{U}_{k+1}\Big(\mathbf{D}_k^{22} - \mathbf{D}_k^{21}\mathbf{U}_k(\mathbf{U}_k^T\mathbf{D}_k^{11}\mathbf{U}_k + \mathbf{J}_k)^{-1}\dots \\ \dots \times \mathbf{U}_k^T\mathbf{D}_k^{12}\Big)\mathbf{U}_{k+1}^T\end{aligned}$$

Now, given Eq. 2.20 and Eq. 2.24, we can define the recursive Bayesian CRB matrices as:

$$\mathbf{D}_k^{11} = \mathbf{Q}_k^{-1} \tag{4.18}$$

$$\mathbf{D}_k^{12} = -\mathbf{Q}_k^{-1} \tag{4.19}$$

$$\mathbf{D}_k^{21} = \left(\mathbf{D}_k^{12}\right)^T \tag{4.20}$$

$$\mathbf{D}_k^{22} = \underset{p(\mathbf{z}_k|\mathbf{x}_k)}{\mathbb{E}}\left\{\mathbf{J}_{k+1}\right\} + \mathbf{Q}_k^{-1} \tag{4.21}$$

The expectation of the nonlinear function of $\mathbf{x}_n$ in $\mathbf{D}_n^{22}$ cannot be evaluated analytically. One can either take the expectation of a Taylor Series approximation of the nonlinear function or a Monte Carlo integration can be done. The latter is the technique used here and defined below:

$$\mathop{\mathbb{E}}_{p(\mathbf{x}_k)}[\mathbf{J}_k] = \int \mathbf{J}_k p(\mathbf{x}_n) \partial \mathbf{x}_k \tag{4.22}$$

$$\approx \frac{1}{N} \sum_{i=1}^{N} \mathbf{J}_k(\tilde{\mathbf{x}}_k^i) \tag{4.23}$$

where $\tilde{\mathbf{x}}_k^i$ are drawn from the Gaussian distribution of $\mathbf{x}_k$. $\mathbf{J}_k$ is the traditional FIM, which can be expressed as shown below:

$$\mathbf{J}_k = \mathbb{E}\left\{ \left(\frac{\partial}{\partial \mathbf{x}_k} \ln p(\mathbf{z}_k|\mathbf{x}_k) \right)^T \left(\frac{\partial}{\partial \mathbf{x}_k} \ln p(\mathbf{z}_k|\mathbf{x}_k) \right) \right\} \tag{4.24}$$

$$= \left(\frac{\partial}{\partial \mathbf{x}_k} \mathbf{h}_k \right)^T \mathbf{V}_k^{-1} \left(\frac{\partial}{\partial \mathbf{x}_k} \mathbf{h}_k \right) \tag{4.25}$$

and the partial derivatives of Eq. 2.24:

$$\frac{\partial \mathbf{z}_k}{\partial \mathbf{x}_k^{(i)}} = \begin{bmatrix} \frac{\partial}{\partial x_k^{(i)}} h_k^{(1)}(\mathbf{x}_k) \\ \frac{\partial}{\partial x_k^{(i)}} h_k^{(2)}(\mathbf{x}_k) \end{bmatrix} \tag{4.26}$$

where (as is derived in Appendix 8.3):

$$\frac{\partial}{\partial x_k^{(i)}} z_k^{(1)}(\mathbf{x}_k) = \left(\frac{1}{\lambda} \right) \left(\frac{-v_{s(k)}^{(i)} |\mathbf{p}_{s(k)} - \mathbf{x}_k| - (\mathbf{v}_{s(k)}^T (\mathbf{p}_{s(k)} - \mathbf{x}_k)) \frac{p_{e(k)}^{(i)} - p_{s(k)}^{(i)}}{|\mathbf{p}_{s(k)} - \mathbf{x}_k|}}{|\mathbf{p}_{s(k)} - \mathbf{x}_k|^2} \right) \tag{4.27}$$

and

$$\frac{\partial}{\partial x_k^{(i)}} z_k^{(2)}(\mathbf{x}_k) = \frac{\partial}{\partial x_k^{(i)}} A(\mathbf{x}_k) + \frac{\partial}{\partial x_k^{(i)}} B(\mathbf{x}_k) + \frac{\partial}{\partial x_k^{(i)}} C(\mathbf{x}_k) \tag{4.28}$$

where

$$\frac{\partial}{\partial x_k^{(i)}} A(\mathbf{x}_k) = \left(\frac{-1}{\lambda}\right)\left(\frac{-a_{s(k)}^{(i)}|\mathbf{p}_{s(k)} - \mathbf{x}_k| - (\mathbf{a}_{s(k)}^T(\mathbf{p}_{s(k)} - \mathbf{x}_k))\frac{p_{e(k)}^{(i)} - p_{s(k)}^{(i)}}{|\mathbf{p}_{s(k)} - \mathbf{x}_k|}}{|\mathbf{p}_{s(k)} - \mathbf{x}_k|^2}\right) \tag{4.29}$$

$$\frac{\partial}{\partial x_k^{(i)}} B(\mathbf{x}_k) = \left(\frac{1}{\lambda}\right)\left(\frac{|\mathbf{v}_k|^2(p_{e(k)}^{(i)} - p_{s(k)}^{(i)})}{|\mathbf{p}_{s(k)} - \mathbf{x}_k|^3}\right) \tag{4.30}$$

$$\begin{aligned}\frac{\partial}{\partial x_k^{(i)}} C(\mathbf{x}_k) = \left(\frac{-1}{\lambda}\right)&\left(\frac{1}{((\mathbf{p}_{s(k)} - \mathbf{x}_k)^T(\mathbf{p}_{s(k)} - \mathbf{x}_k))^3}\right) \times \dots \\ &+ \Bigg(- 2\mathbf{v}_{s(k)}(\mathbf{v}_{s(k)}^T(\mathbf{p}_{s(k)} - \mathbf{x}_k) \cdot \Big((\mathbf{p}_{s(k)} - \mathbf{x}_k)^T(\mathbf{p}_{s(k)} - \mathbf{x}_k)\Big)^{\frac{3}{2}} + \dots \\ &\quad 3(p_{s(k)}^{(i)} - x_k^{(i)})|\mathbf{p}_{s(k)} - \mathbf{x}_k|(\mathbf{v}_{s(k)}^T(\mathbf{p}_{s(k)} - \mathbf{x}_k))^2\Bigg)\end{aligned} \tag{4.31}$$

noting again that $\mathbf{x}_k^{(i)}$ denotes the ith element of the vector $\mathbf{x}$ at the kth time step and $\mathbf{p}_{s(k)}^{(i)}$ denotes the ith element of the position vector of the satellite at the kth time step.

Recall the constraint in Eq. 2.21. This constraint allows the construction of the $L \times (L - G)$ matrix $\mathbf{U}_k$ (as shown in Eq. 4.16) where $L = 3$ is the number of parameters of interest and $G = 1$ is the number of constraints. The gradient matrix can then be defined in this case as:

$$\begin{aligned}\mathbf{G}(\mathbf{x}_k) &= \frac{\partial}{\partial \mathbf{x}_k}\mathbf{g}_k(\mathbf{x}_k) \\ &= \begin{bmatrix} \frac{2\mathbf{x}_k^{(1)}}{R_{eq}^2} & \frac{2\mathbf{x}_k^{(2)}}{R_{eq}^2} & \frac{2\mathbf{x}_k^{(3)}}{R_p^2} \end{bmatrix}\end{aligned} \tag{4.32}$$

We want a matrix $\mathbf{U}_k$ that is the orthonormal nullspace of $\mathbf{G}(\mathbf{x}_k)$. The constraint space as dictated by Eq. 2.16 is an ellipsoid, and the vector described by Eq. 4.32

is the normal vector at the point $\mathbf{x}_k$. Therefore, the tangent plane of the earth ellipsoid at the emitter location provides the basis of $\mathbf{U}_k$. The tangent plane at the point $\mathbf{x}_k$ can be expressed as:

$$0 = \frac{\mathbf{x}_k^{(1)}}{R_{eq}^2}\left(x - \mathbf{x}_k^{(1)}\right) + \frac{\mathbf{x}_k^{(2)}}{R_{eq}^2}\left(y - \mathbf{x}_k^{(2)}\right) + \frac{\mathbf{x}_k^{(3)}}{R_p^2}\left(z - \mathbf{x}_k^{(3)}\right) \tag{4.33}$$

where two vectors spanning this space at point $\mathbf{x}_k$ can easily be found and made orthonormal. The rcPCRB can now be computed for any SSG scenario where the error distribution is approximately Gaussian.

Chapter 5

Numerical Results: Simulated

Using both the cUKF geolocation algorithm and the rcPCRB performance bounds, an in-depth analysis of the accuracy capabilities of SSG is provided with variations in measurement noise, center frequency, slant angle, and initialization error - lending valuable information for various mission types. A contemporary approach using an cEKF (derived in Chapter 3) approach with the same earth-bound constraint as the cUKF is provided for algorithmic comparison. The proposed cUKF algorithm shows a close match with the rcPCRB theoretic performance bounds (derived in Chapter 4), converging to single-kilometer geolocation estimates in only a few seconds of acquisition time with demonstrated resiliency to measurement and initialization error - vastly outperforming the cEKF by over three orders of magnitude in every scenario.

The truth values for the synthesized data follow the derivations in Chapter 2 and are corrupted by Additive White Gaussian Noise (AWGN). The governing physics for the Earth and satellite movement are generated using the realistic simulation environment created from scratch, described in Section 2.3.5. For the processing of the simulated IQ data, the measurement equation (Eq. 2.24) estimates are produced as one would do in real-time by using a cyclostationary-

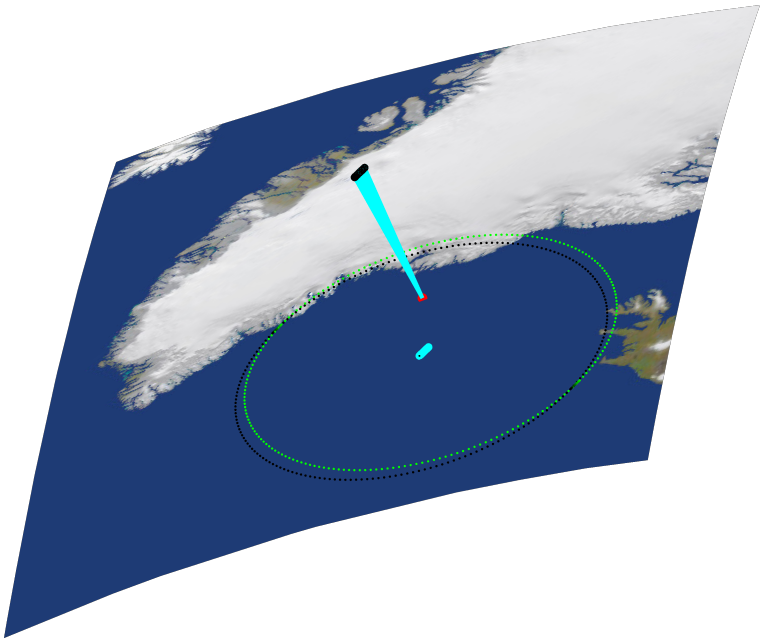

Figure 5.1: Depiction of scenario used for simulated numerical results (unless otherwise noted). The red dot is the emitter while the satellite moves overhead in black. The sub-satellite path and range vectors are in cyan while the antenna footprints are also shown at time zero (black dots) and five seconds later (light green dots).

based method [23] for $\mathbf{z}_k(1)$ (Doppler) and $\mathbf{z}_k(2)$ (Doppler Rate)is estimated using a Least Mean Squares curve fit to a numerical derivative.

All simulated results come from the following settings, shown in Fig. 5.1. An emitter sits at 65 deg Latitude, 35 deg Longitude, and an altitude of 0 kilometers above mean sea level (MSL). The transmitted signal has a center frequency of 120 MHz, emitting a 1200 Baud BPSK signal continuously for 5 seconds. The LEO satellite is flying circular orbit at 500 kilometers altitude at an 88 deg inclination. The satellite receives the transmitted signal, sampling at 4 times the highest expected Doppler frequency. All other parameters are stipulated as needed for the given scenario, or if changed from above, are succinctly noted to the reader.

Each point in the rcPCRB curves was obtained with 150 Monte Carlo trials to produce the numerically derived Expectation in Eq. 4.23. The state covariance

values are set to as close to zero as numerically possible within both the cUKF and rcPCRB to reflect the stationary emitter assumption. The measurement noise for the rcPCRB is set to the average of the measurement noise seen by the cUKF trials. The rcPCRB starting (initial position estimate) covariance matches the cUKF trials' average starting position.

For each of the coordinates (x, y, and z), 100 initial position guesses are drawn from a Gaussian distribution centered about the true position of the emitter with a standard deviation of 50 km (in x, y, and z) unless otherwise stated. These initial emitter position estimates are then projected onto the earth in the manner described in Chapter 3 and fed into the cUKF. The cEKF possesses the same covariances for state and measurement equations as the cUKF and is also fed the same random initialization guesses.

For scenarios exhibiting large ephemeris or oscillator errors, the cUPF is shown to effectively mitigate the non-Gaussianity in the Posterior error distributions. The cUPF is pitted against the cUKF and evaluated for the same scenario as with the cUKF (Fig. 5.1) over various magnitudes of ephemeris and oscillator errors. Again, the received Doppler is estimated using a cyclostationary technique [23] and the Doppler Rate is estimated using a Least Mean Squares curve fit to a numerical derivative technique. Measurements for Doppler and Doppler Rate are provided every 0.0573 seconds. The cUKF is run 150 times to produce the performance curves, and unless otherwise stipulated, the cUPF utilizes 20 particles and skips every 10 samples. Initial guesses are randomly drawn from a normal distribution centered around the true emitter position with a covariance spanning the surface of the earth nearly 400 kilometers in diameter. The cUKF settings in both the cUKF (as itself) and the cUPF (as the proposal distribution generator) are the same - the state standard deviation is set at 50 meters, the measurement

Table 5.1: Parameter Table for Fig. 5.2

C2N [dB]	$\sigma_z(1)$ [Hz]	$\sigma_z(2)$ [Hz/Sec]	h_s [km]	i [deg]	f_c [MHz]
20	2.22	0.16	500	88.5	120.6
30	0.8	0.06	500	88.5	120.6
40	0.15	0.0175	500	88.5	120.6

standard deviation is at 10 Hz for Doppler and 3 Hz for Doppler Rate. The tuning parameters are $\alpha = 1$, $\beta = 2$, and $\kappa = 0$.

5.1 Carrier-to-Noise Ratio

The following scenario depicts the effect of measurement noise on geolocation accuracy. A LEO satellite orbits the earth in a near polar orbit at 500 km altitude above MSL and an 88.5 deg inclination listening to a transmitted signal for 5 seconds. The emitted signal has a center frequency of 120 MHz and has a BPSK modulation with a baud rate of 1200. The sampling frequency is 4 times the expected highest Doppler frequency. The emitter sits at slant angle of 27 deg and a slant range of 574 km at $t_k = 0$ relative to the satellite.

The cEKF, cUKF and rcPCRB are evaluated at differing carrier-to-noise (C2N) ratios, which in turn affects the estimated measurements. This scenario is very typical of a search-and-rescue operation or the intercept of a communication signal. Table 5.1 lists the parameters used to generate the results shown in Fig. 5.2. For reference, the highest absolute measurement values are $z_k(1) = 664.99$ Hz and $z_k(2) = 36.67$ Hz/sec.

The cUKF closely matches rcPCRB with divergence beginning at 20 dB. Carrier-to-Noise ratios ranging from 20 dB to 40 dB are standard values, and given a stable enough estimation of the Doppler and Doppler rate, one can see from Fig. 5.2 that single-kilometer accuracy is obtained nearly immediately and

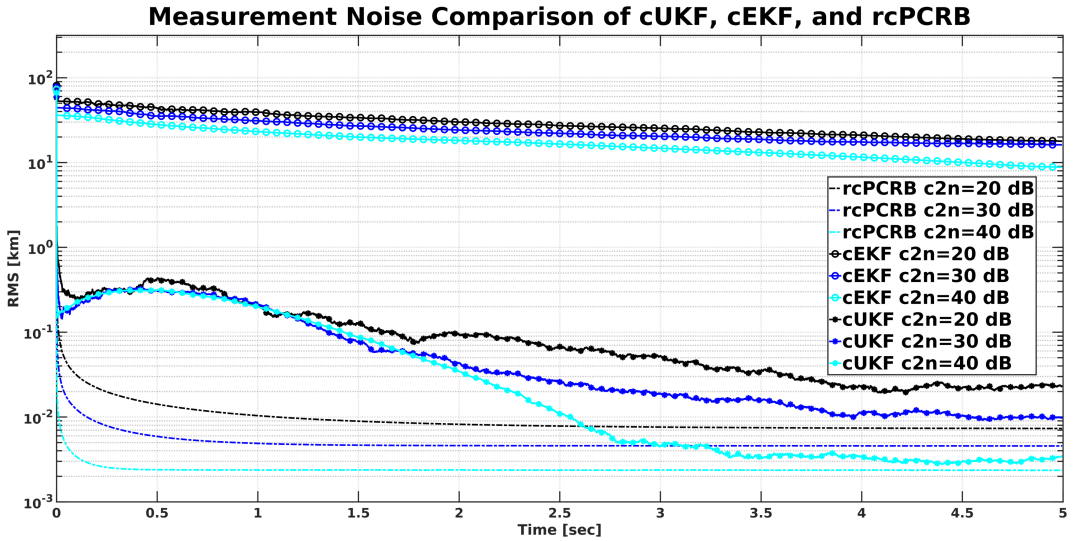

Figure 5.2: Depiction of the effect of differing Received Signal Powers upon the cUKF Algorithm

steady state reached at about 3 seconds. The cEKF is clearly multiple orders of magnitude larger than the cUKF performance. The cEKF is severely hampered by its inabilities to deal with large initialization errors and lower modeling capabilities.

5.2 Center Frequency

Center frequency is a complicated parameter to isolate due to the effect it has on the sampling rate requirements to accommodate Doppler shifts, the RF path loss, and the estimation technique applied. In general, an increase in center frequency brings about a trade space with bandwidth, noise floor, and sampling rate. One sanity check is the following: if the sampling rate is kept proportionally constant to the highest received frequency, and the measurement noise of the received Doppler and Doppler rate are kept with the same ratio - the performance across center frequencies will be the same.

Fig. 5.3, generated using Table 5.2, numerically demonstrates this conclusion.

Table 5.2: Parameter Table for Fig. 5.3

f_c [MHz]	$\sigma_z(1)$ [Hz]	$\sigma_z(2)$ [Hz/Sec]	**max** $z_k^{(1)}$ [Hz]	**max** $z_k^{(2)}$ [Hz/sec]
100	2.00	0.25	481.4	-32.3
500	10.11	1.20	2407.1	-161.55
1000	20.22	2.49	4814.2	-323.1

The fourth and fifth columns in Table 5.2 denote the highest received Doppler and Doppler Rate over the acquisition time to give the noise standard deviations in columns three and four meaning (as SNR will change based on a constant noise level and a changing value of Doppler and Doppler Rate). Using the same orbit settings as Section 5.1, it can be seen that the cEKF, cUKF, and the rcPCRB perform the same at each center frequency. Simulations show once more a good match between the cUKF and the rcPCRB, obtaining single-kilometer accuracies well within 1 second. The cEKF once again performs a little over 3 orders of magnitude worse than the cUKF, far from the optimal rcPCRB. This is strictly from the lack of modeling capabilities of the highly nonlinear equations governing the Doppler, Doppler Rate, and the constraint equation. the cEKF is notorious for falling short in highly nonlinear situations and this scenario is no different.

Center frequency scales the Doppler and Doppler Rate curve up or down proportionally. Yet, when the sampling rate and carrier-to-noise ratios are held proportionally the same across different center frequencies, changing the center frequency yields no new information for the geolocation algorithm to utilize. This is an important fact when designing an SSG system.

5.3 Transceiver Geometry

This section shows how much more information is obtained from larger absolute Doppler Rates that correspond to different signal acquisition positions during

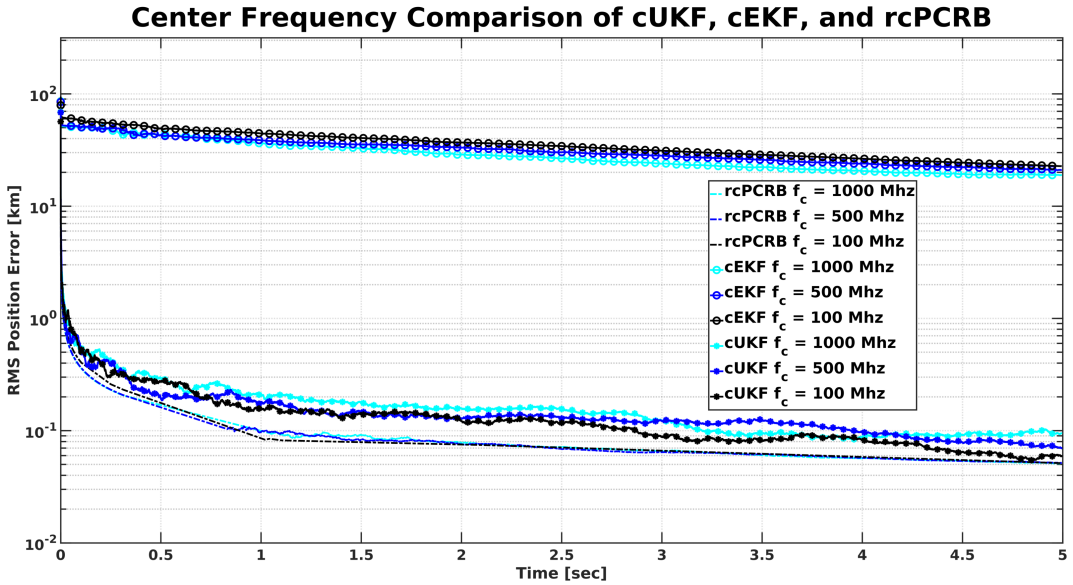

Figure 5.3: Depiction of the effect of different center frequencies when C2N ratios and sampling rates are held proportionally the same.

the orbit. The faster the Doppler is changing (corresponding to the satellite being closer and/or approaching the emitter), the more accurate the expected geolocation solution.

Table 5.3 shows the four signal sets. Each set corresponds to the satellite receiving the signal at differing distances from a direct flyover. Here the center frequency is held constant at 120 MHz. The 500 km orbit is set such that the Doppler zero-crossing ($f_D = 0$) occurs at a closest distance of 530 km away. The time at which the satellite observes $f_D = 0$ is denoted T_{D0} and the midpoint of the satellite's signal acquisition time is denoted T_{mid}.

As one would expect, shows that as the satellite moves closer and closer, the performance improves both in convergence time and accuracy. As the range vector decreases as the satellite moves closer, the signal power increases, causing the cUKF to track closer to the rcPCRB. Note there is a full magnitude of improvement when the satellite is directly over the emitter and when it receives the signal 30 seconds earlier (at a 30 degree slant angle and an additional 50 kilometers of

Table 5.3: Parameter Table for Fig. 5.4

Set	$\sigma_z(1)$ [Hz]	$\sigma_z(2)$ [Hz/Sec]	$T_{\text{mid}} - T_{D0}$ [Sec]	Slant Angle [deg]	Range [km]
1	1.65	0.49	0	15	535
2	3.31	1.00	−10	18	543
3	5.10	1.50	−20	23	561
4	6.04	1.82	−30	30	587

range distance). The cUKF outperforms the cEKF as in previous trials, but the cEKF still reflects the slant angle trends discussed.

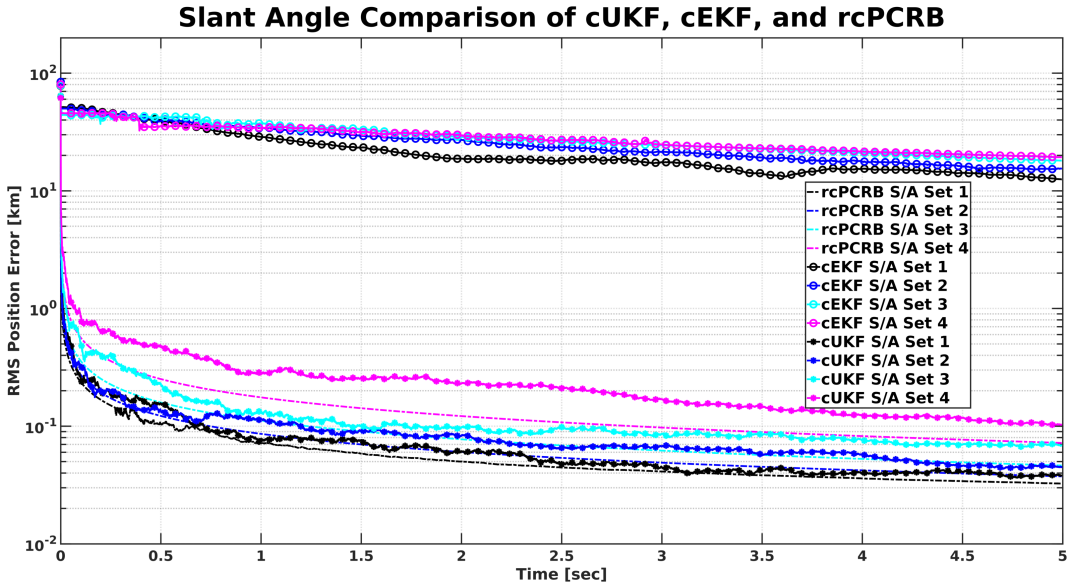

Figure 5.4: Depiction of the effect of different geolocation performances at differing slant angles. The different sets refer to the rows in Table 5.3

5.4 Initialization

A concern of any iterative algorithm is its resiliency to initialization errors. Prior to this section, initial guesses were chosen from a spherical zero mean Gaussian distribution with a standard deviation of 50 km. There, convergence is nearly guaranteed. Here, two satellite orbits are portrayed and a much larger search

space is considered. The two orbits differ mainly in that they are on opposite sides of the emitter. The center frequency is 1000 Mhz and the measurement noise $\sigma_z(1) = 20.00$ Hz and $\sigma_z(2) = 2.5$ Hz/Sec in each scenario.

In order to test the algorithm's sensitivity to initialization, the following is done. For each initial emitter location guess, five simulated runs of the satellite receiving the emitting signal for 2.5 seconds are performed. Each of these runs are put into the cUKF, generating a positional estimate. The average ending error of these five runs is given a proportional color as shown in Fig. 5.5 and Fig. 5.6. The x and y axes show the distances (in x and y) that the initial emitter positional estimate is from the true emitter position. The z error is imbued into the geolocation process, but is not visibly apparent in Fig. 5.5 and Fig. 5.6. However, the z value has an insignificant effect as each guess is projected upon the surface of the earth with a search space located near the North Pole. The directionality of the satellite is shown in the blue vector with light blue dot denoting the satellite position at the end of the acquisition period.

The geolocation algorithm showcases a large area of convergence, several hundreds of kilometers wide surrounding the true emitter position where geolocation accuracies are well below 5 km. These results exemplify the conditioning of the ill-conditioned solution space using the sigma point projection method and the second measurement equation. It can also be noted that there is a divergence in geolocation accuracy along the sub-satellite path of the satellite.

5.5 Ephemeris & Oscillator Errors

The following analysis shows the resiliency of the cUPF to both ephemeris and oscillator errors. The setup and parameterization of the cUPF are as stipulated at the beginning of this Chapter. All the figures are generated utilizing the values

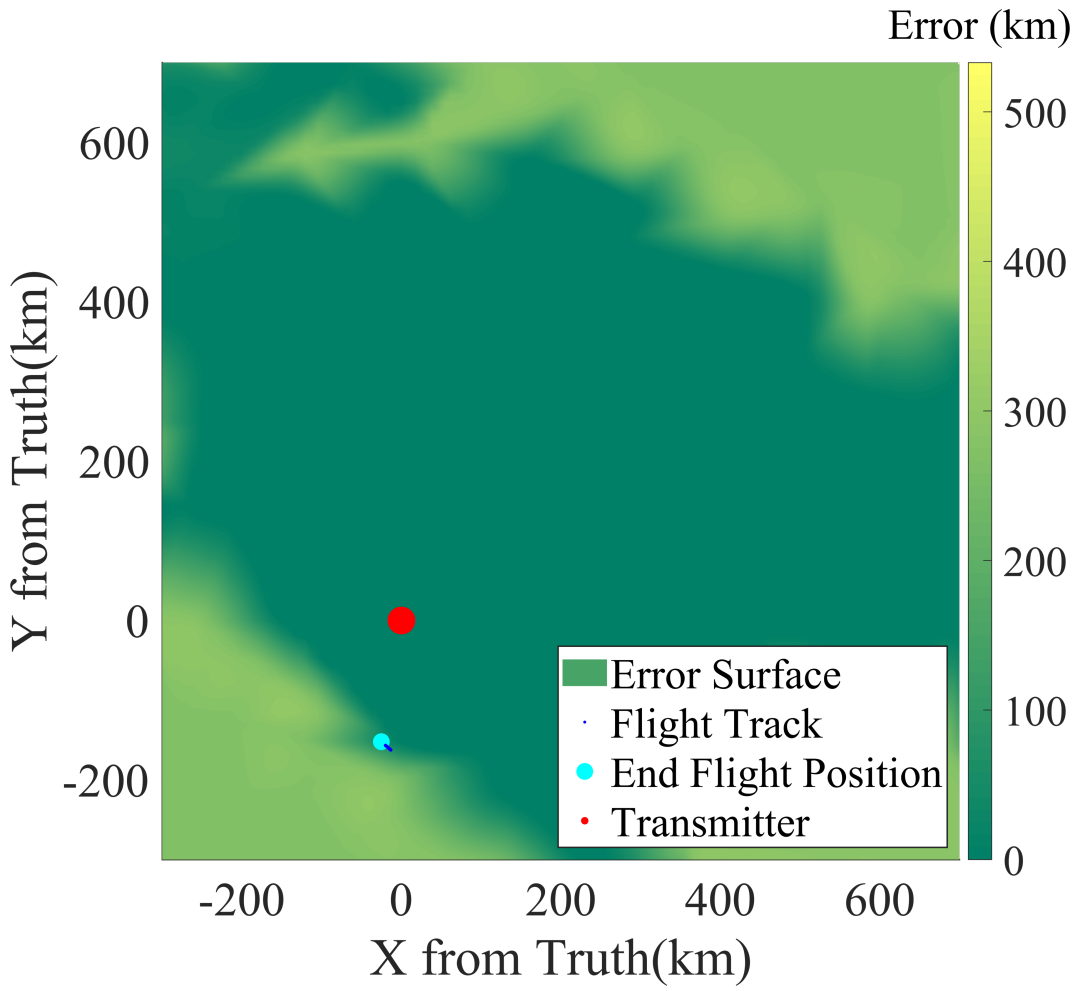

Figure 5.5: Depiction of the effect of different initial emitter position guesses for Flight Path 1.

in Tables 2.1 and 2.2. On each plot the cUKF performance is plotted in red. The weighted estimate of the cUPF is plotted in black. The cUPF's distribution of particles at each time point is plotted as well. Each color represents a particular particle. As the particle evolves over time, the color still remains the same. However, the size of the marker is proportional to the weight the sample has received and so will change over time as the cUPF is applied.

Figs. 5.7-5.9 all show the geolocation performance when the ephemeris errors are set as specified in Table 2.1. The improvement of the cUPF over the cUKF is

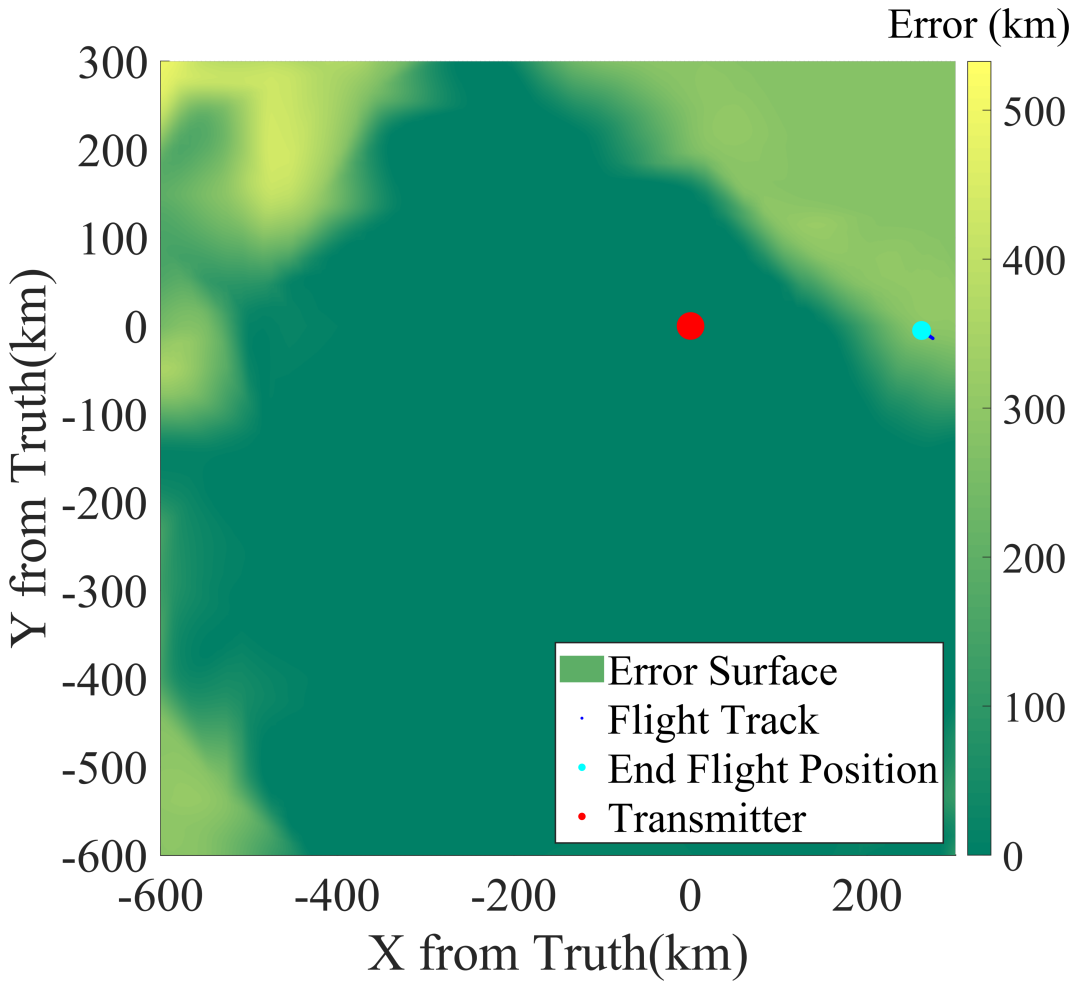

Figure 5.6: Depiction of the effect of different initial emitter position guesses for Flight Path 2.

apparent in each scenario. For the ephemeris error sets 1, 2, and 3, the cUKF's final estimates are approximiately 63, 71, and 75 kilometers away from the true emitter position, respectively. With the cUPF, those estimates are only 12, 8, and 18 kilometers away.

Fig. 5.10 showcases the geolocation performance when the transmitter is given the noise characteristics of Error Set 1 in Table 2.2 and the receiver is given noise characteristics of Error Set 2 in Table 2.2. Again the cUPF significantly outperforms the cUKF. It should be noted that the ephemeris errors appear to

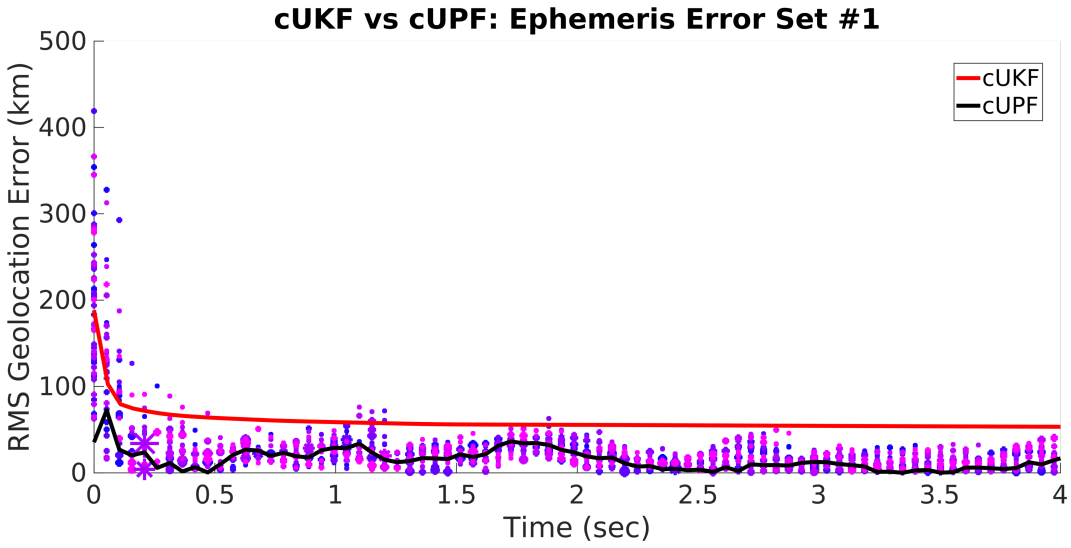

Figure 5.7: Ephemeris Error Set 1 (from Table 2.1).

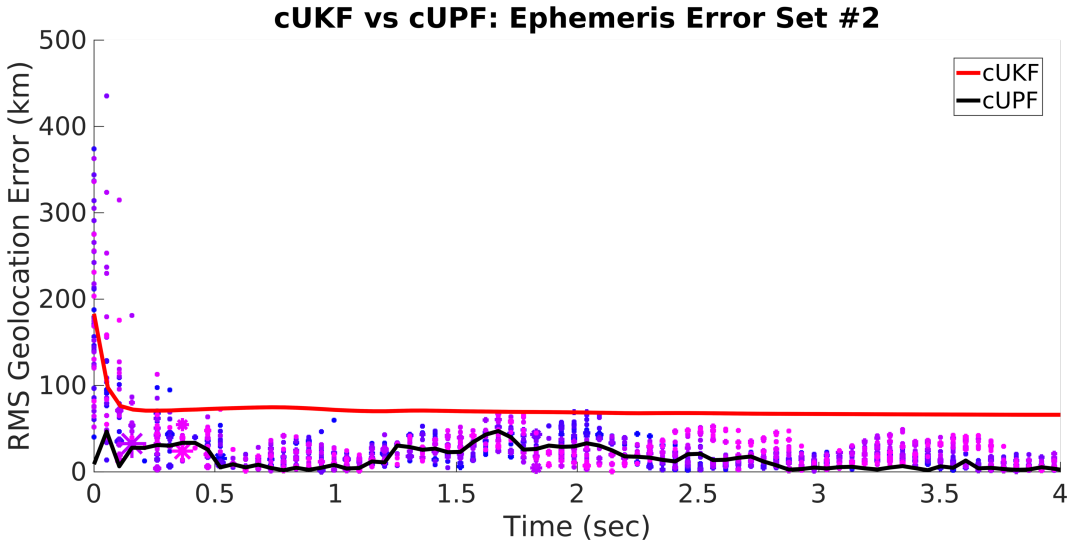

Figure 5.8: Ephemeris Error Set 2 (from Table 2.1).

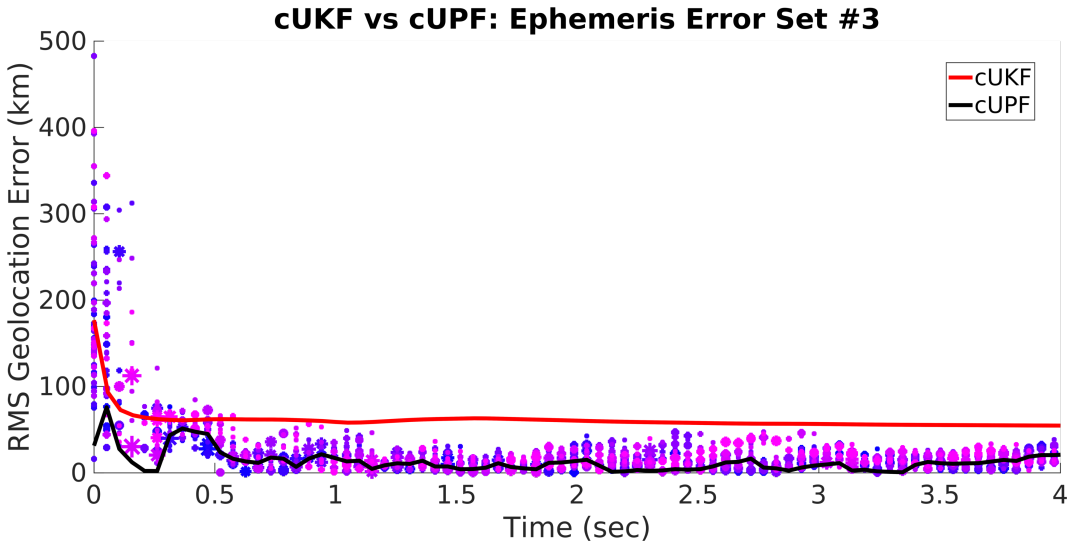

Figure 5.9: Ephemeris Error Set 3 (from Table 2.1).

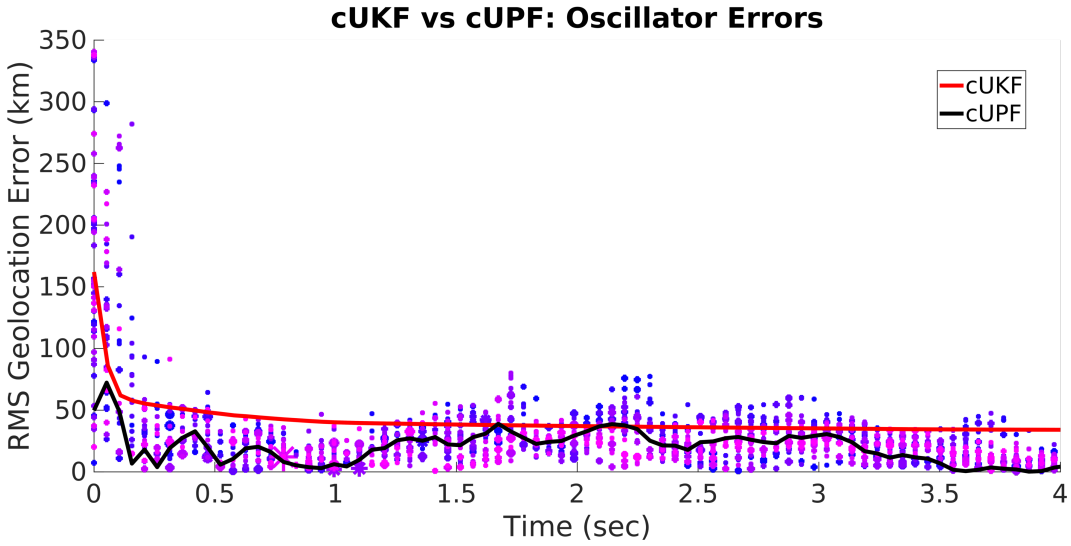

Figure 5.10: Oscillator Error Set (from Table 2.2).

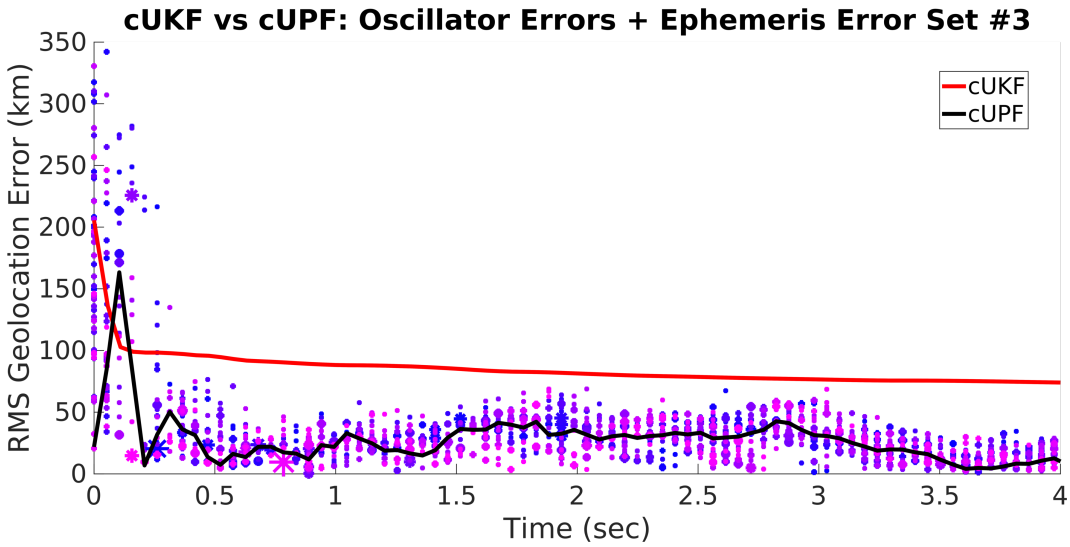

Figure 5.11: Oscillator Error Set and Ephemeris Error Set 3 (from Tables 2.1 and 2.2).

have a greater impact on geolocation error than oscillator errors. Indeed, the cUPF approaches only 3 kilometers of error when only oscillator errors are present.

When both oscillator and ephemeris errors (Error Set 3, the worst case scenario) are present, Fig. 5.11 shows that the cUKF fails to get within 96 kilometers of the true emitter position. The cUPF manages to converge to 10 kilometers of RMS geolocation error in only 4 seconds of acquisition time. Note, the particle degeneracy is avoided and "rogue" particles are corralled in efficiently for fast and accurate convergence. The particle initialization is such that the search area is nearly 400^2 km.

5.6 Computational Cost

Given that the cUPF utilized 20 particles and skipped every 10 samples, the computational cost for the cUPF and cUKF from the prior section (serving as the proposal distribution in the cUPF implementation) can now be expressed. This is outlined in Table 5.4 which utilizes Tables 3.2 and 3.3. It should be noted that

Table 5.4: Computational Cost of cUKF and cUPF Comparison Each kth Algorithmic Iteration

Category	**Flops**	$\sqrt{\cdot}$	**Trig**
cUKF	2028	114	140
cUPF	46998	2340	2820
Ratio	$\approx$ 21.3x	$\approx$ 20.5x	$\approx$ 20.1x

the proportional increase in computation per kth time step is roughly equal to the number of particles chosen (N_p), which in this case is 20. Tables 3.2 and 3.3 show this computational comparison in detail. However, since the cUPF skips every 10 time steps (for the numerical results on simulated data), the increase in computation over the entire algorithm run-time is only approximately two times more than the cUKF.

Chapter 6

Numerical Results: Raw Data

The Cyclone Global Navigation Satellite System (CYGNSS) is a fully functional constellation of 8 microsatellites in LEO whose goal is to improve extreme weather predictions, particularly hurricanes. CYGNSS is a NASA-sponsored project led by the Southwest Research Institute, University of Michigan, Sierra Nevada Corporation, and Surrey Satellite Technology [15]. The objective of

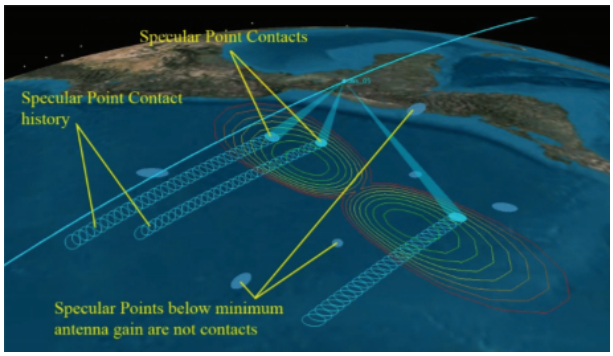

Figure 6.1: Functional depiction of the CYGNSS mission. A CYGNSS microsatellite travels above the Earth receiving reflections of GPS signals upon the water. Areas able to receive the GPS signal reflections are shown with the contoured, concentric circles representing where the antenna gain is large enough to secure the signal. These reflections undergo a Doppler shift caused by the surface water's motion that allows scientists to infer the wind speeds.

CYGNSS is illustrated in Fig. 6.1. One of the 8 microsatellites can be seen

flying above the Earth from left to right across the image. The microsatellite receives both direct and indirect signals from the GPS satellites. The direct signals go straight from the GPS satellite (not pictured) to the CYGNSS microsatellite and are used for precision positioning. The indirect signals also are emitted from the GPS satellite, but instead of traveling to the CYGNSS microsatellite directly, they reflect first upon the surface of the ocean and travel to the CYGNSS microsatellite listening above. The points where the indirect GPS signals reflect off of the water are called *specular points*. These specular points under go different Doppler shifts when reflecting off of different ocean surface contours. These Doppler shifts can be reliably mapped to calculations of wind speed.

This system has been performing successfully since its launch in December of 2016. Prior to its launch a proof-of-concept mission was flown in November of 2016 for final mission validation. The data from this proof-of-concept mission was obtained for the purposes of this Dissertation. Figures 6.3,6.4, and 6.6-6.8 used with permission from Scott Gleason.

6.1 Data Acquisition

On November 13, 2016 a proof-of-concept mission was scheduled to demonstrate the capabilities of the upcoming CYGNSS mission [15] in White Sands, New Mexico. The TDS-1 satellite (see Fig. 6.2) operated by Surrey Satellite Technology would be flying two passes within view of the proposed beacon location. To execute the mission objectives, the predicted ephemeris data of the TDS-1 satellite was obtained for the data collection time window. Similarly, the ephemeris data for the GPS satellites in view at that time was obtained as well as their specific psuedorandom noise sequence (PRN).

One of the main objectives of the proof-of-concept mission was to test how

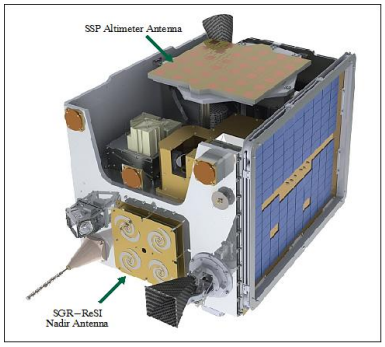

Figure 6.2: TDS-1 Satellite flown by Surrey Satellite Technology for the CYGNSS Proof-of-Concept mission in November 2016. TDS-1 has a size of 77 cm x 60 cm x 90 cm with an approximate launch mass of 156 kg and falls under the category of Minisatellite.

wide of a swath the CYGNSS satellite could reliably receive the specular points (as shown in Fig. 6.1) and to test the resolution of wind speed that could be detected (synonomous with Doppler shift of specular point). To do this, each PRN signal was imbued with small time delays and Doppler shifts - representing different locations and characteristics of specular points. By analyzing which of these points were "seen" by TDS-1, a rough experimental bound on the viewing limits of the CYGNSS satellites could be obtained as well as the Doppler resolution. The exact format of these spectral copies are shown in Fig. 6.3, which span Doppler shifts of ± 5 kHz and time delays of 1000 chips (equivalent to $\pm 16 \mu$sec).

One more hurdle remained to validate the CYGNSS operation. Looking at the mission concept in Fig. 6.4, the "Desired Scenario" depicts exactly what is shown in Fig. 6.1: a GPS satellite transmits its signal which then bounces off a watery area upon the Earth to be received by the CYGNSS (TDS-1) satellite overhead. However, due to this demonstration occurring in the middle of New Mexico, the bounce (specular point) would not occur as there was no water to reflect off of. The mission would have to emulate the desired scenario with only the "Reality" setup in Fig. 6.4, consisting of only the TDS-1 Satellite and a transmitting L1

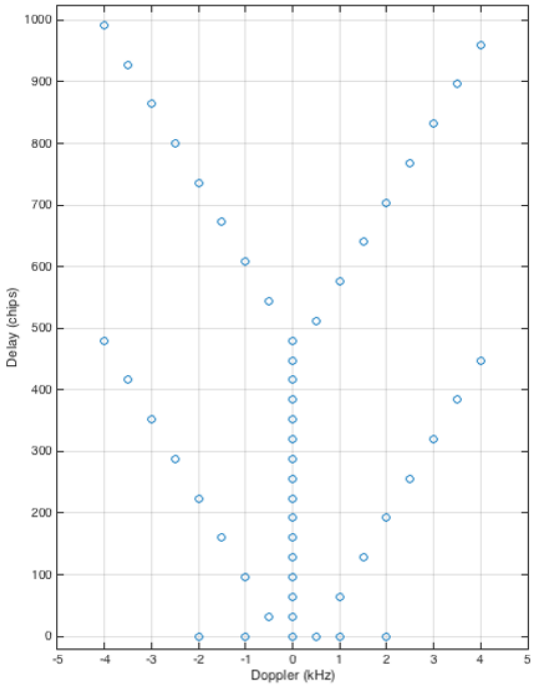

Figure 6.3: The baseband transmitted signal of 54 PRN summed sequences. Each dot represents a PRN sequence that has been imbued with a time delay and Doppler Shift.

beacon.

Figure 6.4: Mission concept of the TDS-1 Proof-of-Concept Demonstration.

In other words, although the GPS signal is being transmitted from the beacon to the TDS-1 satellite along the path r_{br}, doctoring of the signal needs to be done such that the signal appears to the TDS-1 satellite as though it had traveled across r_{st} and r_{sr}. This concept is pictured in Fig. 6.4. In order to accomplish this, the predicted ephemeris data of the TDS-1 satellite and the GPS satellites in view at

that time was obtained and used to pre-multiply each PRN signal (representing a specific GPS satellite) with the appropriate delay and Doppler shifts to make the signal appear to be coming from a moving specular point. This effectively emulates the "Desired Scenario" in Fig. 6.4 and the concept depicted in Fig. 6.1.

A visual summary of data manipulations in the experiment is shown in Fig. 6.5. It can be seen that the transmitted signal is comprised of two PRN sequences (7 and 9). Each PRN sequence is then multiplied with a specific delay and Doppler shifts to create 54 different specular points. These two sets of 54 GPS C/A coded replicas are then summed and multiplied with pre-calculated Doppler shifts to emulate the "Desired Scenario" of the specular points moving across the Earth as shown in Fig. 6.4. The signal is then transmitted at the L1 frequency and is received by the TDS-1 satellite, immediately downconverted to 4.188 MHz, and stored at 2 bit resolution.

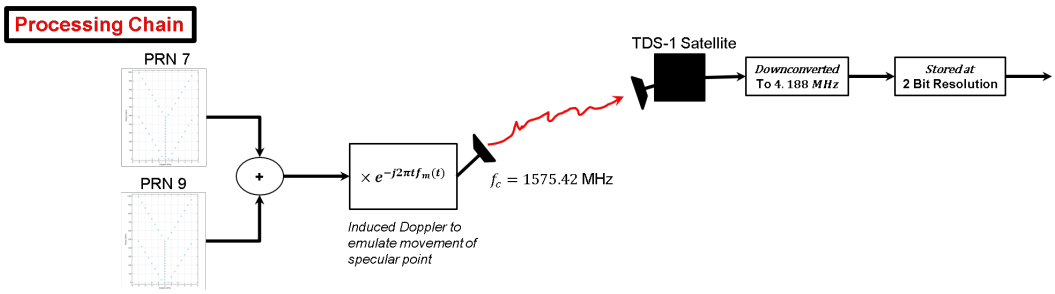

Figure 6.5: Functional diagram of the TDS-1 Experiment. The data stored at 2 bit resolution is the data used in this analysis.

An off-the-shelf USRP beacon with a pointing mechanism was set up to transmit a BPSK signal at 1200 baud to the TDS-1 satellite. The setup is shown below in Fig. 6.6.

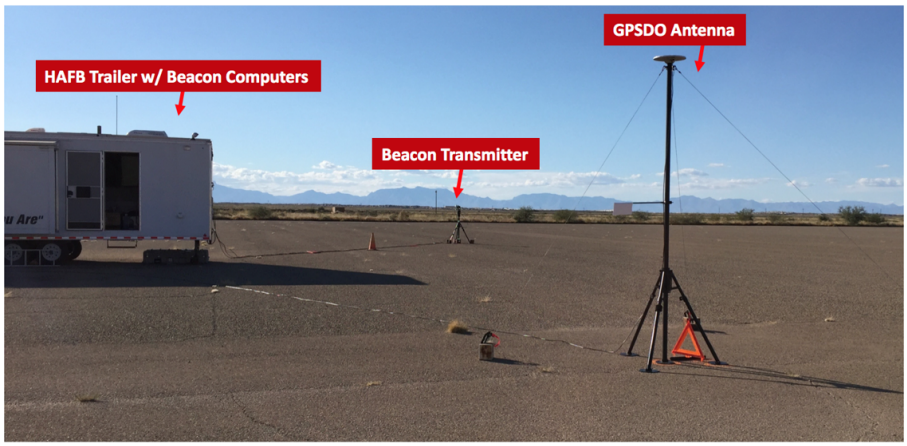

Figure 6.6: Experimental setup in White Sands, NM on November 13, 2016.

6.2 Data Processing

Two passes of the satellite were recorded but only one was usable due to timing and pointing mechanism errors. Roughly 74 seconds of this pass was made available and two GPS satellites were in view at the time corresponding to PRN sequence 7 and 9. The saved IQ data (stored at 2 Bit resolution) was converted into complex baseband form and then the pre-multiplied Doppler Shifts were removed as all geometry and necessary timekeeping of GPS satellites, TDS-1 satellite, and beacon were known. The scenario represented is now equivalent to the "Reality" scenario shown in Fig. 6.4 of a beacon transmitting to an overhead satellite.

As described in the previous section, each of the 54 GPS C/A coded replicas constituted a specular point. These specular points had a received power anywhere from -160 dBm to -125 dBm over the acquisition period. A Cross Ambiguity Function (CAF) was computed in an effort to reproduce Fig. 6.3. Due to the low received power (Fig. 6.7) and slight aiming errors (Fig. 6.8), these specular points flickered in and out of view sporadically throughout the pass. It should be noted that the peaks of the two plots in Fig. 6.7 are aligned in the subplot on the left but misaligned on the plot on the right. This is due to a combination of timing

errors possibly from the USRP radio and a clock bias on the TDS-1 satellite. The aiming errors as shown in Fig. 6.8 are most likely due to errors in the predicted ephemeris of the GPS and TDS-1 satellites.

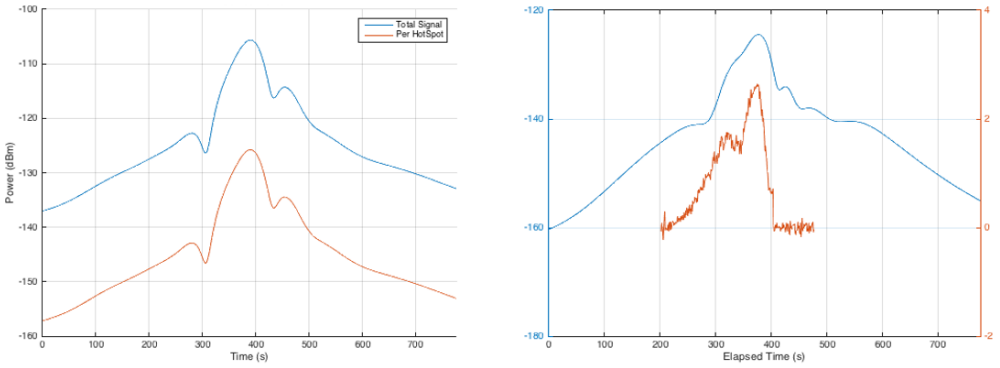

Figure 6.7: The plot on the left shows the Expected total received power in blue and the expected received power of each of the 54 specular points. The plot on the right shows once again the total expected received power (blue) versus magnitude of CAF (red) of one of the 54 spectral points.

The strongest, most consistently appearing specular spot (also referred to as a hotspot) was chosen to be extracted over the 74 seconds of acquisition time. Instantaneous frequency measurements were made by computing a Cross Ambiguity Function (CAF) every 0.125 seconds - thereby yielding the Doppler shift over time. The same numeric derivative and denoising algorithm as described in Section 5 was used to obtain the Doppler Rate. The position of the transceiver geometry over this acquisition period is shown in Fig. 6.9 along with the corresponding specular point over time, recreated in the developed simulation environment discussed in Section 2.3.5.

An example of the Doppler and Doppler Rate estimates are shown in Fig. 6.10. The Doppler is shown on the left subplot, and the Doppler Rate shown on the right subplot. Two estimates are provided on the Doppler Rate. The first uses a numerical derivative approach with smoothing. The second used a polynomial

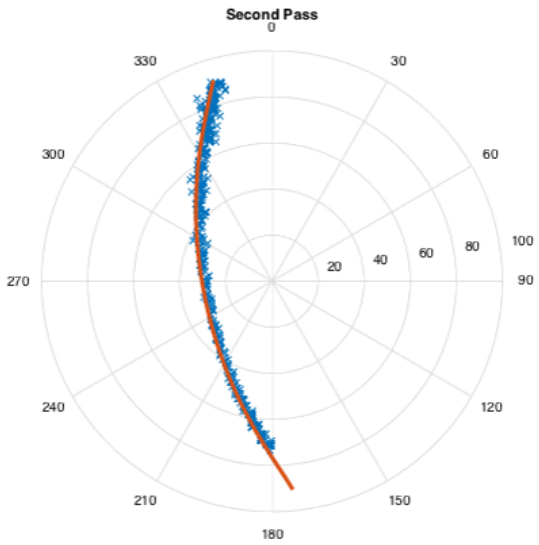

Figure 6.8: Recorded IMU pointing angle (blue) versus elevation angle (red) of recorded TDS-1 pass.

fitting technique to calculate the derivative and then added a pre-determined Gaussian noise to the answer as an attempt to avoid the bias created when using polynomial fitting. It was found that the former attempt yielded better cUKF and cUPF results than the latter.

6.3 cUKF

For the purposes of this section, the best (the time span yielding the most "accurate" Doppler and Doppler Rate estimates) 10 seconds of the 74 seconds available were used. The truth values over this acquisition time are shown in Fig. 6.11. The range at the first data point is 731.44 km at a slant angle of 25 deg. The Doppler estimates had an average bias of 100 Hz with a standard deviation of 485.98 Hz. The Doppler Rate estimates had an average bias of -30 Hz/Sec and a standard deviation of 41.08 Hz/Sec.

Initial guesses were drawn 150 times, distributed about the true emitter po-

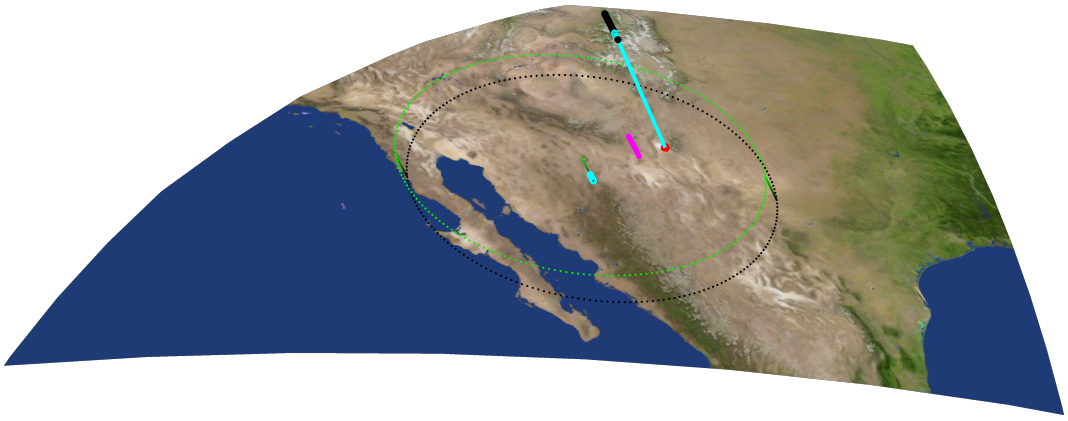

Figure 6.9: Geometry of the TDS-1 Proof-of-Concept Mission over the 10 second chosen acquisition period. The black line represents the movement of the TDS-1 Satellite, the line gradient from black to light green denotes the passage of time for the footprint and sub-satellite path. The pink line denotes the synthesized movement of the specular point (removed in pre-processing). The red dot represents the emitter. The cyan color denotes reception of the 10 seconds on the satellite path, sub-satellite path, and the corresponding range vectors.

sition with an initial average error of 225 km to emulate a realistic search space. Fig. 6.12 shows the performance of the cUKF algorithm utilizing the aforementioned 10 seconds of data. It can be seen that the algorithm converged under 10 km of the true emitter location, which is very encouraging considering the TDS-1 mission was not designed for geolocation. Limited samples, extremely low received power, and data stored at a 2-bit resolution do not provide an ideal scenario for

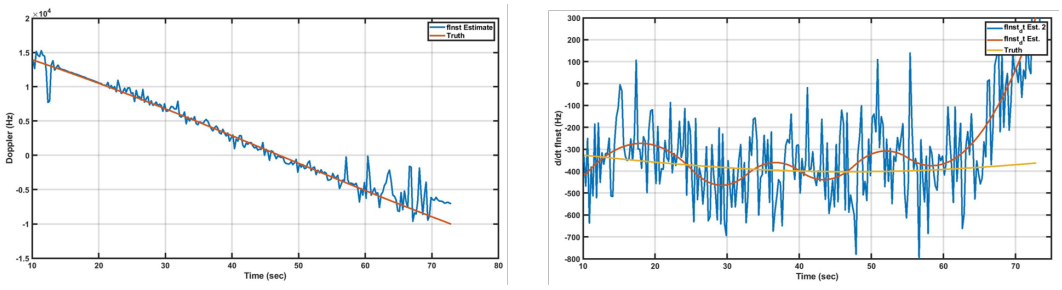

Figure 6.10: Truth values for Doppler and Doppler rate of the TDS-1 Proof-of-Concept Mission. Time is measured from the beginning of the 74 second acquisition period.

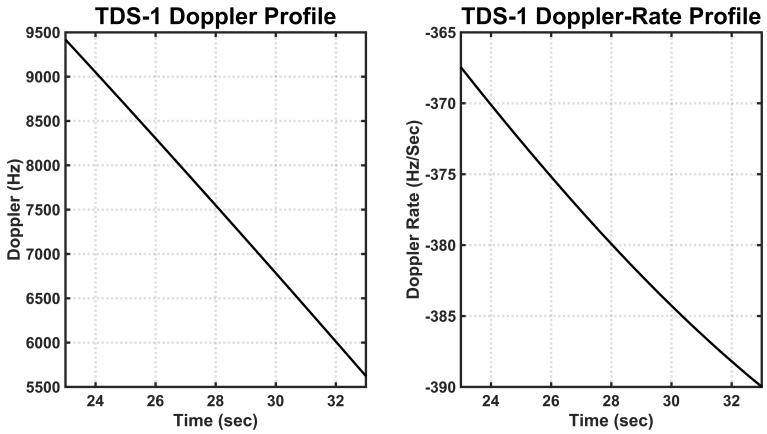

Figure 6.11: Truth values for Doppler and Doppler rate of the TDS-1 Proof-of-Concept Mission. Time is measured from the beginning of the 74 second acquisition period.

geolocating the beacon signal, but the algorithm's utility and effectiveness is clear. The absence of the rcPCRB is due to the error distributions exhibiting very large biases (over the 10 second time span) that invalidate the usage and comparative utility of the rcPCRB. However, it is very apparent that even under these settings, the cUKF filter performed very well.

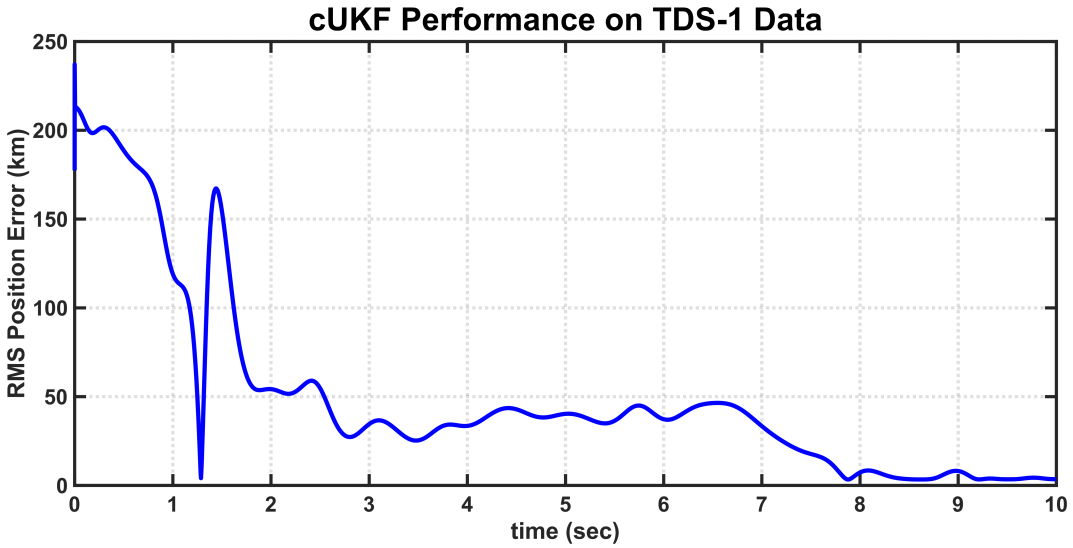

Figure 6.12: Performance of the cUKF on TDS-1 Data.

6.4 cUPF

In the prior section, the best 10 seconds of estimated measurements were chosen. For this scenario, 10 seconds of continuous data were chosen at random from the 74 seconds available, 50 times. Each 10 seconds of signal acquisition was estimated from 15 extracted seconds (so an additional 2.5 seconds obtained from the start and finish of the utilized 10 seconds) using the same methodology as the previous section. Again, Instantaneous frequency measurements were made by computing a Cross Ambiguity Function (CAF) every 0.125 seconds - thereby yielding the Doppler shift. A numeric derivative and least mean squares fit was used to obtain the Doppler Rate. The received power ranged anywhere from -160 dBm to -125 dBm over the acquisition period. The Doppler estimates had biases of up to 300 Hz with a standard deviation of up to 520.12 Hz. The Doppler Rate estimates had biases up to 50 Hz/Sec and a standard deviation up to 45.65 Hz/Sec. The range of truth values for Doppler and Doppler rate are shown in Fig. 6.10.

Fig. 6.13 shows the performance of both the cUKF and cUPF on the TDS-1 Data. The cUKF performance is seen to stabilize quickly at about 48 km geolocation error. Varying the state covariances or the measurement uncertainty produced negligible effects. This reflects the cUKF's inability to capture the phenomena and mitigate the noise present in the measurements. The cUPF however has managed to converge under 10 km of geolocation error.

The cUPF is seen to deal very well with the large biases exhibited in the measurements. This shows the capability of the weights to harness information from both the state assumptions and current estimates that are corrupted with highly erroneous measurements. With only a few samples (80 samples in total), convergence is reached within 3 seconds (24 samples). This was accomplished

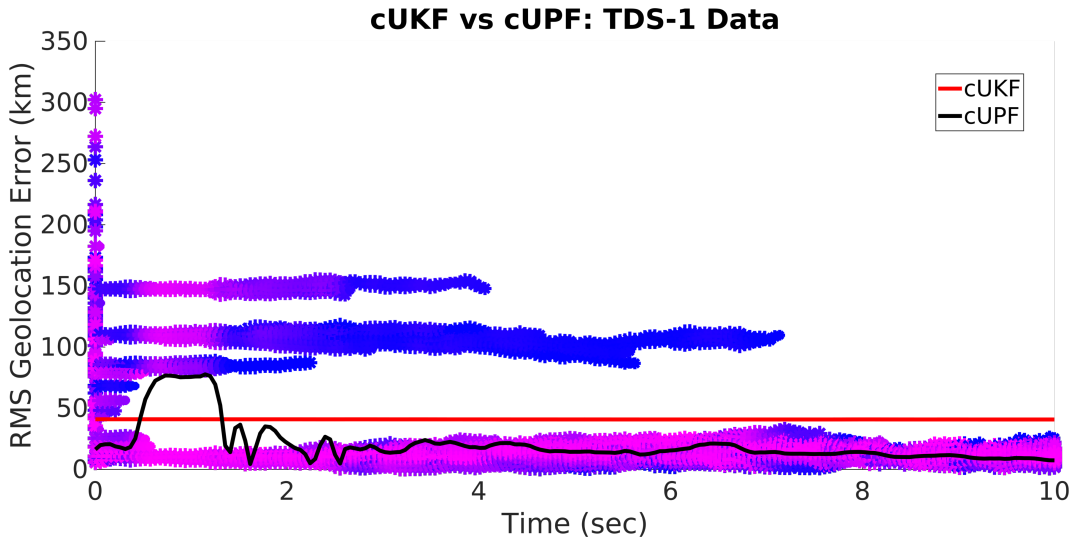

Figure 6.13: Performance of cUKF and cUPF on TDS-1 Data

with only $N_p = 20$ particles.

There is a well-posed trade space between the number of particles used, the number of samples (if possible) able to be skipped, and the desired accuracy of the geolocation estimates and rate of convergence. For this scenario, $N_p = 3$ particles produced a cUPF that consistently beat cUKF estimates. Any cUPF with $N_p > 20$ particles produced only marginal better RMS geolocation error.

The horizontal "lines" in Fig. 6.13 represent groups of particles that have converged on a particular geolocation estimate over time. Within the first second of filtering, there are many, which is reasonable considering how noisy and biased the Doppler and Doppler Rate measurements are. Then, in the 2-4 second filtering time interval there are only 6 horizontal lines. The 4-7 second interval has only three, and past the 8 second mark there remains only one, representing algorithmic convergence. This shows the cUPF's resiliency to the large biases present in the measurements, despite a very limited amount of time samples. Even in the first couple seconds, where many candidate geolocation estimates are being represented by particles with significant weight, the weighted average still hovers and hones

in to the correct geolocation position.

The results here are extremely encouraging. Resiliency to initialization error and low carrier-to-noise ratio were exhibited while obtaining nearly single-kilometer geolocation accuracies. This was all done despite very noisy and biased measurements taken at a sample rate of $\frac{1}{8}$th of a second from IQ samples saved at 2-bit resolution that was transmitted from an off-the-shelf USRP possessing a low quality oscillator (producing oscillator drift) to a SmallSat with additional timing errors and ephemeris errors. Within reason, it can safely be considered a worst-case scenario, and the performance of the cUPF is still very good.

For a standard space system that the cUPF could be applied to, 2-bit resolution is actually quite standard and it is very possible the emitter that is desired to be located possesses a similarly poor oscillator such as the USRP. However, sample rate can be expected to be much higher and further refinements on Doppler and Doppler rate measurements can easily applied. Further, if the system were to be made specifically for geolocation, oscillator error on the side of the receiver could be mitigated with a high quality crystal oscillator and the storage of the IQ data could easily be improved causing drastically increased geolocation accuracy.

In conclusion, the TDS-1 satellite dataset is a perfectly posed worse-case validation of the algorithms provided in this dissertation. The experiment was not meant for geolocation, but instead it was to provide a rough validation of the CYGNSS concepts working on a similar system. As a result, there are ephemeris errors, timing errors, and parasitic errors introduced from the many manipulations required to make the TDS-1 experiment emulate the desired scenario. Quantization and low sampling frequencies also play a major role in geolocation accuracy issues. Despite this, the cUPF algorithm performed exceptionally well and provides a high level of assurance for its capabilities on many existing and future

systems.

Chapter 7

Conclusion

7.1 Dissertation Summary

A passive radio frequency (RF) geolocation solution is provided that uses a single low earth orbit (LEO) satellite to find an uncooperative earth-bound emitter. Prior knowledge on the emitter's location only lends a several hundred kilometer search space. For the first time, an unambiguous solution is available for real-time, single-pass, and time-constrained acquisition scenarios where single transmissions are expected and computational abilities are limited. The geolocation algorithm rapidly maps Doppler and Doppler Rate measurements to an RF emitter location, performing a unique and powerful take on single satellite geolocation (SSG) - the provision of a geolocation estimate only using one satellite as a passive receiver.

Context of the provided technology is given in terms of past techniques and the constraints that are governed by the ill-conditioned solution space offered by the SSG scenario. It is rationalized that of the two approaches available to solve the SSG problem - Angle-of-Arrival and Doppler - that Doppler-based techniques holds the greatest potential. As was shown, the emitter position governs Doppler and Doppler Rate, providing highly informative measurements that al-

low for quick convergence and high geolocation accuracies. The additional measurement of Doppler Rate provides a drastically improved solution space free of ambiguities. An Earth-bound constraint - implemented in a fast and efficient projection technique - was also added that further improves the solution space. Given the high nonlinearity of the system affiliated with the proposed measurement and state constraint problems, as well as the computational limitations of onboard processing - an iterative, nonlinear filtering algorithm was found to be the optimal choice for the geolocation algorithm.

From the host of nonlinear filtering options, two variants were derived. These two solutions cater to approximately symmetric and asymmetric Posterior error distributions, respectively. The first is a variant of the constrained Unscented Kalman Filter (cUKF) which harnesses the estimation abilities of the Kalman Filter and the modeling capabilities of the Unscented Transform. When the error distributions are strongly non-symmetric, as is common when ephemeris and oscillator errors are present, a constrained Unscented Particle Filter (cUPF) has been derived to be used instead. In this solution, the cUKF is utilized as the proposal distribution to allow the Monte Carlo properties of the Particle Filter to efficiently characterize the Posterior Distribution, while avoiding sample degeneracy. Both the cUKF and cUPF solutions are capable of obtaining single-kilometer geolocation accuracy despite small sample sizes, short signal durations, large search areas, and non-trivial transceiver geometry. Computational costs of each algorithm are given in terms of three categories of floating point operations for a single iterative step.

Corresponding theoretic performance bounds are provided for mission analysis and algorithmic optimality comparison. The bound takes the form of the recursive constrained Posterior Cramér-Rao Bound (rcPCRB). This theoretic information

bound is uniquely suited to gauge the mean squared error optimality of iterative nonlinear estimation algorithms - and is recast and adapted to the SSG scenario.

In all simulated scenarios, the cUKF geolocation solution matches the optimal performance bounds provided by the rcPCRB, always reaching sub-kilometer geolocation accuracy with only a few seconds of signal acquisition time. Numerical analysis over measurement noise, center frequency, slant angle, and initialization errors showcase the cUKF's robustness and aptitude over different mission profiles. When oscillator and ephemeris errors are present, the cUPF continues to obtain single kilometer geolocation accuracies, even with single second acquisition times, limited computational powers, and search spaces spanning several hundred kilometers. Finally, the performance of the cUKF and cUPF are demonstrated on raw IQ data acquired from the TDS-1 satellite operated by Surrey Satellites, which listened to a transmitting beacon over White Sands, New Mexico. This real life experiment exactly represents the scenario designed for by this dissertation and provides a worst case test scenario with extremely low SNR, small sample size, ephemeris and oscillator errors, low sample rate, and high quantization error. Predictably, the cUKF failed to provide reliably useful estimates, yielding RMS geolocation accuracies of around 50 km. The cUPF performed extremely well, converging within three seconds with only 24 samples to within roughly 10 kilometers of the true emitter position over a 500^2 km search space.

7.2 Future Work

The work in this dissertation is rich in that many research efforts can spring from it. A theoretic information bound that would also accommodate distributions generated by ephemeris and oscillator errors is a highly desirable result. It would be an extension of the rcPCRB developed in this dissertation.

The problem of simultaneously estimating the center frequency of the transmitted signal is also a logical next step. The application of geolocating a wideband signal would be a major contribution.

Additionally, the use of single satellites to perform Satellite Cluster Geolocation where there is non-simultaneous reception, on the sharing of metadata (not IQ Data) would be an interesting and highly applicable trajectory.

Chapter 8

Appendix

8.1 Derivation of Received Signal

The following derivation of parameters within the received signal model is done for only two dimensions (x and y coordinates). The extension to three dimensions is straightforward. The dependence on time is suppressed and the derivation is kept general for both a moving emitter and satellite.

Range

$$r = |\mathbf{r}| \tag{8.1}$$

$$= |\mathbf{p}_s - \mathbf{p}_e| \tag{8.2}$$

Range Rate

$$
\begin{aligned}
v_r &= \frac{\partial}{\partial t}|\mathbf{r}| && (8.3)\\
&= \frac{\partial}{\partial t}((p_s^x - p_e^x)^2 - (p_s^y - p_e^y)^2)^{\frac{1}{2}} && (8.4)\\
&= \frac{\frac{\partial}{\partial t}((p_s^x - p_e^x)^2 - (p_s^y - p_e^y)^2)}{2((p_s^x - p_e^x)^2 - (p_s^y - p_e^y)^2)^{\frac{1}{2}}} && (8.5)\\
&= \frac{(p_s^x - p_e^x)(v_s^x - v_e^x) + (p_s^y - p_e^y)(v_s^y - v_e^y)}{|\mathbf{r}|} && (8.6)\\
&= \frac{[\mathbf{v}_s - \mathbf{v}_e]^T\mathbf{r}}{|\mathbf{r}|} && (8.7)
\end{aligned}
$$

Range Acceleration

$$
\begin{aligned}
a_r &= \frac{\partial^2}{\partial t^2}|\mathbf{r}| && (8.8)\\
&= \frac{\partial}{\partial t}\left(\underbrace{\frac{(p_s^x - p_e^x)(v_s^x - v_e^x)}{|\mathbf{r}|}}_{A_1} + \underbrace{\frac{(p_s^y - p_e^y)(v_s^y - v_e^y)}{|\mathbf{r}|}}_{A_2}\right) && (8.9)\\
&= \frac{\partial}{\partial t}A_1 + \frac{\partial}{\partial t}A_2 && (8.10)
\end{aligned}
$$

$$
\begin{aligned}
\frac{\partial}{\partial t}A_1 &= \frac{\partial}{\partial t}\frac{(p_s^x - p_e^x)(v_s^x - v_e^x)}{|\mathbf{r}|} && (8.11)\\
&= \frac{1}{|\mathbf{r}|}\left((v_s^x - v_e^x)(v_s^x - v_e^x) + (p_s^x - p_e^x)(a_s^x - a_e^x)\right)\\
&\quad - \frac{1}{|\mathbf{r}|^2}(p_s^x - p_e^x)(v_s^x - v_e^x)\\
&\quad \cdot \left(\frac{(p_s^x - p_e^x)(v_s^x - v_e^x) + (p_s^y - p_e^y)(v_s^y - v_e^y)}{|\mathbf{r}|}\right) && (8.12)
\end{aligned}
$$

$$\frac{\partial}{\partial t}A_2 = \frac{\partial}{\partial t}\frac{(p_s^y - p_e^y)(v_s^y - v_e^y)}{|\mathbf{r}|} \tag{8.13}$$

$$\begin{aligned} &= \frac{1}{|\mathbf{r}|}\left((v_s^y - v_e^y)(v_s^y - v_e^y) + (p_s^y - p_e^y)(a_s^y - a_e^y)\right) \\ &\quad - \frac{1}{|\mathbf{r}|^2}(p_s^y - p_e^y)(v_s^y - v_e^y) \\ &\quad \cdot \left(\frac{(p_s^x - p_e^x)(v_s^x - v_e^x) + (p_s^y - p_e^y)(v_s^y - v_e^y)}{|\mathbf{r}|}\right) \end{aligned} \tag{8.14}$$

Therefore, substituting Eq. 8.12 and Eq. 8.14 into Eq. 8.10:

$$a_r = \frac{1}{|\mathbf{r}|}\left(|\mathbf{v}_s - \mathbf{v}_e|^2 + \left(\mathbf{a}_s - \mathbf{a}_e\right)^T\mathbf{r}\right) - \frac{v_r}{|\mathbf{r}|^2}\left((\mathbf{v}_s - \mathbf{v}_e)^T\mathbf{r}\right) \tag{8.15}$$

$$= \frac{\left(\mathbf{a}_s - \mathbf{a}_e\right)^T\mathbf{r}}{|\mathbf{r}|} + \frac{|\mathbf{v}_s - \mathbf{v}_e|^2}{|\mathbf{r}|} - \frac{v_r^2}{|\mathbf{r}|} \tag{8.16}$$

8.2 Intersection of a Line and Ellipsoid

Let the line segment be defined by $\mathbf{p}_0 = \begin{bmatrix} x_0 & y_0 & z_0 \end{bmatrix}^T$ and $\mathbf{p}_1 = \begin{bmatrix} x_1 & y_1 & z_1 \end{bmatrix}^T$. This line can be parameterized in terms of arc length, s, by the following:

$$\begin{aligned} x &= (1-s)x_0 + sx_1 \\ y &= (1-s)y_0 + sy_1 \\ z &= (1-s)z_0 + sz_1 \end{aligned} \tag{8.17}$$

The equation of an ellipsoid with two equal axes is:

$$1 = \left(\frac{x}{a}\right)^2 + \left(\frac{y}{a}\right)^2 + \left(\frac{z}{b}\right)^2 \tag{8.18}$$

Substituting in (x, y, z) from Eq. 8.17 into Eq. 8.18:

$$\begin{aligned} 1 = & \frac{s^2(x_0^2 - 2x_0x_1 + x_1^2) + s(2x_ox_1 - 2x_0^2) + x_0^2}{a} \\ + & \frac{s^2(y_0^2 - 2y_0y_1 + y_1^2) + s(2y_oy_1 - 2y_0^2) + y_0^2}{a} \\ + & \frac{s^2(z_0^2 - 2z_0z_1 + z_1^2) + s(2z_oz_1 - 2z_0^2) + z_0^2}{b} \end{aligned} \tag{8.19}$$

And further simplifying:

$$\begin{aligned} 1 = & s^2\Bigg(\underbrace{\frac{(x_0 - x_1)^2 + (y_0 - y_1)^2}{a^2} + \frac{(z_0 - z_1)^2}{b^2}}_{\tilde{a}}\Bigg) \\ & + s\Bigg(\underbrace{\frac{2x_0x_1 - 2x_0^2 + 2y_0y_1 - 2y_0^2}{a^2} + \frac{2z_0z_1 - 2z_0^2}{b^2}}_{\tilde{b}}\Bigg) \\ & + \Bigg(\underbrace{\frac{x_0^2 + y_0^2}{a^2} + \frac{z_0^2}{b^2}}_{\tilde{c}}\Bigg) \end{aligned} \tag{8.20}$$

This is a quadratic that can be solved using the positive solution:

$$s = \frac{-\tilde{b} + \sqrt{\tilde{b}^2 - 4\tilde{a}\tilde{c}}}{2\tilde{a}} \tag{8.21}$$

which can be substituted into Eq. 8.17 to obtain the point of intersection.

8.3 Derivatives for rcPCRB

This Appendix shows the calculations of the derivatives in Eq. 4.26, the traditional Fisher Information Matrix (FIM). The FIM can be written as:

$$\begin{aligned}\mathbf{J}_k &= \mathbb{E}\left\{\left(\frac{\partial}{\partial \mathbf{x}_k}\ln p(\mathbf{z}_k|\mathbf{x}_k)\right)^T\left(\frac{\partial}{\partial \mathbf{x}_k}\ln p(\mathbf{z}_k|\mathbf{x}_k)\right)\right\} \\ &= \left(\frac{\partial}{\partial \mathbf{x}_k}\mathbf{h}_k\right)^T\mathbf{V}_k^{-1}\left(\frac{\partial}{\partial \mathbf{x}_k}\mathbf{h}_k\right) \end{aligned} \tag{8.22}$$

where $\mathbf{V}_k$ is a zero mean covariance matrix of the measurement noise vector $\mathbf{v}_k$, which is an independent white noise process. Noting that $\mathbf{x}_k = \mathbf{p}_{e(k)}$, the measurement equation can be described as:

$$\mathbf{z}_k = \mathbf{h}_k + \mathbf{v}_k \tag{8.23}$$

$$= \begin{bmatrix} h_k^{(1)}(\mathbf{x}_k) \\ h_k^{(2)}(\mathbf{x}_k)\end{bmatrix} + \begin{bmatrix} v_k^{(1)} \\ v_k^{(2)}\end{bmatrix} \tag{8.24}$$

where

$$h_k^{(1)}(\mathbf{x}_k) = -\left(\frac{1}{\lambda}\right)\left(\frac{\mathbf{v}_{s(k)}^T[\mathbf{p}_{s(k)} - \mathbf{x}_k]}{|\mathbf{p}_{s(k)} - \mathbf{x}_k|}\right) \tag{8.25}$$

and

$$h_k^{(2)}(\mathbf{x}_k) = -\left(\frac{1}{\lambda}\right)\left(\frac{\mathbf{a}_{s(k)}^T(\mathbf{p}_{s(k)}(t_k) - \mathbf{x}_k)}{|\mathbf{p}_{s(k)} - \mathbf{x}_k|} + \frac{|\mathbf{v}_{s(k)}|^2}{|\mathbf{p}_{s(k)} - \mathbf{x}_k|} - \frac{\left(\frac{\mathbf{v}_{s(k)}^T(\mathbf{p}_{s(k)} - \mathbf{x}_k)}{|\mathbf{p}_{s(k)} - \mathbf{x}_k|}\right)^2}{|\mathbf{p}_{s(k)} - \mathbf{x}_k|}\right) \tag{8.26}$$

Then, Eq. 8.22 can be fully expressed by computing the partial derivatives of the measurement equation 8.24:

$$\frac{\partial}{\partial x_k^{(i)}}\mathbf{z}_k(\mathbf{x}_k) = \begin{bmatrix} \frac{\partial}{\partial x_k^{(i)}} z_k^{(1)}(\mathbf{x}_k) \\ \frac{\partial}{\partial x_k^{(i)}} z_k^{(2)}(\mathbf{x}_k) \end{bmatrix} \tag{8.27}$$

$$= \begin{bmatrix} \frac{\partial}{\partial x_k^{(i)}} h_k^{(1)}(\mathbf{x}_k) \\ \frac{\partial}{\partial x_k^{(i)}} h_k^{(2)}(\mathbf{x}_k) \end{bmatrix} \tag{8.28}$$

Then the derivatives can be computed using the quotient and product rule. Namely, given the generic equation $\mathbf{c}(\mathbf{x}) = \frac{\mathbf{a}(\mathbf{x})}{\mathbf{b}(\mathbf{x})}$:

$$\mathbf{c}'(\mathbf{x}) = \frac{\mathbf{a}'(\mathbf{x})\mathbf{b}(\mathbf{x}) - \mathbf{a}(\mathbf{x})\mathbf{b}'(\mathbf{x})}{\mathbf{b}^2(\mathbf{x})} \tag{8.29}$$

Then for $\frac{\partial}{\partial x_k^{(i)}} h_k^{(1)}(\mathbf{x}_k)$:

$$a(\mathbf{x}_k) = \mathbf{v}_{s(k)}^T(\mathbf{p}_{s(k)} - \mathbf{x}_k) \tag{8.30}$$

$$\frac{\partial}{\partial x_k^{(i)}} a(\mathbf{x}_k) = -v_{s(k)}^{(i)} \tag{8.31}$$

$$b(\mathbf{x}_k) = |\mathbf{p}_{s(k)} - \mathbf{x}_k| \tag{8.32}$$

$$\frac{\partial}{\partial x_k^{(i)}} b(\mathbf{x}_k) = \frac{p_{e(k)}^{(i)} - p_{s(k)}^{(i)}}{|\mathbf{p}_{s(k)} - \mathbf{x}_k|} \tag{8.33}$$

yielding the final result of:

$$\frac{\partial}{\partial x_k^{(i)}} z_k^{(1)}(\mathbf{x}_k) = \left(\frac{1}{\lambda}\right)\left(\frac{-v_{s(k)}^{(i)}|\mathbf{p}_{s(k)} - \mathbf{x}_k| - (\mathbf{v}_{s(k)}^T(\mathbf{p}_{s(k)} - \mathbf{x}_k))\frac{p_{e(k)}^{(i)} - p_{s(k)}^{(i)}}{|\mathbf{p}_{s(k)} - \mathbf{x}_k|}}{|\mathbf{p}_{s(k)} - \mathbf{x}_k|^2}\right) \tag{8.34}$$

A similar fashion is used for $\frac{\partial}{\partial x_k^{(i)}} z_k^{(2)}(\mathbf{x}_k)$, the derivative is more complex so is divided into three parts such that:

$$\frac{\partial}{\partial x_k^{(i)}} z_k^{(2)}(\mathbf{x}_k) = \frac{\partial}{\partial x_k^{(i)}} A(\mathbf{x}_k) + \frac{\partial}{\partial x_k^{(i)}} B(\mathbf{x}_k) + \frac{\partial}{\partial x_k^{(i)}} C(\mathbf{x}_k) \tag{8.35}$$

where

$$A(\mathbf{x}_k) = \left(\frac{-1}{\lambda}\right)\left(\frac{\mathbf{a}_{s(k)}^T(\mathbf{p}_{s(k)}(t_k) - \mathbf{x}_k)}{|\mathbf{p}_{s(k)} - \mathbf{x}_k|}\right) \tag{8.36}$$

$$\frac{\partial}{\partial x_k^{(i)}} A(\mathbf{x}_k) = \left(\frac{-1}{\lambda}\right)\left(\frac{-a_{s(k)}^{(i)}|\mathbf{p}_{s(k)} - \mathbf{x}_k| - (\mathbf{a}_{s(k)}^T(\mathbf{p}_{s(k)} - \mathbf{x}_k))\frac{p_{e(k)}^{(i)} - p_{s(k)}^{(i)}}{|\mathbf{p}_{s(k)} - \mathbf{x}_k|}}{|\mathbf{p}_{s(k)} - \mathbf{x}_k|^2}\right) \tag{8.37}$$

$$B(\mathbf{x}_k) = \left(\frac{-1}{\lambda}\right)\left(\frac{|\mathbf{v}_{s(k)}|^2}{|\mathbf{p}_{s(k)} - \mathbf{x}_k|}\right) \tag{8.38}$$

$$\frac{\partial}{\partial x_k^{(i)}} B(\mathbf{x}_k) = \left(\frac{-1}{\lambda}\right)\left(\mathbf{v}_k^T\mathbf{v}_k\right)\frac{\partial}{\partial x_k^{(i)}}\left((\mathbf{p}_{s(k)} - \mathbf{x}_k)^T(\mathbf{p}_{s(k)} - \mathbf{x}_k)\right)^{-\frac{1}{2}} \tag{8.39}$$

$$= \left(\frac{1}{\lambda}\right)\left(\frac{|\mathbf{v}_k|^2(p_{e(k)}^{(i)} - p_{s(k)}^{(i)})}{|\mathbf{p}_{s(k)} - \mathbf{x}_k|^3}\right) \tag{8.40}$$

$$C(\mathbf{x}_k) = \left(\frac{-1}{\lambda}\right)\left(-\frac{\left(\frac{\mathbf{v}_{s(k)}^T(\mathbf{p}_{s(k)} - \mathbf{x}_k)}{|\mathbf{p}_{s(k)} - \mathbf{x}_k|}\right)^2}{|\mathbf{p}_{s(k)} - \mathbf{x}_k|}\right) \tag{8.41}$$

$$\begin{aligned}\frac{\partial}{\partial x_k^{(i)}} C(\mathbf{x}_k) = &\left(\frac{-1}{\lambda}\right)\left(\frac{1}{((\mathbf{p}_{s(k)} - \mathbf{x}_k)^T(\mathbf{p}_{s(k)} - \mathbf{x}_k))^3}\right) \times \dots \\ &+ \Bigg(- 2\mathbf{v}_{s(k)}(\mathbf{v}_{s(k)}^T(\mathbf{p}_{s(k)} - \mathbf{x}_k) \cdot \left((\mathbf{p}_{s(k)} - \mathbf{x}_k)^T(\mathbf{p}_{s(k)} - \mathbf{x}_k)\right)^{\frac{3}{2}} + \dots \\ &\quad 3(p_{s(k)}^{(i)} - x_k^{(i)})|\mathbf{p}_{s(k)} - \mathbf{x}_k|(\mathbf{v}_{s(k)}^T(\mathbf{p}_{s(k)} - \mathbf{x}_k))^2\Bigg)\end{aligned} \tag{8.42}$$

where use of the quotient rule (Eq. 8.29) was used in the following fashion:

$$a(\mathbf{x}_k) = \Big(\mathbf{v}_{s(k)}^T(\mathbf{p}_{s(k)} - \mathbf{x}_k)\Big)^2 \tag{8.43}$$

$$\frac{\partial}{\partial x_k^{(i)}} a(\mathbf{x}_k) = -2v_{s(k)}(i)\Big(\mathbf{v}_{s(k)}^T(\mathbf{p}_{s(k)} - \mathbf{x}_k)\Big) \tag{8.44}$$

$$b(\mathbf{x}_k) = \Big((\mathbf{p}_{s(k)} - \mathbf{x}_k)^T(\mathbf{p}_{s(k)} - \mathbf{x}_k)\Big)^{\frac{3}{2}} \tag{8.45}$$

$$\frac{\partial}{\partial x_k^{(i)}} b(\mathbf{x}_k) = -3|\mathbf{p}_{s(k)} - \mathbf{x}_k|(p_{s(k)}^{(i)} - x_k^{(i)}) \tag{8.46}$$

Bibliography

[1] Small satellites: A revolution in space science. , Keck Institute for Space Studies and California Institute of Technology, Pasadena, CA, 2014.

[2] The space report. , Space Foundation, 2016.

[3] Global trends in small satellites. , Science and Technology Policy Institute, Washington, DC, 2017.

[4] A. Arechiga, A. Michaels, and J. Black. Onboard Image Processing for Small Satellites. *NAECON 2018*, -(-):234–240, 2018.

[5] Service Argos. Argos User's Manual. 2009.

[6] J. Arlas and S. Spangelo. GPS Results for the Radio Aurora Explorer II CubeSat Mission. *51st AIAA Aerospace Sciences Meeting*, 2013.

[7] M. Arulampalam, S. Maskell, N. Gordon, and T. Clapp. A Tutorial on Particle Filters for Online Nonlinear/Non-Gaussian Bayesian Tracking. *IEEE Trans. on Signal Processing*, 50(2):174–188, 2002.

[8] K. Bell and H.V. Trees. Posterior Cramer-Rao Bound for Tracking Target Bearing. *Adaptive Sensor Array Process. Workshop*, pages 773–778, 2005.

[9] B. Boashash. Estimating and Interpreting the Instantaneous Frequency of a Signal. I. Fundamentals. In *Proceedings IEEE*, volume 4, pages 520–538, 1992.

[10] B. Boashash. Estimating and Interpreting the Instantaneous Frequency of a Signal. II. Algorithms and Applications. In *Proceedings IEEE*, volume 4, pages 540–568, 1992.

[11] D. CaJacob, N. McCarthy, T. OâĂŹShea, and R. McGwier. Geolocation of RF Emitters with a Formation-Flying Cluster of Three Microsatellites. In *30th Annual AIAA/USU Conference on Small Satellites*, pages 1–13, 2016.

[12] H. Cramer. *Mathematical Methods of Statistics*. Princeton Univ. Pres, Princeton, NJ, USA, 1945.

[13] J. Crestel, B. Emile, M. Guitton, and D. Menard. A Doppler Frequency Estimate Using the Instantaneous Frequency. In *Proceedings of 13th International Conference on Digital Signal Processing*, pages 777–780. IEEE, 1997.

[14] R. Danchik. Navy Navigation Satellite System. *Johns Hopkins APL Technical Digest*, 5(4):323–329, 1984.

[15] J. Dickinson, C. Ruf, R. Rose, A. Ridley, and B. Walls. CYGNSS: The Cyclone Global Navigation Satellite System's CubeSat Foundations. *12th Annual JACIE (Joint Agency Commercial Imagery Evaluation) Workshop*, 2013.

[16] J. V. DiFranco and W.L. Rubin. *Radar Detection*. Artech House, Inc., Dedham, MA, USA, 1980.

[17] A. Doucet, S. Godsill, and C. Andrieu. On sequential Monte Carlo sampling methods for Bayesian filtering. *Statistics and Computing*, 10(3):198–208, 2000.

[18] P. Ellis and F. Dowla. A Single Satellite Geolocation Solution of an RF Emitter using a Constrained Unscented Kalman Filter. *IEEE Statistical Signal Processing Workshop 2018*, pages 643–647, 2018.

[19] P. Ellis and F. Dowla. Performance Bounds of a Single LEO Satellite Providing Geolocation of an RF Emitter. *9th Advanced Satellite Multimedia Systems Conference and 15th Signal Processing for Space Communications Workshop*, pages 1–5, 2018.

[20] P. Ellis, D. V. Rheeden, and F. Dowla. Use of Doppler and Doppler Rate for RF Geolocation Using a Single LEO Satellite. *IEEE Access*, Early Access, January 2020.

[21] L. Galleani. A tutorial on the two-state model of the atomic clock noise. *Metrologia*, 45:S175–S182, 2008.

[22] M. Garcia-Fernandez and O. Montenbruck. Low Earth Orbit Satellite Navigation Errors and Vertical Total Electron Content in Single-Frequency GPS Tracking. *Radio Science*, 41(RS5001):48–57, 2006.

[23] W. Gardner. *An Introduction to Cyclostationary Signals*. IEEE PRESS Marketing, 445 Hoes Lane Piscataway, NJ 08855-1331, 1994.

[24] A. George and C. Wilson. Onboard Processing With Hybrid and Reconfigurable Computing on Small Satellites. *Proceedings of IEEE*, 106(3):458–471, 2018.

[25] J.D. Gorman and A. O. Hero. Lower Bounds for Parametric Estimation with Constraints. *IEEE Trans. Inform. Theory*, 26:1285–1301, 1990.

[26] W. H. Guier and G. C. Weiffenbach. A Satellite Doppler Navigation System. *Proceedings of the IRE*, 48(4):507–516, April 1960.

[27] F. Guo. Single-Satellite Geolocation System Based on Direction Finding. In *Space Electronic Reconnaissance: Localization Theories and Methods First Edition*, chapter 3. Wiley and Sons Singapore Pte Ltd., Singapore, 2014.

[28] F. Guo. Single-Satellite Geolocation System Based on the Kinematic Principle. In *Space Electronic Reconnaissance: Localization Theories and Methods First Edition*, chapter 6. Wiley and Sons Singapore Pte Ltd., Singapore, 2014.

[29] A. Hauschild, M. Markgraf, and O. Montenbruck. GPS Receiver Perfromance On Board a LEO Satellite. *InsideGNSS*, pages 48–57, 2014.

[30] C. He, M. Zhang, and F. Guo. Bias Compensation for AOA-Geolocation of Known Altitude Target Using Single Satellite. *IEEE Access*, 7:54295–54304, April 2019.

[31] K. C. Ho and Y. T. Chan. Geolocation of a Known Altitude Object From TDOA and FDOA Measurements. In *IEEE Trans. on Aerospace and Electronic Systems*, volume 33, pages 770–783, 1997.

[32] K. C. Ho and Y. T. Chan. Algebraic Two-Satellite TOA/FOA Position Solution on an Ellipsoidal Earth. In *IEEE Trans. on Aerospace and Electronic Systems*, volume 40, pages 1087–1092, 2004.

[33] R. Hunger. Floating point operations in matrix-vector calculus. , Technische Universitat Munchen, 2007.

[34] S. J. Julier and J. J. LaViola. On Kalman Filtering With Nonlinear Equality Constraints. *IEEE Transactions on Signal Processing*, 55(6):2774–2784, June 2007.

[35] S. J. Julier and J. K. Uhlmann. Unscented Filtering and Nonlinear Estimation. *Proceedings of the IEEE*, 92(3):401–422, Mar 2004.

[36] R. Kandepu, L. Imsland, and B. A. Foss. Constrained state estimation using the Unscented Kalman Filter. In *2008 16th Mediterranean Conference on Control and Automation*, pages 1453–1458, June 2008.

[37] G. Kitagawa. Monte Carlo filter and smoother for non-Gaussian non-linear state space models. *Journal of Computational and Graphical Statistics*, 5(1):1–25, 1996.

[38] J. Klimas. A small satellite revolution, 2019.

[39] I. Klotz. Small satellites driving space industry: Report, 2017.

[40] N. Levanon. Theoretical Bounds on Random Errors in Satellite Doppler Navigation. *IEEE Transactions on Aerospace and Electronic System*, 20:810–816, November 1984.

[41] N. Levanon. Theoretical Bounds on Random Errors in Satellite Doppler Navigation. *IEEE Transactions on Aerospace and Electronic Systems*, 20:810–816, November 1984.

[42] N. Levanon. Instant Active Positioning with One LEO Satellite. *Journal of The Institute of Navigation*, 46:87–95, June 1999.

[43] N. Levanon and M. Ben-Zaken. Random Error in ARGOS and SARSAT Satellite Positioning Systems. *IEEE Transactions on Aerospace and Electronic Systems*, 21:783–790, November 1985.

[44] N. Levanon and E. Weinstein. Angle-Independent Doppler Velocity Measurement. *IEEE Transactions on Aerospace and Electronic Systems*, AES-19(3):354–359, May 1983.

[45] D. Levesque. The History and Experience of the International COSPAS-SARSAT Programme. International Astronautical Federation (IAF), 2016.

[46] R. Lopez, J. P. MalardÃĺ, F. Royer, and P. Gaspar. Improving Argos Doppler Location Using Multiple-Model Kalman Filtering. *IEEE Transactions on Geoscience and Remote Sensing*, 52(8):4744–4755, Aug 2014.

[47] W. Luk, D. Thomas, P. Leong, and J. Villasenor. Gaussian Random Number Generators. *ACM Computing Surveys*, 39(4), 2007.

[48] J. Marini. Error Analysis for Relay Type Satellite-Aided Search and Rescue Systems. *IEEE Transactions on Aerospace and Electronic Systems*, 15:660–665, September 1979.

[49] T. L. Marzetta. A Simple Derivation of the Constrained Multiple Parameter Cramer-Rao Bound. *IEEE Trans. Signal Processing*, 41:2247–2249, 1993.

[50] D. J. Nelson and J. B. McMahon. Target location from the estimated instantaneous received frequency. Proceedings of SPIE 8020, Airborne Intelligence, Surveillance, Reconnaissance (ISR) Systems and Applications VIII, 2011.

[51] N. Nguyen and K. Dogancay. Algebraic Solution for Stationary Emitter Geolocation by a LEO Satellite Using Doppler Frequency Measurements. In *Proceedings ICASSP*, volume II, pages 3341–3345. IEEE, 2016.

[52] T. Pattison and S. I. Chou. Sensitivity Analysis of Dual-Satellite Geolocation. In *IEEE Trans. on Aerospace and Electronic Systems*, volume 36, pages 56–71, 2000.

[53] D. Petrick. SpaceCube v2.0 space flight hybrid reconfigurable data processing system. *Proc. IEEE Aerosp. Conf.*, -(-):234–240, 2014.

[54] C. Rao. Information and the accuracy attainable in the estimation of statistical parameters. *Bull. Calcutta Math. Soc.*, 37:81–91, 1945.

[55] R. Ren and M. Fowler. An LBI Based Emitter Location Estimator with Platform Trajectory Optimality. *2009 Conference Record of the 43rd Asilomar Conference on Signals, Systems and Computers*, pages 1692–1696, May 2009.

[56] B. Ristic, S. Arulampalam, and N. Gordon. Beyond the Kalman Filter: Particle Filters for Tracking Applications. *Journal of Computational and Graphical Statistics*, 2003.

[57] H. Saito. Miniature Space GPS Receiver by means of Automobile-Navigation Technology. *21st Aunnual AIAA/USU Conference on Small Satellites*, pages 773–778, 2007.

[58] W. C. Scales and R. Swanson. Air and Sea Rescue via Satellite Systems: Even Experimental Systems Have Helped Survivors of Air and Sea Accidents. Two Different Approaches are Discussed. *IEEE Spectrum*, 21(3):48–52, March 1984.

[59] L. Schmitt and W. Fichter. Cramer-Rao Lower Bound for State-Constrained Nonlienar Filtering. *IEEE Signal Processing Letters*, 24(12):1882–1885, 2017.

[60] D. Shaw and P. Roques. Random Error in ARGOS and SARSAT Satellite Positioning Systems. *IEEE Transactions on Aerospace and Electronic Systems*, 21:783–790, November 1985.

[61] D. Simon. Kalman filtering with state constraints: a survey of linear and nonlinear algorithms. *IET Control Theory Applications*, 4(8):1303–1318, August 2010.

[62] Y. Song and D. Gnyawali. What Drives Innovation Choices in The Small Satellite Industry? The Role of Technological Resources and Managerial Experience. In *31st Annual AIAA/USU Conference on Small Satellites*, pages 1–6. AIAA/USU, 2-17.

[63] S. Spangelo, A. Klesh, and J. Culter. Position and Time System for the RAX Small Satellite Mission. *AIAA/AAS Astrodynamics Specialist Conference*, 2010.

[64] T. Stansell. The TRANSIT Navigation Satellite System. *Magnavox Government and Industrial Electronics Company*, 1983.

[65] P. Stoica and B. Ng. On the Cramer-Rao Bound under Parameteric Constraints. *IEEE Signal Processing Letters*, 5(7):177–179, 1998.

[66] P. Tichavsky, C. Muravchik, and A. Nehorai. Posterior Cramer Rao Bounds for Discrete Time Nonlinear Filtering. *IEEE Trans. on Signal Processing*, 46:1386–1396, 1998.

[67] G. Whitesides. Launching the small-satellite revolution, 2015.

[68] E.C. Williams, C.P. Bridges, and M.D. J. Bowyer. Nowhere to Hide? Passive, Non-Cooperative Maritime Surveillance from a Nanosat. *2018 IEEE Aerospace Conference*, 2018.

[69] H. Witzgall. A reliable Doppler-based solution for single sensor geolocation. In *2013 IEEE Aerospace Conference*, pages 1–7, March 2013.

[70] C. Xi, W. Menglu, and Z. Lei. Analysis on the Performance Bound of Doppler Positioning Using One LEO Satellite. *Vehicular Technology Conference*, 1, May 2016.